METAMATERIAL APPLICATIONS FOR VIBRATION AND WAVE PROPAGATION IN 1D ELASTIC RODS

A Dissertation
Presented to
The Academic Faculty

By

William R. Johnson

In Partial Fulfillment
of the Requirements for the Degree
Doctor of Philosophy in the
School of Mechanical Engineering

Georgia Institute of Technology

December 2020

METAMATERIAL APPLICATIONS FOR VIBRATION AND WAVE PROPAGATION IN 1D ELASTIC RODS

Approved by:

Dr. Ruzzene, Advisor
Department of Mechanical Engineering
University of Colorado Boulder

Dr. Leamy, Co Advisor
School of Mechanical Engineering
Georgia Institute of Technology

Dr. Sabra
School of Mechanical Engineering
Georgia Institute of Technology

Dr. DiLeo
School of Aerospace Engineering
Georgia Institute of Technology

Dr. Ferri
School of Mechanical Engineering
Georgia Institute of Technology

Date Approved: August 13, 2020

The Child is the father of the Man

William Wordsworth

To my children

ACKNOWLEDGEMENTS

Anyone obtaining a PhD knows that it requires the help, work, effort, support, and tolerance of a large number of people. I am very grateful for the support of all those who have helped me in various ways.

I would like to start by thanking my advisor, Dr. Massimo Ruzzene, who helped direct my research, provided funding, and gave instruction in the field of elastic metamaterials. Working with him allowed me to see firsthand how research is conducted among the leaders in this field. I would also like to thank Dr. Michael Leamy who has acted as my advisor during the last year of my PhD, after Dr. Ruzzene moved to a new position at the University of Colorado Boulder. His help and encouragement made it possible for me to get to the finish line. I would also like to thank Mitsubishi Electric and Honeywell for funding portions of this research, with a special thank you to Washington DeLima at Honeywell for his contributions to the chapter on pulse shaping.

I am very grateful for the involvement and feedback of the other members of my committee, including Dr. Karim Sabra, Dr. Aldo Ferri, and Dr. Claudio Di Leo. I appreciate their feedback and guidance in improving the quality of my research.

An important thank you goes to the members of Dr. Ruzzene's wave lab, who I have thoroughly enjoyed working with. I would especially like to thank Raj Pal, now a professor at Kansas State University, for his insights into the bouncing electrode circuit breaker problem, and Matheus Nora Rosa, who helped get me up to speed on spectral element techniques. Also, a special thank you to Raffaele Manna, who along with being my labmate, was also my roommate prior to getting married, and became one of my best friends. Additionally, I would like to acknowledge Yiwei Xia, Romain Gerbe, and Luca De Beni; thank you for being so enjoyable to work with!

Without the support of my family my PhD would not have been possible. I appreciate the support and encouragement of my parents, Rick and Virginia Johnson, who are always

there for me. I want to thank my wife who has been very patient and supportive. While I have worked to finish my PhD she has supported our family financially. My PhD schooling has, at times, been a stressful experience for her, and I appreciate her support in finishing. My in-laws, Andrew and Helena, have been very encouraging. Helena's willingness to provide daycare for our young son made it possible for my wife and I to start our family while I've been working to finish. It wouldn't have been possible for me to complete my degree requirements without her willingness to do this. She has sacrificed her time and health to watch our son, and I am extremely grateful for this act of service.

I have been the beneficiary of a number of good mentors as I've worked on my PhD. Bob Chipman and Steve Smith always seemed to believe in me more than I believed in myself. Bob Chipman, who has since passed away, was an emeritus engineering professor from UCLA, always provided an encouraging voice. Steve Smith, a close family friend has provided a great deal of guidance in my personal life. I would not be who I am today without him. I also want to thank Terry Roberts for his mentoring and encouragement in navigating the challenges of academia and in determining my future career path.

There are two close friends who have been with me the entire time I've been at Georgia Tech. Brandon Carroll, who was working on his PhD in electrical engineering, lived directly across the street from me. We have enjoyed many games of tennis and pickleball together over the years. Anirudh Bhat had a cubicle in the same office as me when I started. I have enjoyed many long discussions with him about politics and appreciated having him as a running buddy.

Finally, I would like to thank my Heavenly Father. As a member of the Church of Jesus Christ of Latter-Day Saints, my faith is very important to me. I have felt God's guiding influence in my life, leading me to where he wanted me to be and helping me to become a better person. He has placed people in my path when I needed them, including many of those mentioned above. I would also like to thank one of my church leaders who I have especially appreciated. Bishop Steve Colton spent a great deal of time with me as I worked

through personal challenges.

TABLE OF CONTENTS

Acknowledgments v

List of Tables xii

List of Figures xiii

Chapter 1: Introduction 1

1.1 Overview 1

1.2 Background 1

1.3 Motivation and Objectives 5

1.4 Contributions 7

1.5 Work Organization 8

Chapter 2: Periodic Internal Resonators for Power Generator Support Vibration Mitigation 9

2.1 Overview 9

2.2 Introduction 9

2.2.1 Problem Statement 12

2.3 Power Generator Elementary Model 14

2.3.1 Model Description 14

2.3.2 Generator Modal Analysis 15

2.3.3 Generator Frequency Response 17
2.3.4 Generator Simplified Models 17
2.4 Concept - Mode Targeted Tuned Resonators 20
2.5 Concept - Base Isolation Using a Grounded Spring-Mass Chain 23
2.5.1 Spring Mass Chain Dispersion 24
2.5.2 Simple Spring Mass Chain Support 27
2.5.3 Implementation of a Spring Mass Chain Support on a Generator . . 30
2.6 Conclusion 33

Chapter 3: High Voltage Vacuum Circuit Breaker Bounce Mitigation 34

3.1 Overview 34
3.2 Introduction 34
3.2.1 Bounce Requirements 37
3.3 Basic Circuit Breaker Bouncing Model 39
3.3.1 Equations of Motion 42
3.3.2 D'Alembert's Solution 43
3.3.3 Calculating Reflections From Boundary Conditions 44
3.3.4 Finite Difference Solution 45
3.3.5 Calculating Bounce Duration 48
3.4 Circuit Breaker Bouncing Results 49
3.4.1 $\hat{k} \to \infty$ 49
3.4.2 $\hat{k} = 2$ 53
3.4.3 Analysis of Bounce Duration Results 58

3.5 Wave Characteristics for Bouncing and Dispersion 59

3.6 Conclusion 62

Chapter 4: Pulse Shaping in 1D Elastic Waveguides for Shock Testing 64

4.1 Overview 64

4.2 Introduction 64

4.3 Theoretical Background 66

4.3.1 Input and Output 66

4.3.2 Transfer and Dynamic Stiffness Matrices 69

4.3.3 Longitudinal Rod Governing Equation 74

4.3.4 Dynamic Stiffness Matrix 75

4.4 Parametric Studies 82

4.4.1 Phononic Crystal 82

4.4.2 Local Resonator 84

4.4.3 Grounding Springs 86

4.4.4 Exponentially Varying Cross Section 87

4.5 Optimization 88

4.5.1 Fitness Function 88

4.5.2 Analytical Model Optimization Results 89

4.5.3 Analytical Model Sensitivity Analysis 94

4.5.4 FE Optimization 98

4.6 Conclusion 108

Chapter 5: Conclusions and Contributions 110

5.1 Summary 110

5.2 Challenges and Constraints in the Practical Application of Elastic Metamaterials 112

5.3 Research Contributions 113

5.4 Recommendations for Future Work 114

5.4.1 Hopkinson Pressure Bar 114

5.4.2 Electrode Bouncing 115

5.4.3 Dispersion Optimization 116

5.4.4 Pulse Shaping Using Variable Cross-Section 116

References 122

Vita 123

LIST OF TABLES

3.1 Material properties used for assumed copper electrode. 38

3.2 Reduction in bounce duratio necessary to achieve a desired reduction in arc duration. 39

3.3 Nondimensional parameters governing the electrode bouncing problem. . . 40

4.1 Optimized parameter values for ramp type waves. 90

4.2 Optimized parameter values for longer ramp type waves. 92

4.3 Optimized parameter values for square type waves. 93

4.4 Optimized parameter values for ramp type waves using an FE model. 102

4.5 Optimized parameter values for longer ramp type waves using an FE model. 105

4.6 Optimized parameter values for dwell type waves using a FE model. 107

LIST OF FIGURES

2.1 Axial view diagram of a power generator. 12

2.2 Snapshots of undeformed generator shape (on left) and deformed shape of generator (on right) under rotating magnetic fields. 13

2.3 Generator FEA model geometry, boundary conditions, and loading. 15

2.4 The first 6 mode shapes for the power generator model. 16

2.5 Response of the generator base case (unmodified supports). 18

2.6 Simplification of second mode to a mass on a spring. 19

2.7 Simplification of third mode to a disk on two springs. 20

2.8 Generator model with tuned mass absorbers. 21

2.9 Generator model with tuned mass absorbers. 23

2.10 Support modified to include a spring mass chain. 24

2.11 Example of a grounded spring mass chain. 25

2.12 Nondimensionalized dispersion diagram for grounded spring mass chain, with stop bands shown in gray, target frequency in red, and dispersion relation in blue. 27

2.13 Analytical model of a grounded mass spring chain support, $m/M = 0.1$, N is the number of unit cells included in the chain. 28

2.14 Analytical model of a grounded mass spring chain support, $m/M = 0.004$, N is the number of unit cells included in the chain. 29

2.15 Application of the grounded spring-mass chain for the generator support. . . 31

2.16 Generator finite element model with grounded spring mass support (mesh not shown), zoomed in on grounded support shown on right. 32

2.17 Response of the generator with grounded spring mass chain supports. 32

3.1 Vacuum circuit breaker mechanical diagram. 36

3.2 Sample experimental data of bouncing circuit breakers electrodes with contact indicated by a high value and bounce indicated by a low value. 38

3.3 Simplified electrode impact model. 40

3.4 Characteristic diagram for displacement of rods for first bounce, with movable rod displacement being shown from values 0 to 1, fixed from 1 to 1.5, and parameters $\hat{k} = \infty$, $\hat{c}_2 = 0.56$, $\hat{L}_2 = 0.5$, $\hat{u}_b = 0$. 51

3.5 Characteristic diagram for displacement of rods for first bounce using finite difference derivatives, compare to Fig. 3.4. 51

3.6 Bounce duration for first bounce of the impacting rods, with $\hat{k} = \infty$ and varying $\hat{c}_2$ and $\hat{L}_2$. 53

3.7 Stress waves and ghost waves, indicated as the derivatives df or dg of the traveling wave displacements f and g that will result from reflections off of the spring and fixed ends at the time of impact, in the movable (solid) and fixed (dashed) rods for $\hat{k} = 2$, $\hat{u}_b = \frac{1}{2}\hat{v}_i\hat{L}_1$, $\hat{L}_2 = 0.5$, and $\hat{c}_2 = 0.56$. 54

3.8 Characteristic diagram of stress waves for $\hat{k} = 2$, $\hat{u}_b = \frac{1}{2}\hat{v}_i\hat{L}_1$, $\hat{L}_2 = 0.5$, and $\hat{c}_2 = 0.56$ 54

3.9 Bounce durations for $\hat{k} = 2$ and $\hat{u}_b = \frac{1}{2}\hat{v}_i$. 58

3.10 Example stress waves during bounce, indicated by df and dg, illustrating important wave characteristics that affect bounce duration. 59

3.11 Comparison of nondispersive wave and same wave, with dispersion relationship $k = \frac{\omega^{0.9}}{c}$, traveling in a rod. 61

4.1 Initial force and acceleration wave shapes. 67

4.2 Example output curve created from Eq. 4.5. 68

4.3 Example rod unit cell. 70

4.4 A finite rod composed of an arbitrary number of sections. 71

4.5 Coordinates and displacement for a longitudinal rod. 75

4.6 Example of a phononic crystal unit cell. 76

4.7 Example of a unit cell for a rod with periodically applied local resonators. . 77

4.8 Rod unit cell with a grounding spring. 78

4.9 Rod with an exponentially decaying cross-sectional area. 79

4.10 Unit cell combining both a phononic crystal and local resonance into a single elastic metamaterial. 81

4.11 Effect of change in the phononic crystal cross-sectional area on the output pulse shape. 82

4.12 Effect of change of relative section lengths in the phononic crystal on the output pulse shape. 83

4.13 Effect of phononic crystal unit cell length on the output pulse shape. 83

4.14 Effect of change in the resonator mass on the output pulse shape. 85

4.15 Effect of change in the resonator frequency on the output pulse shape. . . . 85

4.16 Effect of ground spring cut-off frequency on the output pulse shape. 86

4.17 Effect of different exponentially decaying cross-sectional areas on wave shape, with $\alpha = A(L)/A(0)$ being the ratio between initial and final cross-sectional areas. 87

4.18 Graphical representation of the error integration in Eq. 4.46 with the error to be integrated up to the end of the desired output curve, shown in gray. . . 89

4.19 Optimized wave shapes for ramp type desired outputs, with the top, middle, and bottom waves having $t_1 = 5/6\tau, t_2 = 1/6\tau$; $t_1 = 1/2\tau, t_2 = 1/2\tau$; and $t_1 = 1/6\tau, t_2 = 5/6\tau$ respectively, all with $T_d = 0$ (no dwell) as defined in Fig. 4.2. 91

4.20 Optimized wave shapes for longer rightward facing ramp type desired outputs, with the first wave $t_1 = \tau, t_2 = \tau$, the second $t_1 = 5/4\tau, t_2 = 3/4\tau$, the third $t_1 = 3/2\tau, t_2 = 1/2\tau$, and the fourth $t_1 = 7/4\tau, t_2 = 1/4\tau$, all with $T_d = 0$ (no dwell) as defined in Fig. 4.2. 93

4.21 Optimized wave shapes for dwell type desired outputs with the top, middle, and bottom waves having $t_1 = 1/3\tau, T_d = 1/3\tau, t_2 = 1/3\tau$; $t_1 = 1/4\tau, T_d = 1/2\tau, t_2 = 1/4\tau$; and $t_1 = 1/6\tau, T_d = 2/3\tau, t_2 = 1/6\tau$ respectively, as defined in Fig. 4.2. 94

4.22 Dispersion diagram of the optimized unit cell for the $t_1 = 1/3\tau, T_d = 1/3\tau, t_2 = 1/3\tau$ dwell wave, bandgaps highlighted in gray and imaginary portion shown as a dashed line. The transfer function amplitude is shown on a log scale in the colorbar with highest values in dark red of approximately $\log_{10}(1.8)$ and lowest values in dark blue as approximately $\log_{10}(0.005)$. . . 95

4.23 Dispersion diagram of the optimized unit cell for the $t_1 = 1/4\tau, T_d = 1/2\tau, t_2 = 1/4\tau$ dwell wave, bandgaps highlighted in gray and imaginary portion shown as a dashed line. The transfer function amplitude is shown on a log scale in the colorbar with the highest values in red as approximately $\log_{10}(1.5)$ and the lowest values in blue as approximately $\log_{10}(0.02)$. . . . 95

4.24 Dispersion diagram of the optimized unit cell for the $t_1 = 1/6\tau, T_d = 2/3\tau, t_2 = 1/6\tau$ dwell wave, bandgaps highlighted in gray and imaginary portion shown as a dashed line. The transfer function amplitude is shown on a log scale in the colorbar with red as approximately $\log_{10}(1.6)$ and the lowest values in blue as approximately $\log_{10}(0.03)$. 96

4.25 Sensitivity analysis for the pulse shaping technique, showing the effect of random variation in Young's Modulus on the pulse shape. 98

4.26 Sensitivity analysis for the pulse shaping technique, showing the effect of random variation in area on the pulse shape. 99

4.27 Various views of the unit cell geometry created from simplified combined unit cell shown in Fig. 4.10, with the far right view showing a cut-away view of a spring. 100

4.28 Nominal FE rod geometry composed of 9 unit cells as shown in Fig. 4.27 with wave propagation in the z-direction. 101

4.29 Optimized wave shapes produced by FE models for rightward facing ramp type desired outputs for waves (from top to bottom) $t_1 = 5/6\tau, t_2 = 1/6\tau$; $t_1 = 1/2\tau, t_2 = 1/2\tau$; and $t_1 = 1/6\tau, t_2 = 5/6\tau$. 103

4.30 Optimized geometries for, from top to bottom, the $t_1 = 5/6\tau, t_2 = 1/6\tau$; $t_1 = 1/2\tau, t_2 = 1/2\tau$; and $t_1 = 1/6\tau, t_2 = 5/6\tau$ ramp type waves. 104

4.31 Optimized wave shapes for, from top to bottom, the $t_1 = \tau, t_2 = \tau$; $t_1 = 5/4\tau, t_2 = 3/4\tau$; $t_1 = 3/2\tau, t_2 = 1/2\tau$; and $t_1 = 7/4\tau, t_2 = 1/4\tau$ ramp type waves. 105

4.32 Optimized geometries for, from top to bottom, the $t_1 = \tau, t_2 = \tau$; $t_1 = 5/4\tau, t_2 = 3/4\tau$; $t_1 = 3/2\tau, t_2 = 1/2\tau$; and $t_1 = 7/4\tau, t_2 = 1/4\tau$ ramp type waves. 106

4.33 Optimized wave shapes for, from top to bottom $t_1 = 1/3\tau, T_d = 1/3\tau, t_2 = 1/3\tau$; $t_1 = 1/4\tau, T_d = 1/2\tau, t_2 = 1/4\tau$; $t_1 = 1/6\tau, T_d = 2/3\tau, t_2 = 1/6\tau$ dwell type waves. 107

4.34 Optimized geometries for, from top to bottom $t_1 = 1/3\tau, T_d = 1/3\tau, t_2 = 1/3\tau$; $t_1 = 1/4\tau, T_d = 1/2\tau, t_2 = 1/4\tau$; $t_1 = 1/6\tau, T_d = 2/3\tau, t_2 = 1/6\tau$ dwell type waves. 108

SUMMARY

This dissertation is focused on the application of elastic metamaterials and phononic crystals to problems encountered in industry. The field of elastic metamaterials has experienced a large amount of development and is reaching a level of maturity where practical applications can be developed. In this dissertation three applied problems are addressed: the vibration mitigation of a large electrical generator; the impact and bouncing of circuit breaker electrodes; and the use of phononic materials for pulse shaping in Hopkinson bar tests.

Various base isolation techniques have been developed for heavy machinery. This dissertation looks at the problem of a vibrating electric generator and how phononic material concepts could be applied to mitigate vibrations. Two concepts are investigated: the first uses resonators tuned to the motion and natural frequency of the mode closest to the excitation frequency; the second technique replaces the previous support with periodically applied grounding springs. The frequency response obtained using both techniques show that they can attenuate the response at the excitation frequency. Finally, a practical implementation of grounding springs is presented.

High voltage vacuum circuit breakers have become the standard for industrial circuit breaker applications. Circuit breakers interrupt the flow of electricity through an electrical network, protecting it if the current flow becomes too high. When the electrodes in a circuit breaker close, initiating the flow of electricity, they bounce off of each other before reaching resting contact. During bouncing arcing occurs between the electrodes, which can lead to permanent welding of the electrodes and failure of the circuit breaker. Previously, the electrode bouncing problem has been studied using discrete lumped element models, with the underlying assumption that the bouncing was arising from resonance within the system. However, this perspective ignores wave propagation when impact occurs. In this dissertation a model of electrode bouncing, treating the electrodes as a continuous system,

is developed. The model shows how waves propagate through the bouncing electrode system, and helps illustrate what parameters control the bounce time. Wave bounce criteria are also suggested which could help reduce circuit breaker bouncing.

Hopkinson bar tests are used to obtain dynamic material properties such as strain rate dependent stress-strain relationships. This is accomplished by sending a mechanical shock wave, or pulse, down the bar and into the material sample to be tested. Parameters such as amplitude, shape, and duration of the wave are important in obtaining the desired material properties. The research presented in this dissertation shows that through using optimized elastic metamaterial concepts, an input pulse to a longitudinal bar can be shaped to sufficiently approximate a specified, predefined output pulse. Concepts including local resonators, phononic crystals, grounding springs, and cross-sectional variations were investigated. These concepts are applied to a homogeneous rod and analyzed using the transfer matrix technique. The output of a metamaterial rod is predicted using the dynamic stiffness matrix. The metamaterial parameters for a combined phononic crystal - local resonator are then tuned using an optimization algorithm to achieve the desired response of the system.

These applications demonstrate three scenarios where phononic materials can be applied to industrial problems, for vibration mitigation and pulse shaping. The generator vibration mitigation problem investigates phononic material techniques that would maintain the static stiffness required to support the generator. The circuit breaker problem develops a new model for bouncing that clarifies the role of wave propagation, suggesting that phononic materials could be used to modify the wave shape in a beneficial way. The Hopkinson bar problem, which had similarities to the circuit breaker problem, develops this concept further, resulting in pulse shaping using phononic materials. This is a novel application.

Based on the work presented here a number of different design techniques could be pursued to push the boundaries of these applications even further. The pulse shaping technique was developed looking at the acceleration profile of a wave. This could be developed

for stress, strain, or velocity as well as similar Hopkinson bar tests using tension or torsional waves. The same technique could also be used to optimize a phononic material for a different quantity, such as the energy distribution in the system. One other avenue of development could look at optimizing the bar cross-sectional area to shape the pulse traveling through the system.

CHAPTER 1
INTRODUCTION

1.1 Overview

This dissertation is focused on the application of phononic materials to problems encountered in industry. Three main problems are addressed: vibration mitigation for a large electrical generator; the modeling of impact and bouncing of circuit breaker electrodes; and pulse shaping using phononic materials for Hopkinson bar tests. Previous research in the field of elastic metamaterials has focused on introducing band gaps to block the propagation of waves at particular frequencies. Through various techniques wave directionality, focusing, or topological modes can be introduced into a structure. A large variety of phononic material concepts and analysis techniques are available in the literature, but so far a limited number of practical applications for elastic metamaterials have been developed. In addressing the problems described above, this dissertation expands the practical application of phononic materials. To this end, this dissertation discusses the modeling of waves created by impact, phononic material techniques to mitigate vibration, modeling techniques to obtain dispersion relationships and predict wave shapes, and techniques to obtain geometry optimized for dispersion. This chapter provides a general review of elastic metamaterials and phononic crystals, problem motivation and objectives, and an outline of the dissertation.

1.2 Background

General background on elastic metamaterials is reviewed here. Because the problems examined in this dissertation have unique backgrounds, problem specific literature is reviewed at the beginning of each chapter. Two important developments in the field of phononic ma-

terials has allowed the discipline to progress to where it is today. In the 1970's observations about wave propagation in periodic [1] or periodically stiffened structures [2] was the first important development, which has since been termed phononic crystals. Later, locally resonant crystals that created subwavelength bandgaps in structures were developed. This allowed for the creation of frequency stop bands at much lower frequencies than could be achieved with material periodicity [3]. Structures using designed local resonance have been termed elastic metamaterials.

The theoretical development of elastic metamaterials has generated a wide range of concepts. For example, in transversely vibrating beams low-frequency bandgaps were opened using a variety of methods, including periodically applied spring mass resonators with both torsional and translational components [4] and mass resonators with two translational degrees of freedom [5]. Local resonators were applied to beams and rods using using additional beams as springs [6], as well as continuum resonator beams attached via a Winkler foundation [7].

When local resonators were applied periodically they created bandgaps due to the resonance frequency and the periodicity of the structure [8]. When the frequency of the periodically applied resonators is tuned to match the bandgap frequency created by the periodicity, even wider bandgaps are produced [9]. Masses were also mounted on two springs resulting in resonators with both translational and rotational degrees of freedom [5], effectively creating low frequency bandgaps on transversely vibrating structures. A somewhat similar concept coupled the resonators from adjacent unit cells, resulting in two-degree of freedom motion of the resonators, leading to a unique band structure and directional wave response [10]. Instead of coupled degrees of freedom, one technique tuned resonators to different resonant frequencies around a frequency range of interest. The stiffness was optimized to provide the highest degree of attenuation, resulting in attenuation spanning the entire frequency range of interest [**reich**, 11].

Additional techniques looked at designing resonators which contained a rigid mass sur-

rounded by a softer material acting as a spring [12]. This resulted in three degree of freedom resonators which could attenuate both transverse and longitudinal waves. Another interesting technique used what has been termed inertial amplification. Inspired by the development of the inerter [13], inertial amplifiers basically use the mechanical advantage created by a mass on a lever to make it behave as if it were more massive than it actually is. When the inertial amplifier is used periodically, as an elastic metamaterial, it results in wide low frequency bandgaps [14]. This concept has been successfully applied to continuous structures [15] and has been the subject of topology optimization for enhanced bandgap width [16].

Elastic metamaterials have the ability to create what has been termed a negative effective mass or stiffness [4], which can be used to counteract externally applied forces on a system. A double negative elastic metamaterial has both a negative effective mass and stiffness. One design of a double negative elastic metamaterial resulted in a stopband for both longitudinal and transverse waves, as well as a negative Poisson's ratio [17], opening up the possibility of negative refraction or the inverse Doppler effect. Double negative elastic metamaterials were also created using an analogy from electric circuit networks, achieving a wider bandgap than could be created by only negative mass or stiffness [18].

Other interesting concepts have also been developed, such as metamaterials used to create an anisotropy that corrected dispersion of waves in an elastic waveguide [19]. Shape memory alloys were used to create temperature dependent bandgaps for vibration isolation [20]. Elastic metamaterials were also used to create topologically protected wave modes, resulting in waves which can follow specific paths through a material [21].

Lattice structures have also been used to create phononic materials. Periodic honeycomb structures have been found to exhibit a variety of different effects including wave beaming [22]. A wide variety of lattices, such as hexagonal, triangle, and square honeycomb lattices, as well as Kagome lattices, were also analyzed. The different lattices types exhibit a designable band structure based on properties such as material density, or slender-

ness ratio of the the constituent beam members [23]. Using a mass supporting rubber lattice embedded within a transversely vibrating frame, a high-stiffness, high-damping structure was designed which created low frequency bandgaps [24]. Inertial amplifiers were also deployed in an array to create an elastic metamaterial lattice with a wide bandgap [25].

Along with the development of a wide variety of concepts, analysis techniques have also been developed or repurposed for use in elastic metamaterials. The typical analysis for an elastic metamaterial applies the Bloch theorem to a single unit cell of a crystal, which relates the displacements at opposing edges of a unit cell through a phase shift [26]. The resulting equation is often solved using a simple plane-wave expansion. Transfer matrices were developed very early in the study of periodic systems, creating a simple mathematical way to analyze structurally complex configurations of periodic structures [27]. A more recent example of transfer matrix use is in [7]. A similar technique uses spectral elements to determine the dispersion relationship for wave propagation in beams [8]. In [23] the finite element (FE) method was used to construct the mass and stiffness matrices for a unit cell composed of Timoshenko beams. Then periodic boundary conditions were applied and the dispersion relationship was found by solving the eigenvalue problem. For more complex geometry which cannot be modeled with simple beam elements a technique using commercially available FE software was developed to apply periodic boundary conditions for a specific wave number and then use a modal analysis step to extract the corresponding frequencies, determining the dispersion relationship [28].

All of the previous techniques assumed periodic boundary conditions. Periodic boundary conditions presuppose an infinitely repeating periodic lattice. The analysis of finite periodic systems is important for the implementation of periodic elastic metamaterials. Development of analysis techniques for finite periodic structures also occurred very early in the field. For example, reference [29] demonstrated a way to calculate the natural frequencies of a finite periodic system and showed that these natural frequencies fall outside of the stop bands of the structure. More recently, a technique assuming an infinite number

of resonators on a finite beam was developed to derive the dispersion relationship [30]. The response to an infinite number of resonators was shown to be adequately approximated by as few as five resonators, depending on the composition of the system.

The background presented in this section has discussed the development of elastic metamaterial topics including resonators on rods and beams, lattices, and analysis techniques. It has covered some of the important developments in the field of elastic metamaterials, but is not comprehensive. For example, it has not discussed nonlinear elastic metamaterials which were not considered for this dissertation. For a more comprehensive review of what has previously been accomplished using elastic metamaterials see [31].

1.3 Motivation and Objectives

Section 1.2 demonstrates that there has been a large amount of development in the field of elastic metamaterials and a wide variety of concepts from which to draw for the design and analysis of elastic metamaterials. During the review of elastic metamaterials literature a limited number of elastic metamaterial applications for industry were found. Two such applications include periodically applied rotational resonators for the seismic isolation of buildings [32] and the use of spherical granules to create a vibration mitigating support [33]. The contact of the granules with the walls of the support results in a high pass mechanical filter. Because of the wide variety of ideas from which to draw in the elastic metamaterial literature, this field of study is beginning to reach a level of maturity where applications can be developed.

The purpose of this dissertation is to push the boundaries of the application of elastic metamaterials and demonstrate their practical use. Because of this the broad objective of this dissertation was to find ways to apply elastic metamaterials to three industry problems, vibration mitigation for heavy machinery, bounce reduction of impacting circuit breaker electrodes, and pulse shaping for Hopkinson bar tests.

Elastic metamaterials are a natural choice to consider for vibration mitigation problems,

because they have the possibility of making minimal modifications to heavy machinery support structures while introducing frequency bandgaps that could result in attenuation of the vibration to be mitigated. For the problem of vibration mitigation for heavy machinery there are a couple of technical challenges which need to be considered. Often heavy machinery operates at relatively low frequencies. Also, because it is heavy, statically stiff supports are required to hold it. Under these requirements, a vibration mitigation solution will need to be able to maintain a static stiffness while also being tuned to lower frequencies which typically would require more massive resonators to provide effective attenuation. For this problem solutions that mitigated vibration and addressed these design constraints were explored.

The other two problems, bounce reduction of electrodes and pulse shaping for Hopkinson bars, although very different applications, have similar phenomena underlying them that can be addressed by the same elastic metamaterial solution. In high-voltage vacuum circuit breakers, when the electrodes close to allow the flow of electricity they impact causing elastic waves to propagate through them. These waves reflect off of the various surfaces within the electrodes and return to the impact interface. When the waves combine at the interface under the right conditions the electrodes lose contact, that is they bounce. For a typical closing event the electrodes bounce multiple times before achieving resting contact. During this bouncing electrical arcing occurs which degrades the contact surface of the electrodes. If the bouncing were modified to create shorter duration bounces the arcing could be significantly reduced and the circuit breaker life could be extended. However, the bouncing phenomenon is nonlinear, and previous models have not clarified the underlying mechanisms leading to the bouncing. For this problem the underlying causes for the bouncing were explored further. Motivated by this lack of understanding, the objective of this project was to create a model that provided a greater fundamental understanding of the bouncing phenomenon, so that the bounce reduction could be addressed in a more systematic way.

Hopkinson bar tests are used to measure dynamic material properties. This project is specifically interested in shock testing of accelerometers. In the test a pulse is created by an impacting rod striking the Hopkinson bar, similar to the bouncing electrodes when they first make contact. However, in the Hopkinson bar the bounce after impact is not of interest. The bar directs the pulse into the object to be tested. The shape of the pulse is the important aspect of this problem. Different pulse shapes can be used to provide additional information about the dynamic properties of the system. In a typical Hopkinson bar the shape of the pulse is a product of the velocity and length of the impacting rod. Usually the Hopkinson bar is designed to prevent wave dispersion and maintain the shape of the wave pulse. Instead, this project considered intentionally introducing dispersion into the Hopkinson bar, in a controlled manner, to cause the output pulse to change into a desired shape for testing as it traveled through the bar. Because phononic materials are known to introduce dispersion and bandgaps, they seemed like a likely candidate to shape the input pulse in a controllable way. However, elastic metamaterials have not been used for pulse shaping before. As a result, it was necessary to explore how elastic metamaterials would change the shape of waves traveling through them, as well as determine the necessary characteristics to successfully accomplish this.

1.4 Contributions

This dissertation contributes to the field of elastic metamaterials in four different ways:

1. It explores the application of elastic metamaterials to heavy industrial equipment, and demonstrates mode targeted resonators and grounding springs attached to the supports.

2. It proposes a new analytical model for the bouncing of circuit breaker electrodes after closing. Prior work on this subject has treated the electrodes as discrete element systems. This oversimplified treatment made it difficult to understand the factors that

controlled the bounce duration. The new model clarifies these factors.

3. It develops and refines a novel technique to shape pulses in 1D rods. Previous elastic metamaterials have focused on controlling the bandgaps the metamaterials introduce, but have not taken advantage of the effect introducing the bandgap has on the dispersion of the waves. The change in dispersion has not yet been used in a controlled way to accomplish something such as shape pulses traveling through a metamaterial.

4. It demonstrates the geometry and implementation for the pulse shaping technique in a physically realizable structure.

1.5 Work Organization

This dissertation is organized into five chapters. Chapter 1 provides general background information for elastic metamaterials, motivation, and contributions. Chapter 2 examines the vibration of an electric generator and the application of internal resonators and grounding springs applied to the supports as vibration mitigation techniques. Chapter 3 describes the circuit breaker electrode bouncing problem. It introduces a new model treating the electrodes as continuous rods and demonstrates how wave propagation within the structure governs the bouncing phenomenon. Chapter 4 presents the Hopkinson bar pulse shaping problem. It describes the Hopkinson bar experiment, presents results on different phononic materials capabilities to change the shape of a wave, and presents an optimization routine which successfully finds geometry for the shaping of predefined pulse shapes. Chapter 5 summarizes the work presented, describes some of the challenges in applying elastic metamaterials to practical problems, and puts forward some suggestions for future work.

CHAPTER 2
PERIODIC INTERNAL RESONATORS FOR POWER GENERATOR SUPPORT VIBRATION MITIGATION

2.1 Overview

This chapter presents research on vibration mitigation for large electric generators. The results are applicable to other heavy rotating machinery. Two vibration mitigation concepts were investigated. The first employs resonators tuned to the natural frequency of the mode closest to the excitation frequency. The second technique replaced the previous support with a metamaterial support composed of periodically applied grounding springs. The frequency response of the systems shows both can significantly attenuate the excitation frequency. Finally, a practical implementation of the grounding springs is analyzed using finite element analysis (FEA).

2.2 Introduction

Massive power generators introduce a large amount of vibration into their operating environment. The mitigation of vibration in power generators and other heavy machinery poses a difficult problem. Because these machines have a large mass, they must be placed on statically stiff supports. They also often have low operating frequencies. Vibration can be passed through the machinery support, which acts like an elastic spring, to the floor or base of the structure the machine is mounted to.

One of the simplest ways to reduce transmitted vibration is by mounting the heavy equipment on an inertia block. The massive inertia block effectively increases the mass of the system, causing a downward shift in the system's natural frequency and a reduction in velocity. Assuming that the operating frequency is above the natural frequency of the

system, this results in a greater amount of attenuation at the operating frequency [34]. The drawback to this technique is that it results in a large increase in mass, which in many cases can be prohibitive.

Another technique, used to reduce the large amount of mass while still effectively attenuating the transmitted vibration, is to use a levered mass. Instead of a large inertia block, a lever mechanism, with a mass mounted at the end, is placed in parallel with the elastic supports of the structure [35]. The effective inertia of the levered mass can be increased by exploiting the mechanical advantage of the lever. This results in smaller masses providing attenuation at very low frequencies.

Sometimes, instead of adding an inertia block or additional support mechanisms, it might be desirable to make a direct modification to the structure of the elastic support itself. Theoretically, elastic metamaterials offer strong potential benefits, given their ability to generate sub-wavelength frequency bandgaps, while being integrated into the support structure [8]. Assuming that the support is in the form of a stiff elastic spring, such as an iron rod, there are several elastic metamaterial concepts to choose from. For example, replacing the elastic support with a mass spring chain with equivalent static stiffness results in higher stop band attenuation than could be achieved using a massive inertia block [36]. Adding internal resonators to each individual mass on the chain can increase attenuation even further. However, each additional mass introduces another resonance. This means that the cut-off frequency is pushed higher, making this technique difficult to implement when attenuation at low frequencies is desirable. One variation to this approach examined holding the mass constant, but creating a spectrum of resonant frequencies around a natural frequency of interest [37, 11]. This technique provided a wider but shallower attenuation zone than a periodically applied resonator tuned to a single frequency would have. Another variation to the mass chain technique involves replacing the masses with levered masses in parallel with the springs. This concept results in lower stop-band frequencies than the spring-mass chain [38], but still leads to an overall increase in the cut-off frequency.

A limitation to these approaches is that the attenuation, and the effective lower range, of each of these concepts, is dependent on the resonator mass to beam stiffness ratio. For transverse beam vibration the beam stiffness is typically much lower than that for longitudinal beam vibration, so elastic metamaterials used for transverse vibration at low frequencies are relatively easy to design compared to longitudinal vibration. This can be problematic when the beam is excited in both longitudinal and transverse directions from machine vibration.

Most metamaterial structures create a mechanical band stop filter, with the overall goal being to move the stop band to the lowest frequency range possible. A transversely vibrating beam with a periodic elastic boundary presents an interesting alternative. As the stiffness of the elastic boundary increases, a band gap with an initial frequency of zero emerges [39]. In other words, the elastic boundary results in a high pass filter. The same can be done for a longitudinally vibrating beam, which may be useful in vibration isolation applications. One way this has been carried out is by using a chain of granular media, embedded within a rod. The rod acts like the grounding spring, and the metal, or plastic beads effectively become a nonlinear load-bearing high pass filter [33]. However, granular media are also limited in their load bearing capacity, with the potential to deform plastically.

The purpose of this chapter is to introduce two concepts to address the vibration of heavy machinery, with a large generator being used as an example of how they can be applied. The first technique targets resonators to the natural frequency and rotational motion of an important contributing mode of the system. Instead of being placed on the supports, these resonators are placed directly on the body of the generator. The second technique modifies the support to include a grounded spring mass chain, which is known to behave as a high pass filter, in such a way that the static stiffness is maintained, but the dynamic stiffness at the frequency of interest is reduced. This technique is analyzed using both a lumped mass model and an FE model. FE designs taking into account space limitations will be presented.

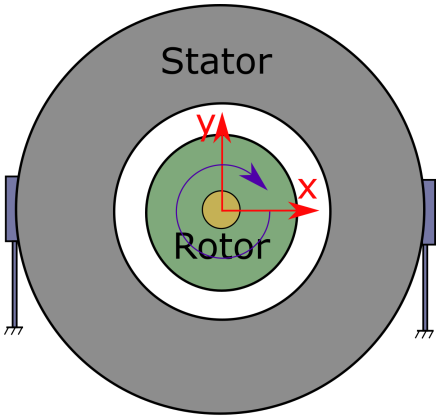

Figure 2.1: Axial view diagram of a power generator.

2.2.1 Problem Statement

Power generators convert mechanical energy into electrical energy based on the Faraday principle, which states that magnetic flux in an electric circuit will induce an electrical current. The two main parts of a generator used to accomplish this are the stator and the rotor. Figure 2.1 provides a simple diagram showing this. The stator typically has magnets inside of it which generate a magnetic field. The rotor has a number of wire windings. When the rotor spins, the change in magnetic flux through the wire windings induces an electrical current.

To cause the rotor to spin, a turbine or internal combustion engine, is used to convert other sources of energy into rotational mechanical energy. The rotational element of the turbine is then attached to the shaft of the generator, shown in yellow in Fig. 2.1, causing the turbine to spin. For example, in a typical nuclear reactor, heat from the nuclear reaction is used to generate high pressure steam which drives the turbine. The spinning of the turbine causes the generator rotor to rotate in the magnetic field, and electricity is generated.

An additional magnetic field is also induced by the electric current in the rotor. This magnetic field is very strong, and can deform the generator stator, in the manner shown in Fig. 2.2. The rotor rotation results in a rotating deformation of the stator at twice the frequency of the spinning rotor, which also results in a deformation of the generator supports.

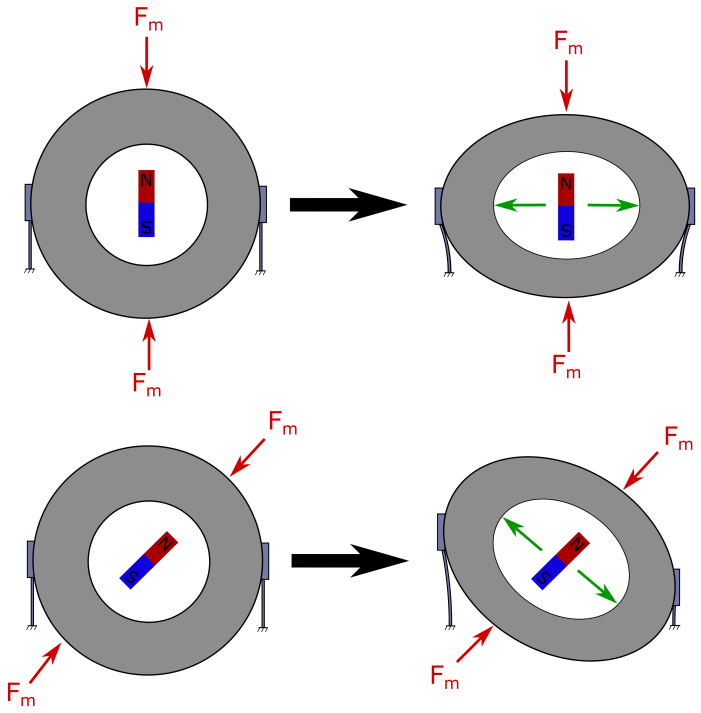

Figure 2.2: Snapshots of undeformed generator shape (on left) and deformed shape of generator (on right) under rotating magnetic fields.

This deformation leads to vibration of the supports in both the longitudinal and transverse directions. The longitudinal vibration of the supports leads to sound and vibration in the working environment of the generator. This work is concerned particularly with mitigating this longitudinal vibration to reduce the sound and vibration transmitted to the environment.

In the generator, the magnetic field spins with the rotor at a frequency of $1/2f_m$ Hz (typically 50 or 60 Hz depending on the country), resulting in a deformation as shown in Fig. 2.2 rotating at a frequency of f_m. Because this excitation induces noise in the operating environment, this research seeks to attenuate this vibration. This needs to be accomplished while at the same time maintaining the transverse and static stiffness of the supports. Because phononic material concepts have not been exhaustively explored for similar applications, the design space for this problem will be restricted to phononic material solutions. These offer the potential to provide a simple solution without requiring a

complete redesign of the entire structure of the generator, as some other solutions would.

2.3 Power Generator Elementary Model

Prior to designing supports for the generator, an FE model was developed to capture the key physics of the vibrating generator. This model was developed based on geometry information provided by the research sponsor. It was validated by comparing the modal and frequency response to modal and frequency response data provided by the research sponsor. Analytical lumped element models for the highest contributing modes of the system were then created to simplify the development of vibration mitigation techniques.

2.3.1 Model Description

The generator FE model and mesh is shown in Fig. 2.3. Because the generator is composed of a long cylindrical mass motion in the z-direction is constrained, therefore linear plane strain elements provide an adequate approximation of the generator behavior. The idealized generator can be treated as a cylindrical mass resting on two elastic supports. These supports attach to the generator at approximately its equator, and then go to mechanical ground. The spinning of the rotor results in vibration in the x-y plane with no deformation or motion along the axial direction. This research applies these assumptions for all FE models presented for the generator, unless otherwise specified.

Specific information about the size and mass of the rotor was not provided by the research sponsor, therefore the rotor was not modeled. Instead, the research sponsor provided proprietary information about the load created by the rotating magnetic field. This load was applied as a rotating pressure load on the inner surface of the stator. This was used for the calculation of the frequency response of the generator. The net effect of the load, shown Fig. 2.3, produces an oscillating vertical force and axial moment moment about the center of the generator.

Both of the supports connect the generator to ground. The base of each support was

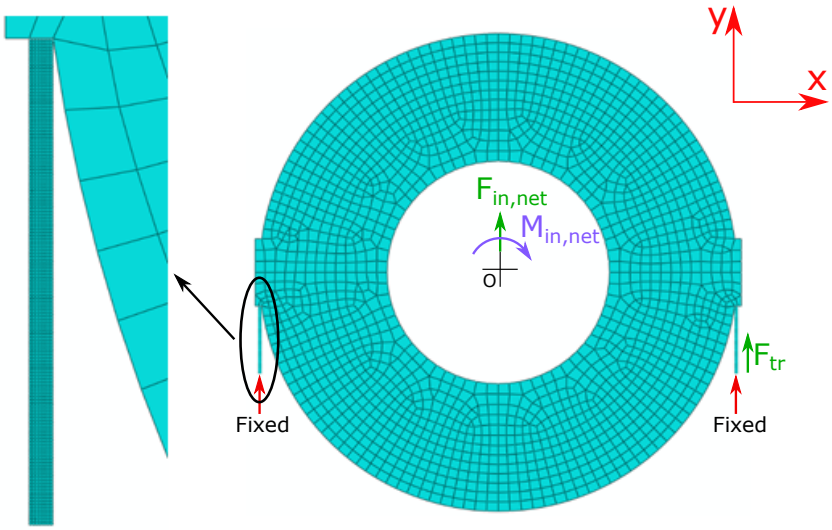

Figure 2.3: Generator FEA model geometry, boundary conditions, and loading.

fixed in all degrees of freedom to simulate the connection to the generator foundation. For the force transmitted by the supports to ground the reaction forces at the nodes on the base of the right support were summed to get the total force through the support. This is shown as F_{tr} in Fig. 2.3. The reaction forces through the right support in the y-direction are used for all models, to allow for a consistent comparison.

2.3.2 Generator Modal Analysis

Prior to designing vibration mitigation supports for the generator, vibration mThe first 6 modes of the generator are shown in Fig. 2.4, with arrows showing the direction of motion for each mode. In the first three modes the stator body does not deform, while the supports do. The first mode is analogous to transverse beam vibration with a mass at the end. In this mode the stator moves as a rigid body from side to side, horizontally. The second mode is analogous to longitudinal beam vibration with a mass at the end. In this mode, the stator moves as a rigid body in the vertical direction. In the third mode, the stator rotates as a rigid body about its center while the supports are stretched or compressed alternately. Although the motion of the stator is different in the second and third modes, the motion of

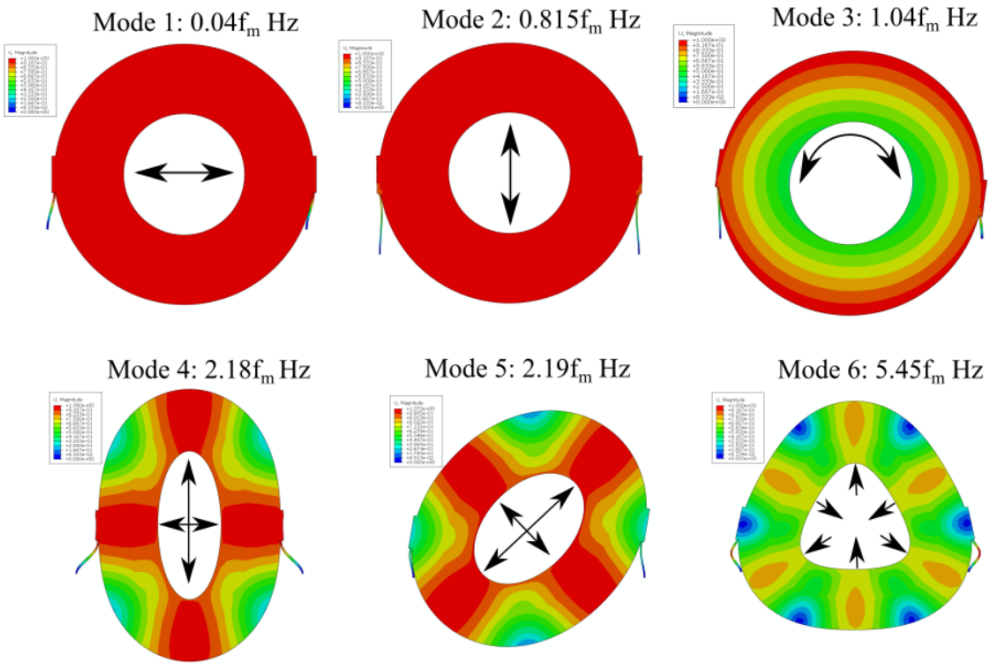

Figure 2.4: The first 6 mode shapes for the power generator model.

the supports is similar. Both modes lead to compression and tension of the supports in a comparable manner. The fourth, fifth, and sixth modes all include deformation of the stator. In the fourth mode, the sides are alternately compressed or stretched, exciting the supports in a transverse manner. The fifth mode is very similar to the fourth mode, only rotated by 45^o. This leads to excitation of the supports in both the transverse and longitudinal directions. In the sixth mode a triangular shape is created by the stator, with the sides and corners alternating between pushing in or pulling out. This mode also excites the supports in a transverse and longitudinal way.

The natural frequencies predicted by this model have less than a 3% difference with those provided by the research sponsor. Although not perfect, the natural frequencies are close enough to provide confidence that this model is capturing the primary physics of interest in the vibration of the power generator, and that the model can be used for further development of vibration mitigation techniques.

The first mode and the fourth, fifth, and sixth modes, were provided here to show val-

idation of the model. In attenuating the longitudinal excitation at a frequency of f_m Hz the second and third modes are of primary interest for two reasons. The first reason is that they are the two closest modes to the frequency of vibration, and therefore will be the largest contributors to the response at that frequency. The second reason is that both of these modes involve longitudinal deformation of the supports, and thus are contributors to the longitudinal excitation which the supports experience.

2.3.3 Generator Frequency Response

The frequency response of the generator, presented as the y-component of the reaction force through the right support, is shown in Fig. 2.5 using the loading described in Sec. 2.3.1. The response was normalized by the natural frequency of mode 3, the first rotational mode of the system. It was normalized by this frequency because this frequency is closest to the excitation frequency of interest, f_m, and because this mode dominates the response of the system.

The first resonance of the response shown in Fig. 2.5, appears at approximately $\omega/\omega_{rot1} = 0.8$. This resonance is mode 2 as shown in Fig. 2.4, the first longitudinal vibrational mode of the system. The first mode of the system, which has motion mainly in the transverse (i.e. x) direction occurs at a lower frequency, but does not appear in this response because the transverse nature of the mode did not result in any reaction forces in the y-direction. This resonance occurs at a frequency much lower than the frequency range of interest, and so was ignored in the analyses presented here. This model captures all of the key components of the frequency response provided by the research sponsor, especially at the excitation frequency.

2.3.4 Generator Simplified Models

As stated previously, this research seeks to develop a phononic material concept which attenuates the longitudinal (y direction) vibration at the generator operating frequency.

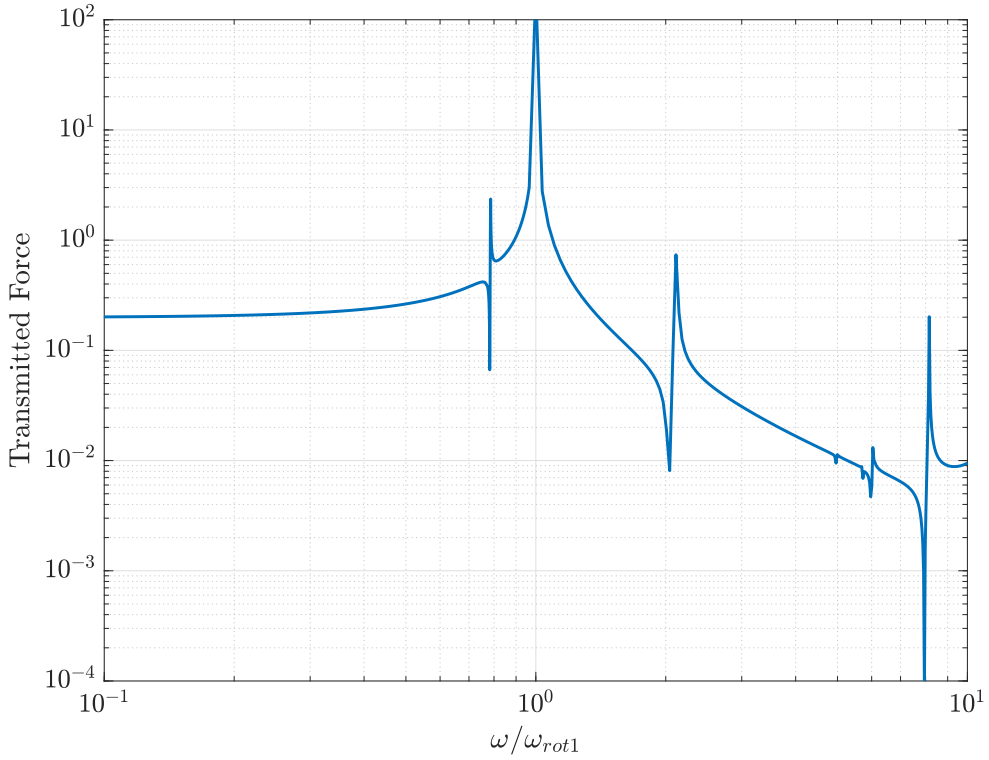

Figure 2.5: Response of the generator base case (unmodified supports).

Models of the generator which isolate the key physics of interest simplify the design process needed to address this excitation, by eliminating information about unimportant phenomenon. Although the FE model presented is already fairly simplified, even simpler models are developed here for the second and third modes. These modes both include longitudinal vibration of the supports, and provide the greatest contribution to vibration at the excitation frequency. Models that focus on these two modes make it easier to develop phononic materials that target their motion and will therefore be most effective at attenuating the generator response to the excitation frequency. These models can then be used as design tools for developing metamaterials concepts to address the particular excitation of interest in this problem.

From examining the second and third modes, for the longitudinal vibration of the system the supports act like springs with a stiffness

$$k_s = AE/L \tag{2.1}$$

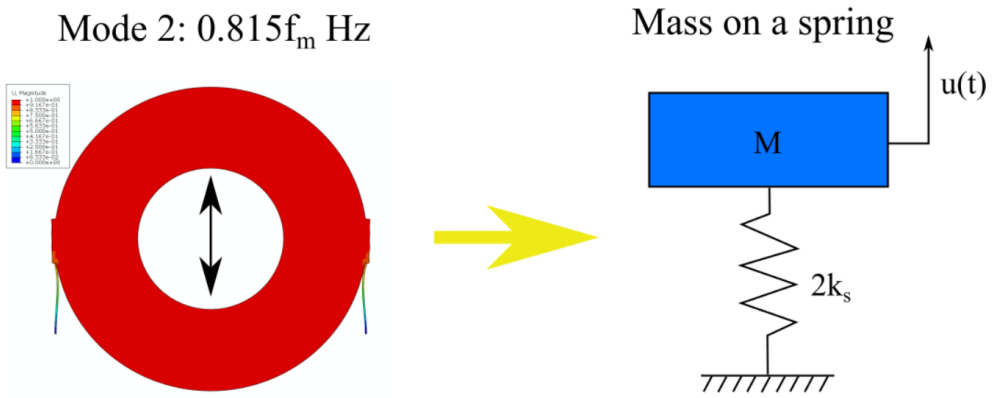

Figure 2.6: Simplification of second mode to a mass on a spring.

where A is the cross-sectional area of the support, E is the Young's modulus, and L is the length of the support. The main generator body (stator/rotor) acts like a distributed rigid body mass. A streamlined analytical model can be created for each of these modes which isolates their physics using these simplifications.

The second mode behaves like a mass on a spring. This simplification is shown in Fig. 2.6. In this case the mode has been reduced to a single degree of freedom system, with vertical displacement $u(t)$. Using the generator mass, included as M, and support stiffness $2k_s$ for the two supports acting as springs in parallel, the natural frequency was 96.3% that of the second mode, less than 4% error from that predicted by the FE model. This confirms that this simplification is a close enough approximation to be useful for design purposes, for the second mode.

The third mode behaves like a rotating disk on two springs. This simplification is shown in Fig. 2.7. The mass of the generator is given by M, rotational inertia by I, and outer radius by R. This model has one degree of freedom, θ, the rotation about the center of the disk. The vibration of the stator would be induced by the rotor, which is included here only as M_{in}, the input moment. The natural frequency for this model has less than 1% difference between that of the FE model. The similarity of the model to the third mode makes the model a useful approximation for design purposes as well.

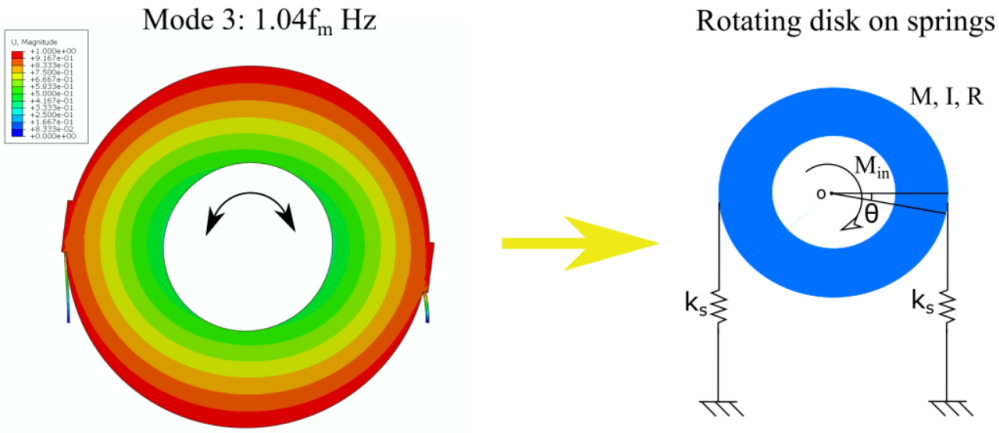

Figure 2.7: Simplification of third mode to a disk on two springs.

2.4 Concept - Mode Targeted Tuned Resonators

The first concept presented in this research is developed on the simplified model for the third mode – the disk on springs. Applying Newton's second law and summing moments about the origin O of the disk leads to the equation of motion

$$I\ddot{\theta} + 2k_s R^2\theta = M_{in} \tag{2.2}$$

with the natural frequency

$$\omega_n = R\sqrt{\frac{2k_s}{I}}. \tag{2.3}$$

The generator has now been reduced to a single degree of freedom model with only a single resonance. One way to address the vibration of the generator at this resonance is by adding tuned vibration absorbers to the outside of the generator, as shown in Fig. 2.8. In this case the resonator masses m_r, are mounted to the generator using slender flexible bars of length l_r, with stiffness k_r. The stiffness of the bar can be easily controlled by modifying its cross-sectional properties.

To model the resonators, each is assumed to move through a rotation $\theta_r - \theta$, relative to the rotation of the generator. Each individual resonator is assumed to have the same

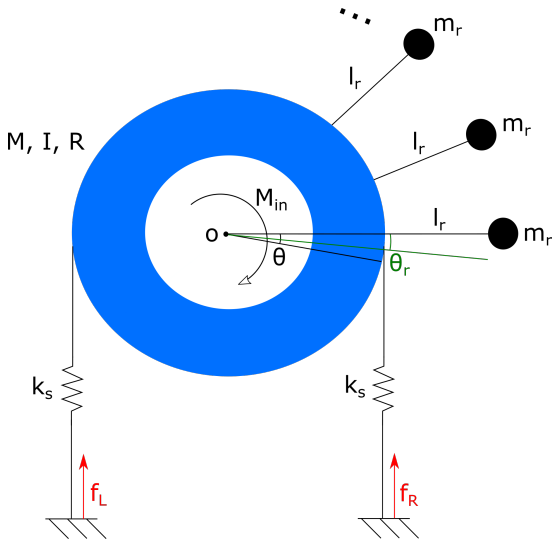

Figure 2.8: Generator model with tuned mass absorbers.

properties and therefore the same rotational displacement. These assumptions lead to the equation of motion for each resonator, of

$$m_r(R+l_r)^2\ddot{\theta}_r + k_r(R+l_r)l_r(\theta_r-\theta) = 0 \tag{2.4}$$

where the natural frequency of the tuned absorbers, is given by

$$\omega_r = \sqrt{\frac{k_r l_r}{m_r(R+l_r)}}. \tag{2.5}$$

The equation of motion, Eq. (2.2), with the added tuned absorbers becomes

$$I\ddot{\theta} + 2k_s R^2\theta + Nk_r(R+l_r)l_r(\theta-\theta_r) = M_{in} \tag{2.6}$$

where N is the total number of tuned absorbers used.

Assuming time harmonic motion, Eq. (2.4) can be solved for θ_r and then subbed into

Eq. (2.6) to get an expression for θ of

$$\theta \left[2k_s R^2 - \omega^2 \left(I + N \frac{m_r (R + l_r)^2}{1 - \frac{\omega^2}{\omega_r^2}} \right) \right] = M_{in}. \tag{2.7}$$

By adding the resonators in this manner the specific rotational mode of interest can be targeted. The tuned resonators increase the effective inertia of the system, seen in the term in round brackets in Eq. (2.7). This shifts the natural frequency of the generator, and also provides attenuation at the natural frequency they are tuned to.

Of particular interest is the attenuation of force transferred to ground through the supports, shown as f_l and f_r in Fig. 2.8. Since the amplitude of these forces is the same, it is only necessary to examine one of these forces. Assuming that the generator rotates through small angles, the force transmitted through the right support is given by

$$f_{tr} = k_s \theta R \tag{2.8}$$

or

$$\frac{f_{tr}}{M_{in}} = \frac{k_s R}{\left[2k_s R^2 - \omega^2 \left(I + N \frac{m_r (R + l_r)^2}{1 - \frac{\omega^2}{\omega_r^2}} \right) \right]} \tag{2.9}$$

The frequency response of the generator, both without (base case, Fig. 2.7) and with resonators, is shown in Fig. 2.9 for an example case of a 25 metric ton mass with 40 evenly spaced 10 kg resonators attached. The resonator mass to generator mass ratio is 1.6%. In this example, the resonators are tuned to the assumed excitation frequency to be attenuated of 100 Hz. The resonators provide more than two orders of magnitude attenuation at the operating frequency, and provide a band gap width of 10.5 Hz. This shows that using this concept, and by designing resonators to target the specific structural motion of interest, small amounts of mass can effectively provide attenuation.

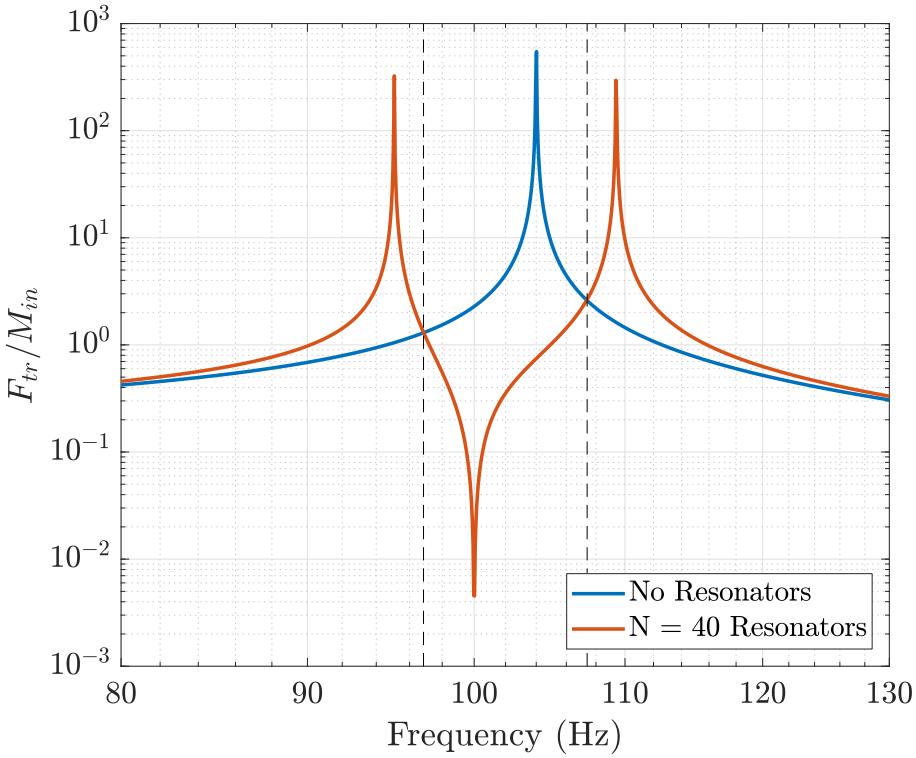

Figure 2.9: Generator model with tuned mass absorbers.

2.5 Concept - Base Isolation Using a Grounded Spring-Mass Chain

Alternatively, instead of adding resonators to the mass of the generator, it may be desirable to modify the generator support to act as a mechanical filter. Using the FEA model of the unmodified generator geometry, shown in Fig. 2.3, as a base, and for comparison, a modification to the support is made to reduce vibration transmitted by the base to the ground. It is easier to develop concepts for the support on the mass-on-a-spring model (Fig. 2.6) instead of the rotational model, since it involves only a single spring. Then the concepts can be scaled up to the full FE model.

Previous research [36] has explored the possibility of adding mass in the chain of support, as shown in Fig. 2.10. This research found that adding masses along the main chain increased the slope of the frequency response after the natural frequencies in the attenuation zone, providing more attenuation faster, but at the expense of adding new resonances,

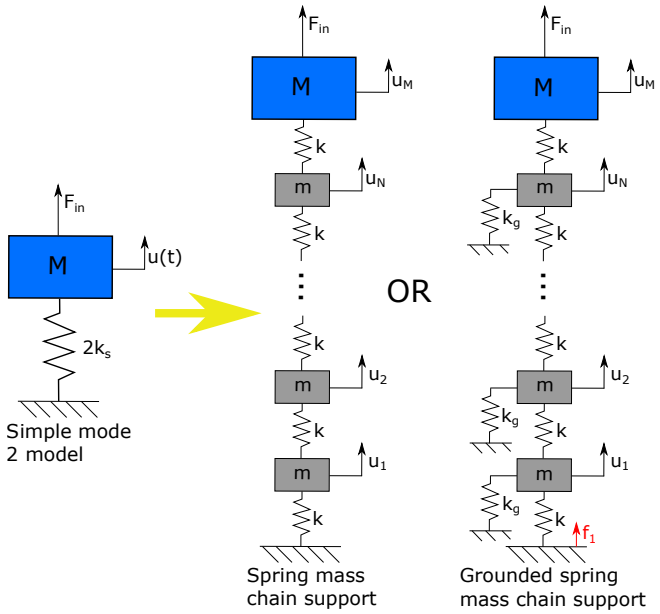

Figure 2.10: Support modified to include a spring mass chain.

which pushed the cut-off frequency of the system higher. For a high-mass, high-stiffness system with a low excitation frequency such as the power generator, this is not a feasible solution because the additional masses push the cut-off frequency above the excitation frequency. If this solution is modified slightly to include grounding springs on the masses, a grounded spring mass chain results, which is known to produce a high pass mechanical filter [33]. This concept is examined in greater detail here. Before integrating any concepts into the simple mass-on-a-spring model the dispersion diagram of the grounded spring mass chain is used as a tool to evaluate the concept's ability to provide attenuation at the excitation frequency.

2.5.1 Spring Mass Chain Dispersion

An example of several unit cells of an infinite chain is shown in Fig. 2.11. For this configuration, the equation of motion for the nth mass is

$$m\ddot{u}_n + (2k + k_g)u_n - k(u_{n-1} + u_{n+1}) = 0. \tag{2.10}$$

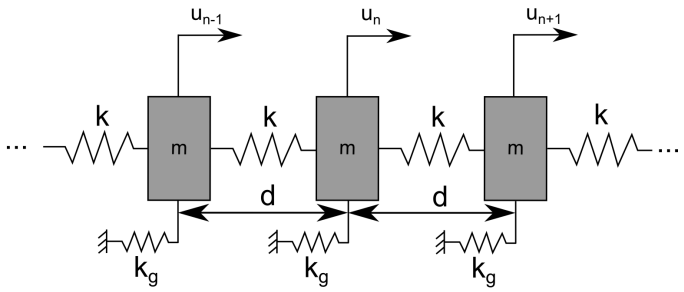

Figure 2.11: Example of a grounded spring mass chain.

To get the dispersion relationship, a plane wave solution is employed, so that $u_n = \tilde{u}(\mu(\omega))e^{i(\mu n - \omega t)}$ where $\mu = \kappa d$ is the normalized wave number, and κ is the wave number [31]. Subbing this into Eq. (2.10) leads to the dispersion relation

$$\Omega = \sqrt{2[1 - cos(\mu)] + \Omega_g^2} \tag{2.11}$$

where

$$\Omega = \quad \frac{\omega}{\omega_0} \tag{2.12}$$

$$\Omega_g = \quad \frac{\omega_g}{\omega_0} \tag{2.13}$$

$$\omega_0 = \quad \sqrt{\frac{k}{m}} \tag{2.14}$$

$$\omega_g = \quad \sqrt{\frac{k_g}{m}}. \tag{2.15}$$

Here Ω and Ω_g are the normalized excitation frequency and what is herein termed the normalized grounding frequency, respectively. The normalized grounding frequency is the resonant frequency if the mass were only connected to the grounding spring.

Using Eq. (2.11) the lower and upper bounds of the pass band for this system can be found. The minimum occurs when $cos(\mu) = 1$, and the max occurs when $cos(\mu) = -1$,

which leads to

$$\Omega_{min} = \quad \Omega_g \tag{2.16}$$

$$\Omega_{max} = \quad \sqrt{4 + \Omega_g^2}. \tag{2.17}$$

Because the grounded spring mass chain is a high pass filter it can be used to stop low frequencies from propagating through the structure. Based on the above equations, criteria can be established to tune ω_{min}, the lower end of the pass band, or the upper end of the stop band, which ranges from $0 - \omega_{min}$. If it were desirable that a target frequency ω_t fall inside the stop band, then the spring mass chain must meet the requirement that

$$\omega_{min} > \omega_t. \tag{2.18}$$

If the mass were fixed, then this criteria can be reduced to a requirement on the grounding springs, of

$$k_g > m\omega_t^2. \tag{2.19}$$

This means that the value of k_g can be tuned to place a target frequency of ω_t inside of a stop band.

As an example, the first mode natural frequency of the generator discussed in Sec. 2.4, is given by Eq. (2.3). To make this natural frequency fall within the stop band of a support modified to include grounding springs the grounding spring stiffness must satisfy the requirement

$$k_g > mR\sqrt{\frac{2k_s}{I}} \tag{2.20}$$

where m is the chosen mass in the spring mass chain. In Fig. 2.12 a nondimensionalized dispersion diagram which might result from this choice, from Eq. (2.11), is shown with $\Omega_{min} = 0.3$, chosen to safely place a target frequency of $\Omega_t = 0.04$ within the bandgap generated by the structure.

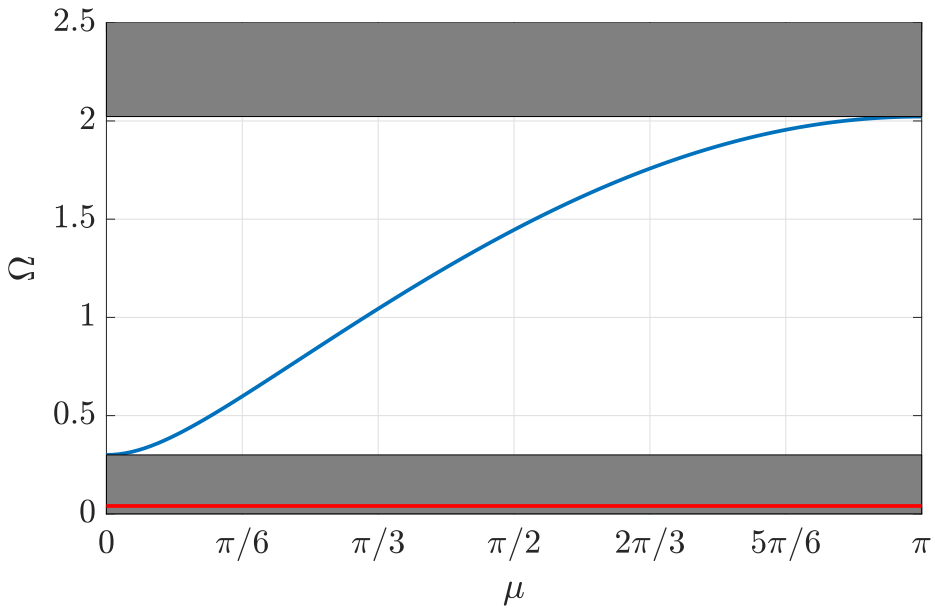

Figure 2.12: Nondimensionalized dispersion diagram for grounded spring mass chain, with stop bands shown in gray, target frequency in red, and dispersion relation in blue.

2.5.2 Simple Spring Mass Chain Support

Fig. 2.10 shows a simple lumped element model of how the grounded spring mass chain may be incorporated into the support of the structure. The input force to this model is indicated by F_{in}, a force applied to the generator mass of the system, modeling how the magnetic load would excite the generator in this manner. The transmitted force of interest is indicated by $f_1 = f_{tr}$, the reaction force along the main spring chain.

Two different responses to this system are shown, Figs. 2.13 and 2.14, with a similar Ω_{min} to that shown in the dispersion diagram, Fig. 2.12. The response is normalized by the first natural frequency of the system without the grounded masses, which is

$$\omega_{n1} = \sqrt{\frac{k_s}{M}} = \sqrt{\frac{(N+1)k}{M}}. \tag{2.21}$$

In Fig. 2.13 the ratio of individual grounded mass to generator mass is $m/M = 0.1$. This is a relatively high mass ratio. For example, if the mass of the generator were 10,000 kg, the mass of each individual mass in the chain would be 1,000 kg. Although an infeasible

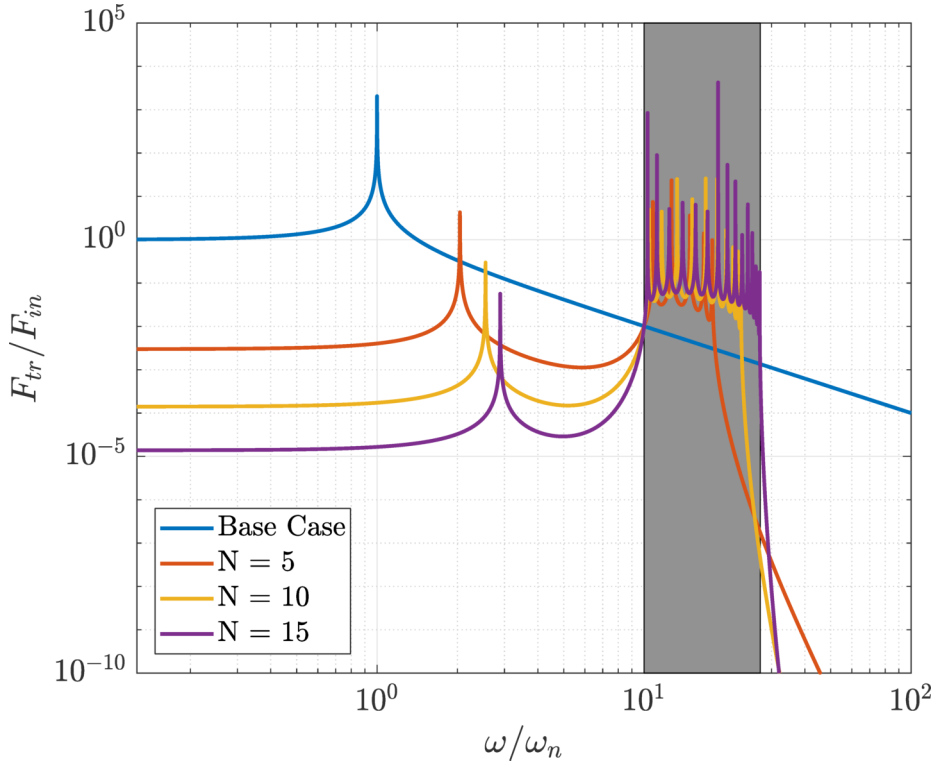

Figure 2.13: Analytical model of a grounded mass spring chain support, $m/M = 0.1$, N is the number of unit cells included in the chain.

mass, this amount was chosen to demonstrate that the desired high-pass filtering effects do in fact occur. The transmitted force through the main chain to ground is reduced by several orders of magnitude until just before Ω_{min} for the pass band.

In Fig. 2.14 the ratio of individual grounded masses to the generator mass is $m/M = 0.004$. Even at this very small value more than 65% attenuation occurs for frequencies less than Ω_{min} for the $N = 5$ case, except at the generator natural frequency, ω_{n1}. The natural frequency was shifted by the increased stiffness which resulted when the grounding springs were added.

These examples demonstrate the potential of the grounded spring-mass chain concept to reduce the response over a chosen frequency range. All of the new frequencies introduced by the spring-mass chain fall within the pass band (highlighted in gray), predicted by the dispersion diagram of the system. At frequencies lower than the pass-band attenuation occurs. These results demonstrate how designing a grounded spring mass support would

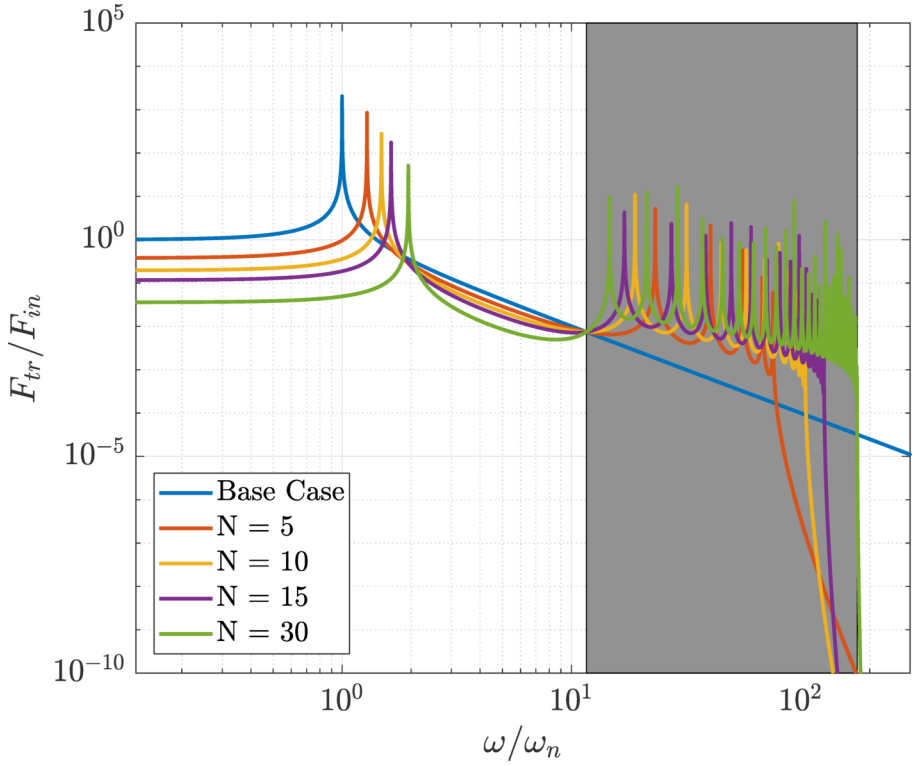

Figure 2.14: Analytical model of a grounded mass spring chain support, $m/M = 0.004$, N is the number of unit cells included in the chain.

work, as well. As the number of unit cells, N, increases, greater attenuation occurs. Also, at higher masses greater attenuation is achieved. To design a grounded spring mass support these results suggest that more unit cells, and higher masses, will result in more effective vibration mitigation. Finally, by adding the grounding springs, the overall stiffness of the system was increased. This could be an undesirable effect depending on how this affects the natural frequency of the system that falls within the band gap. This can be mitigated by modifying the spring stiffnesses along the main spring mass chain to maintain the value of this natural frequency.

These results show that the dispersion relation can be used to determine the spring stiffnesses and mass values for designing a grounded spring mass support. They also show that a grounded spring mass chain, when integrated into the support can effectively attenuate the vibration experienced by the support.

2.5.3 Implementation of a Spring Mass Chain Support on a Generator

Although these concepts have been shown to be theoretically feasible, they do not address the reality of the challenges in implementing them. In a typical tuned resonator system, there is a trade-off between the stiffness and mass of the system. To achieve attenuation at low frequencies, high mass is required, but this increases the stiffness.

In an applied setting, there is another design variable that becomes particularly relevant, and often disqualifies phononic material concepts. This variable is the available space. To effectively apply a phononic material concept enough unit cells need to be included to provide sufficient attenuation, but the available space can limit the number of unit cells. The vibrating generator problem has short supports. In order to provide sufficient attenuation each unit cell needs to be relatively compact. Therefore this problem is a good example of how space constraints might be taken into account.

Fig. 2.15 shows how the grounded spring mass chain can be implemented as a support for the generator with 5 masses. Because the support needs to stay statically stiff, each of the springs was replaced with a longitudinal bar. This is possible because a longitudinal bar acts like a spring with equivalent stiffness given in Eq. 2.1. Because the mechanical ground is a horizontal plane, for the generator, each of the grounding springs needs to become longer to reach the ground. To obtain the same static stiffness each of the grounding springs needs to have an increased thickness to compensate for the added length. This actually becomes a limiting factor with the small amount of space provided. Too many masses would result in too much space being taken up by the grounding springs. As noted earlier, the space available for grounding springs becomes a limiting factor in the number of unit cells that can be included.

Each of the springs along the main chain were also replaced with longitudinal bars, of constant length, except for the top spring, which needed to be a little longer to provide clearance from the generator for the first mass. Its thickness was adjusted accordingly. The masses were modeled as simple blocks. This is another limiting factor in the application

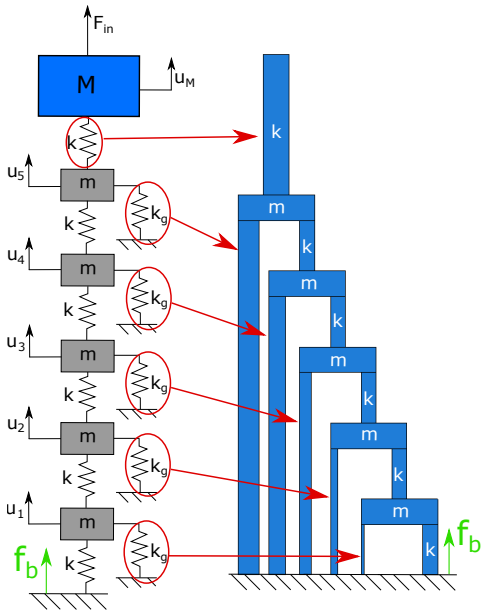

Figure 2.15: Application of the grounded spring-mass chain for the generator support.

of the grounded spring-mass chain. Because some clearance is necessary for the mass the amount of vertical available space is reduced. This reduces the number of masses that can be included.

The grounded spring mass support incorporated into the generator is shown in Fig. 2.16. The support is the same length, but is a little wider than the previous support. To verify that the behavior of this concept is as expected from the dispersion diagrams and simplified models provided previously the response of the generator with these supports was simulated.

For the simulations the generator support is subject to fixed boundary conditions at the base, to simulate ground, as indicated by the red arrows. The loading was identical to that used for the generator with the unmodified support (Fig. 2.3), and the transmitted force was measured at the right most member, indicated by the green arrow. This member is the main chain spring on the right side of the chain attached to ground. It is equivalent to the spring indicated in Fig. 2.15 by the reaction force f_b meaning the base force.

The FEA results for two variations of this support design are shown in Fig. 2.17, for the same mass ratios as given in Figs. 2.13 and 2.14. The results were normalized by

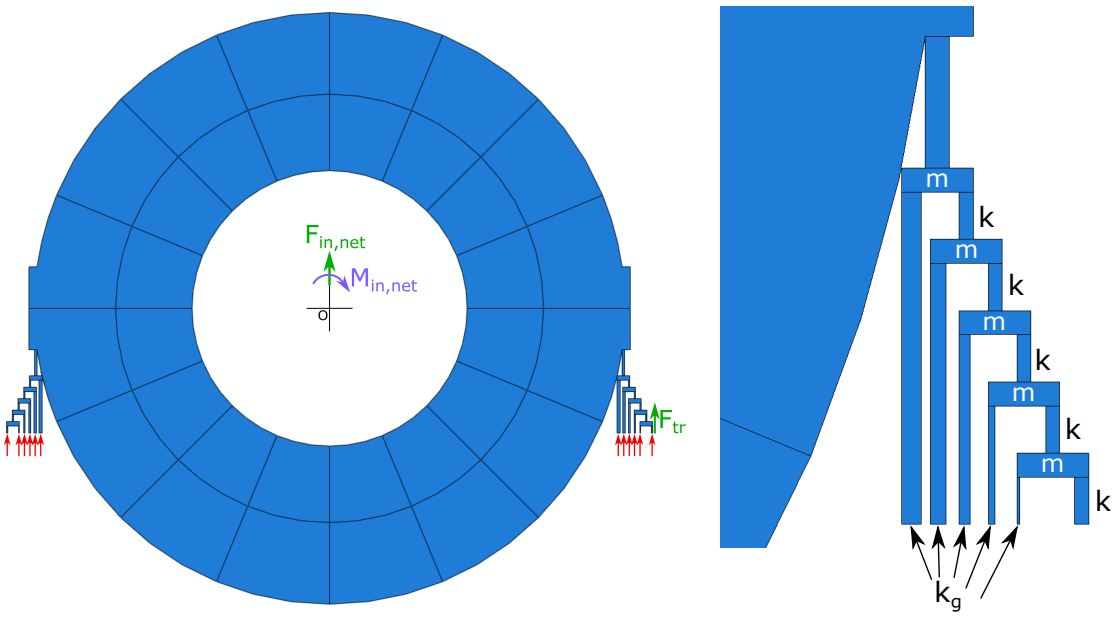

Figure 2.16: Generator finite element model with grounded spring mass support (mesh not shown), zoomed in on grounded support shown on right.

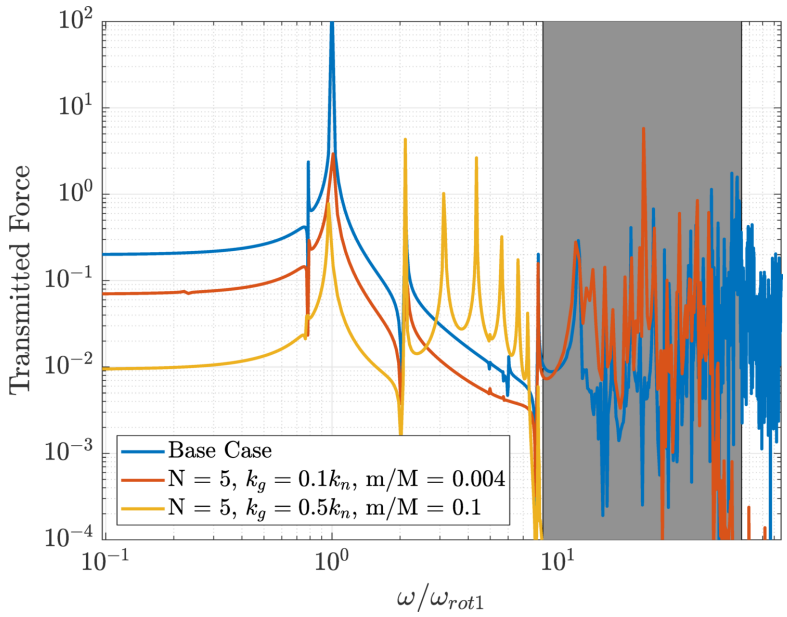

Figure 2.17: Response of the generator with grounded spring mass chain supports.

the first rotational mode of the generator system, because this was the closest resonance to the target frequency, and the response at this resonance dominated all the others. The pass band for the $m/M = 0.004$ case is indicated in gray. Any new natural frequencies introduced for this case fall inside of the pass band. Because of the large number of natural frequencies in this frequency range, the new natural frequencies of the grounded resonators are a little difficult to separate from the natural frequencies of the system. However, the rapid roll-off after the pass band matches what was predicted in the discrete mass model. For the $m/M = 0.1$ case, the newly introduced modes occur at lower frequencies due to the larger stiffness used for k_g. However, these frequencies fall within the pass band for this particular case of mass and stiffness.

At the target frequency of $\omega/\omega_{rot1} = 0.96$ there is attenuation of approximately 94% for the $m/M = 0.004$ case, and approximately 99% for the $m/M = 0.1$ case. Although the same number of masses are used, because the masses are much larger for this case, the transmitted force is reduced even further. These results show that the grounded spring-mass support can successfully attenuate vibration, acting as a high-pass filter.

2.6 Conclusion

Two concepts have been proposed as potential candidates for reducing the vibration of heavy machinery, without reducing the static stiffness necessary to support the machinery. The first concept was a simple resonator designed to reduce rotational vibration by increasing the rotational inertia. This reduction in rotational vibration resulted in attenuation of the force transferred from the generator to ground at the excitation frequency. The second concept was designed based on a phononic material concept, grounding springs, which when stiff enough are known to create a high pass filter. Adding the grounding springs changed the frequency response of the supports at the excitation frequency of interest, also resulting in a large amount of attenuation. Both of these concepts could be used for vibration mitigation of other rotating machinery as well.

CHAPTER 3

HIGH VOLTAGE VACUUM CIRCUIT BREAKER BOUNCE MITIGATION

3.1 Overview

High voltage vacuum circuit breakers have become the standard for industrial circuit breaker applications. Circuit breakers interrupt the flow of electricity through an electrical network, protecting it if the current flow becomes too high. When the electrodes in a circuit breaker close, initiating the flow of electricity, they bounce off of each other before reaching resting contact. During bouncing, arcing occurs between the electrodes, which can lead to permanent welding of the electrodes and failure of the circuit breaker. Previously the electrode bouncing problem has been studied analytically using various lumped element models or numerically using finite element models. These analyses focused on the energy dissipation or predict the bounce duration. However, wave propagation within the system and how it affected bouncing was not analyzed. In this chapter a new model of electrode bouncing, treating the electrodes as a continuous system, is developed. This model provides analytical solutions to wave propagation in the system, as well as analytical solutions to the bounce duration. These analytical solutions illuminate what parameters of the system control the bounce duration for the electrodes. Some criteria are also suggested which could help reduce circuit breaker bouncing.

3.2 Introduction

Of particular interest for this chapter is electrode arc reduction during bouncing due to electrode closure of medium and high voltage vacuum circuit breakers. Circuit breakers work like switches, which open, interrupting the flow of current, to protect the circuit and its constitutive elements if the current flow becomes too high. In high voltage vacuum

circuit breakers a fixed and a movable electrode are placed in a vacuum, which acts as a dielectric, preventing current flow. If the current flow becomes too high the electrodes separate and the vacuum prevents any further current from flowing. A diagram of a typical vacuum circuit breaker is shown in Fig. 3.1. When the circuit is closed again the following process occurs:

1. The movable electrode is given a closing velocity, usually between 1 - 2 m/s.
2. An arc forms between the electrodes as they approach each other.
3. The arc melts the surface of the electrodes, ejecting particles into the vacuum reducing its dielectric effectiveness as a barrier to current flow [40].
4. The electrodes make contact and initially bounce off of each other for a period of time. It takes approximately 1 - 2 ms for an arc to be established [40]. Usually bounces are long enough for more arcing to occur.
5. After some period of time the electrodes are welded together in resting contact, due to surface melting [41].

The welding that occurs when the circuit breaker closes is called percussive welding. If the percussive weld is too strong, then the circuit breaker will be unable to reopen, constituting a critical failure of the breaker. Previously, investigations into the optimal surface material identified materials that resulted in improved weld resistance [42]. The strength of the arc also has an effect on the failure of the circuit breaker. To reduce the effect of the arc the shape of the electrodes were given a spiral shape, causing the arc to move around the surface of the electrode, reducing the amount of localized heating at any one spot [43][44]. Another strategy to reduce the strength of the weld and maintain the life of the circuit breaker is to reduce the arc duration because it results in less melting of the electrode surfaces. This means fewer particles are ejected into the vacuum, maintaining its dielectric

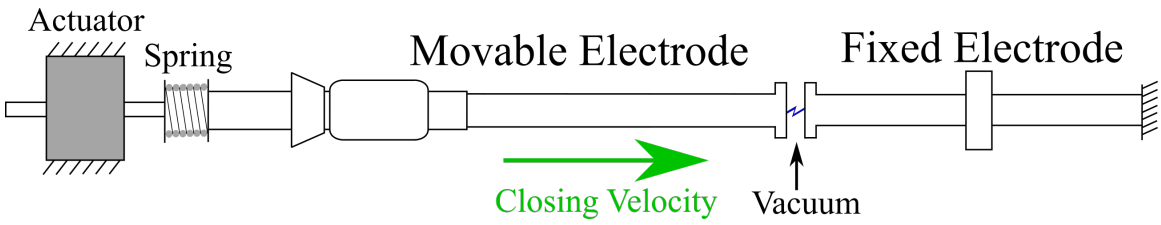

Figure 3.1: Vacuum circuit breaker mechanical diagram.

capabilities, so that arcing is less probable during bouncing. It also means a weaker resting weld, leading to less force necessary to open the breaker, and a longer breaker life.

At the time of impact stress waves are created in the electrodes, and propagate through them. As the waves propagate they will reflect off of boundaries. Although the stress waves are initially compression waves due to the impact, after reflections off of the boundaries the waves can return to the electrode interface in tension [45]. When the contact interface between the two electrodes reaches a state of tension, then bouncing initiates and contact is lost. Springs at the base of the electrodes push the electrodes together again, resulting in multiple bounces, and ultimately resting contact. Electrode bounce duration is dependent on the complex interaction of a number of factors, which will be demonstrated and explored further in this chapter. These factors include the wave speeds in the electrodes, the electrode lengths, and stiffness of the springs the electrodes are mounted on, as well as mechanical energy dissipation from the impact [46].

Effort has already been put into reducing the amount of heating the electrodes experience by modifying their contact and bounce characteristics. In [47] a spring was added to the base of the fixed electrode, as well as a bellows, to minimize the contact bouncing. The dissipation of kinetic energy during contact was studied in [46]. Contact after impact can only be maintained if at least some of the kinetic energy from impact is dissipated. The main method of energy dissipation for electrode contacts was found to be plastic deformation of the electrode surfaces, along with some slip and friction. Multiple open and close cycles result in repetitive reworking and work hardening of the electrode surfaces leading to the possibility that the electrode contact surfaces could fail in fatigue. Impact energy

is also dissipated through the support structure of the electrodes. If the amount of impact energy transferred to the support structure is maximized then electrode bouncing can be reduced. Reference [48] later confirmed experimentally and with FE models that the impact force from closing electrodes resulted in stresses beyond the yield stress of the contact materials. The closing speed was also optimized to minimize total arc duration, which is a combination of closing duration and bounce duration [49].

Previous research examining the bouncing portion of the electrode arc problem has mainly focused on either experimental investigation of the circuit breakers, or else simulated the impact and bounce using finite element or lumped element models. None of these models were used to look at the role wave propagation played in bouncing. Treating the electrodes as a continuous system would allow for greater fundamental insight, from a wave propagation perspective, into what dynamics play a role in the initiation of bounce, and what factors control the bounce duration. Because arcing can't be avoided during closing, and it is difficult to eliminate bouncing completely, this research seeks to provide information which will help to modify the wave propagation phenomenon, and therefore the bouncing, so that arcing doesn't occur during electrode bouncing.

3.2.1 Bounce Requirements

In Fig. 3.2 a time record of bounce and contact for two electrodes is shown. A low value indicates bounce, while a high value indicates contact. The data has been nondimensionalized assuming that the electrodes are made out of copper with a wave speed c_{copper} and a length L of 1m. Using these assumed values time was nondimensionalized with $t_{nondim} = tc_{copper}/L$. Material properties used for copper can be found in Table 3.1. This data was obtained from experiments conducted by the research sponsor.

From the data in Fig. 3.2 some bounce criteria can be developed. The average bounce duration for the data is 7.48 nondimensional time units. Using the same nondimensionalization, it takes 3.5 - 7 nondimensional time units for an arc to set up (assuming 1 - 2 ms).

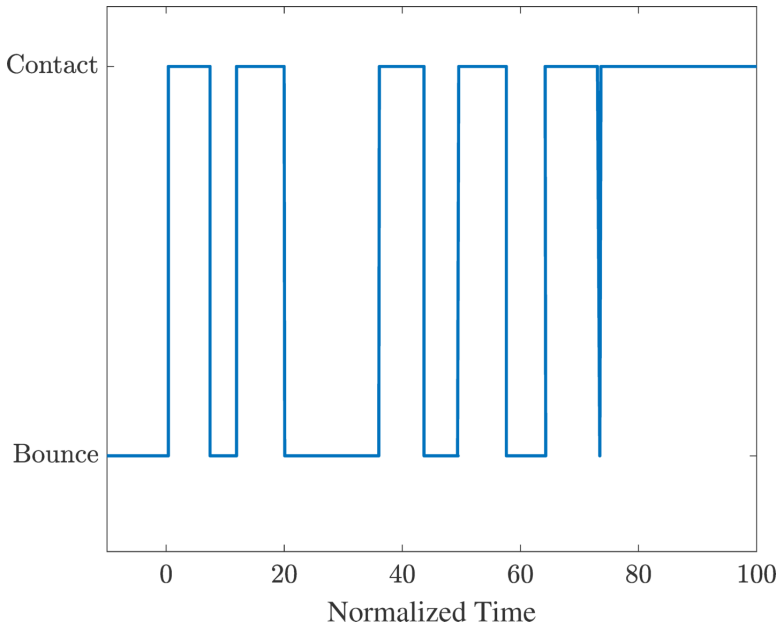

Figure 3.2: Sample experimental data of bouncing circuit breakers electrodes with contact indicated by a high value and bounce indicated by a low value.

Young's Modulus (E)	110 GPa
Density (ρ)	$8930\text{kg}/\text{m}^3$
Wave Speed ($c = \sqrt{E/\rho}$)	$3510\text{m}/\text{s}$

Table 3.1: Material properties used for assumed copper electrode.

Desired Arc Duration Reduction (%)	25	50	100
Necessary Bounce Duration Reduction (%)	13.3	26.5	53

Table 3.2: Reduction in bounce duratio necessary to achieve a desired reduction in arc duration.

If the average bounce duration could be reduced to less than 3.5 then arcing would be eliminated. The percent reduction in bounce duration required to prevent arcing is calculated to be

$$\frac{7.48 - 3.5}{7.48} * 100\% = 53\% \tag{3.1}$$

This means that reducing the average bounce duration from 7.48 to 3.5 nondimensionalized time units, which is a 53% reduction, would result in a 100% reduction in arc duration. Table 3.2 includes data for the necessary reduction in bounce duration for a couple other cases. This simple analysis shows that bouncing does not need to be eliminated to prevent arcing. If instead the bouncing can be reduced to sufficiently short bounces then arcing will be eliminated, improving the performance of the circuit breaker.

3.3 Basic Circuit Breaker Bouncing Model

In this work the electrodes in the circuit breaker are modeled as continuous rods. This simplification of the actual electrodes naturally lends to the derivation of analytical expressions for bounce duration, something which previous analyses did not provide. The continuous electrode model is shown in Fig. 3.3. Each electrode is modeled as a rod undergoing longitudinal vibration. The key parameters modeled include: the lengths of the rods L_1 and L_2; the rod densities ρ_1 and ρ_2; the rod Young's moduli E_1 and E_2; the rod cross sectional areas A_1 and A_2; the initial closing velocity v_i; the base displacement for the movable spring, u_b; and the spring stiffness k. The base displacement and movable spring model the actuator which pushes the two electrodes together.

These important values allow the problem to be nondimensionalized. Using the pa-

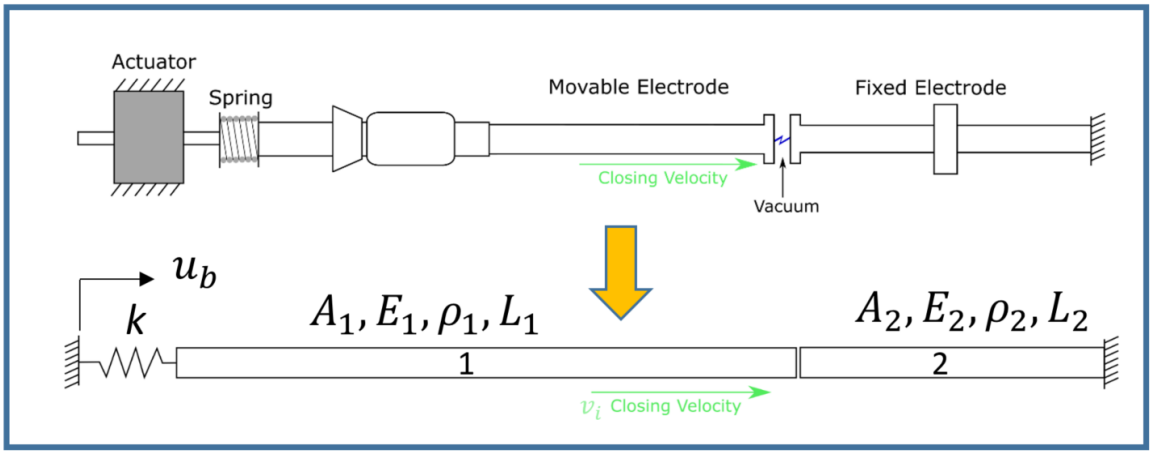

Figure 3.3: Simplified electrode impact model.

$\hat{\rho}_2 = \frac{\rho_2 L_1^2}{\rho_1 A_1}$	$\hat{A}_1 = \frac{A_1}{L_1^2}$	$\hat{A}_2 = \hat{A}_1 \frac{\rho_1 c_1}{\rho_2 c_2}$	$\hat{v}_i = \frac{v_i}{c_1}$
$\mathbf{\hat{L}_2 = \frac{L_2}{L_1}}$	$\mathbf{\hat{c}_2 = \frac{c_2}{c_1} = \sqrt{\frac{E_2 \rho_1}{E_1 \rho_2}}}$	$\mathbf{\hat{u}_b = \frac{u_b}{L_1}}$	$\mathbf{\hat{k} = \frac{k L_1}{E_1 A_1}}$

Table 3.3: Nondimensional parameters governing the electrode bouncing problem.

rameters $t^* = L_1/c_1$, $m^* = \rho_1 A_1 L_1$, and $L^* = L_1$ the nondimensional parameters given in Table 3.3 were derived. c_1 and c_2 are the wave speeds in the movable and fixed rods, respectively. These are calculated through the relationship $c = \sqrt{E/\rho}$. The parameters of greatest importance to the bouncing problem are bolded on the second row of Table 3.3. This research looks at how varying three of these parameters, $\hat{L}_2$, $\hat{c}_2$, and $\hat{k}$ affect the bounce duration. The fourth parameter, $\hat{u}_b$ controls the compression of the base spring. In the model, if the base spring is not compressed, then as the rods displace forwards after impact the spring will pull the movable rod away from the fixed rod. But this is not what the actuator in the actual circuit breaker would do, it would continue to provide a closing force. By applying a base displacement to the spring equal to or greater then the maximum displacement in the rod the spring can be kept in compression, always pushing the rods together, as actually occurs in the circuit breaker.

In the circuit breaker, each electrode is made of the same material. The model included here allows the material of the two electrodes to vary. Because of this the effect of changing the wave speed on the bounce duration can be studied. It is hypothesized that a change in

wave speed could lead to a desirable reduction in bounce duration. Only the first bounce and the parameters that affect it are examined in this analysis. Although the bounces before permanent contact are not identical, it is assumed that the first bounce will provide enough insight into the waves and physical processes that affect electrode bouncing to significantly modify the electrode bounce characteristics. In practice, changing electrode wave speeds is not realizable through changing the materials of the electrodes because of other design considerations (such as conductivity) that factor into the choice of materials. However, dispersion could be introduced using phononic materials to create an effective change in wave speed at different frequencies.

One important assumption has to do with a constraint placed on the reflection coefficient. Typically, when a wave hits an interface between two different materials, or a change in cross sectional area, part of the wave is transmitted and part of the wave is reflected. If the rods were identical, then the reflection coefficient would be zero, and the transmission coefficient would be 1. The wave would be transmitted perfectly. Including two different materials would result in a new reflection, introduced at the interface boundary, each time a wave reaches it. Because in actuality the electrodes are made of the same material, this wave is undesirable, and unnecessarily complicates the model. To eliminate this wave, the reflection coefficient must be zero. The reflection coefficient is given as

$$c_r = \frac{\hat{A}_2\hat{\rho}_2\hat{c}_2 - \hat{A}_1\hat{\rho}_1\hat{c}_1}{\hat{A}_1\hat{\rho}_1\hat{c}_1 + \hat{A}_2\hat{\rho}_2\hat{c}_2}. \tag{3.2}$$

Requiring the reflection coefficient to be zero means that the numerator of Eq. 3.2 must be zero. The densities and wave speeds are independent variables to be investigated, so the no reflection requirement puts a constraint on the cross sectional area. To prevent reflection at the contact interface the following relationship must be satisfied

$$\hat{A}_2 = \hat{A}_1\frac{\hat{\rho}_1\hat{c}_1}{\hat{\rho}_2\hat{c}_2}. \tag{3.3}$$

This requirement simplifies the analysis, by preventing reflections which wouldn't otherwise be in the system, but does change the amplitude of the transmitted wave. However, the general trends and conclusions derived from the analysis are still valid.

3.3.1 Equations of Motion

The system is modeled as two separate rods, given by the equations

$$\frac{\partial^2 u_1}{\partial \hat{x}^2} = \frac{\partial^2 u_1}{\partial \hat{t}^2} \tag{3.4}$$

$$\frac{\partial^2 u_2}{\partial \hat{x}^2} = \frac{1}{\hat{c}_2^2}\frac{\partial^2 u_2}{\partial \hat{t}^2} \tag{3.5}$$

where $u_1(\hat{x}, \hat{t})$ is the nondimensional displacement in the movable rod, and $u_2(\hat{x}, \hat{t})$ is the nondimensional displacement in the fixed rod. $\hat{x}$ and $\hat{t}$ are the nondimensional displacement and time, defined as $\hat{x} = x/L_1$ and $\hat{t} = tc_1/L1$. For all further references the $\hat{}$ on $\hat{x}$ and $\hat{t}$ is omitted for simplicity, and they are referred to as x and t. The initial conditions to the problem are

$$u_1(x, 0) = 0 \tag{3.6}$$

$$\frac{\partial u_1}{\partial t} = \hat{v}_i \tag{3.7}$$

$$u_2(x, 0) = 0 \tag{3.8}$$

$$\frac{\partial u_2}{\partial t} = 0. \tag{3.9}$$

The boundary conditions at the spring and fixed end are given by

$$\hat{k}\left[u_1(0, t) - \hat{u}_b(0, t)\right] = \frac{\partial u_1}{\partial x}(0, t) \tag{3.10}$$

$$u_2(\hat{L}_2, t) = 0. \tag{3.11}$$

The boundary conditions at the contact interface change depending on whether or not the electrodes are in or out of contact. When they are in contact continuity requires that the force and the velocity match. Mathematically this is stated as

$$\frac{\partial u_1}{\partial t}(\hat{L}_1, t) = \frac{\partial u_2}{\partial t}(0, t) \tag{3.12}$$

$$\frac{\partial u_1}{\partial x}(\hat{L}_1, t) = \hat{E}_2 \hat{A}_2 \frac{\partial u_2}{\partial x}(0, t). \tag{3.13}$$

When the electrodes are out of contact the force and velocity no longer match. However, the physics requires that the stress at the free ends goes to zero. This leads to the out of contact boundary condition for the electrode contacting ends, of

$$\frac{\partial u_1}{\partial x}(\hat{L}_1, t) = \frac{\partial u_2}{\partial x}(0, t) = 0. \tag{3.14}$$

3.3.2 D'Alembert's Solution

From a wave propagation perspective, the best way to solve these equations is using D'Alembert's solution, sometimes referred to as the method of characteristics. This solution shows the motion of the underlying waves in the system, which results in the observed displacement, stress, and velocity. D'Alembert's solution is typically used for waves propagating in infinite rods, but can be modified to include reflections for finite rods. The solution assumes that two waves, a right traveling wave $f(x - ct)$ and a left traveling wave $g(x + ct)$. For this problem, two simultaneous solutions, one for each rod, occur. These are, in nondimensionalized form

$$u_1(x, t) = f_1(x - t) + g_1(x + t) \tag{3.15}$$

$$u_2(x, t) = f_2(x - \hat{c}_2 t) + g_2(x + \hat{c}_2 t). \tag{3.16}$$

Each reflection off of a boundary can be thought of as a wave propagating from infinity and reaching the boundary at the same time as the wave being reflected. This is called an image in the literature. The total solution is the sum of the waves and all their reflections, given by

$$u_1(x,t) = \sum_{n=0}^{\infty} f_{1n}(x-t) + g_{1n}(x+t). \tag{3.17}$$

The stress and velocity can also be calculated, and are defined as

$$\sigma_1(x,t) = \hat{E}_1 \sum_{n=0}^{\infty} f'_{1n}(x-t) + g'_{1n}(x+t) \tag{3.18}$$

$$v_1(x,t) = \hat{c}_1 \sum_{n=0}^{\infty} -f'_{1n}(x-t) + g'_{1n}(x+t) \tag{3.19}$$

and likewise for u_2, σ_2, and v_2. More information about D'Alembert's solution and the method of characteristics can be found in many textbooks on partial differential equations, or wave propagation in solids, such as [45]. One of the simplest ways to portray the wave propagation is by use of characteristic diagrams, which show the waves and their reflections.

3.3.3 Calculating Reflections From Boundary Conditions

The reflections off of fixed and free boundaries are very simple to solve for. For a fixed end a force balance requires that the wave reflect off with the same amplitude and sign, resulting in stress doubling when the wave hits a fixed end. At a fixed end velocity and displacement must go to zero. For a free end a force balance requires the forces to go to zero, resulting in a stress wave with the same amplitude, but opposite sign being reflected. For both velocity and displacement there is no restriction at a free end, resulting in velocity or displacement doubling. Greater detail on boundary conditions can be found in [45].

The most difficult boundary condition to solve for in this problem is the spring end. To solve for this end, following the process explained in [45] use Eq. 3.15 in Eq. 3.11 with

$x = 0$. This gives

$$\hat{k}f(t) + f'(t) = g'(t) - \hat{k}g(t) + \hat{k}\hat{u}_b. \tag{3.20}$$

Because the incoming wave g(x + t) is known this is a first order differential equation of $f(x - t)$. The Laplace transform provides a straightforward way to solve this differential equation. Taking the Laplace transform of Eq. 3.20 yields

$$F(s) = \left(1 - \frac{2\hat{k}}{s + \hat{k}}\right) G(s) + \frac{\hat{k}\hat{u}_b}{s(s + \hat{k})}. \tag{3.21}$$

The inverse Laplace transform can then be taken to yield an equation for the reflection f(t). This gives

$$f(t) = g(t) + \hat{u}_b(1 - e^{-\hat{k}t}) - \mathcal{L}^{-1}\left\{\frac{2\hat{k}}{s + \hat{k}} G(s)\right\} \tag{3.22}$$

which can then be used to calculate the reflection of an arbitrary waveform $g(x + t)$ off of a compressed spring boundary. To get the final solution, sum everything together, then replace t with $x + t$.

3.3.4 Finite Difference Solution

To provide comparison and validation to the analytical solutions, the equations were also solved numerically using finite difference derivatives. Equations 3.4 and 3.5 are the classic example of a hyperbolic partial differential equation. To solve partial differential equations with finite difference derivatives, solutions typically fall into the implicit or explicit category. For this problem, because we are interested in looking at relatively short time scales for the propagation of a wave in the structure, the explicit technique is the natural choice [50]. The derivatives in the wave equation are approximated with central difference

derivatives to get

$$\frac{\partial^2 u}{\partial x^2} \approx \frac{u_{i+1}^n - 2u_i^n + u_{i-1}^n}{\Delta x^2} \tag{3.23}$$

$$\frac{\partial^2 u}{\partial t^2} \approx \frac{u_i^{n+1} - 2u_i^n + u_i^{n-1}}{\Delta t^2} \tag{3.24}$$

where the index i corresponds to a discrete step in space, and n a discrete step in time. By subbing these equations into Eq. 3.4 and then solving for u_i^{n+1} an expression for each node, at each time step, is found to be

$$u_i^{n+1} = 2u_i^n - u_i^{n-1} + \left(\frac{\Delta t}{\Delta x}\right)^2 \left(u_{i+1}^n - u_i^n + u_{i-1}^n\right). \tag{3.25}$$

For the initial conditions, $n = 0$ and $u_i^0 = u(x_i, 0)$. Because of the way that the time derivative is taken, one of the terms will end up with a negative index. This negative index can be solved for by taking a first finite difference derivative in time to get

$$\frac{\partial u}{\partial t} \approx v_i^n = \frac{u_i^{n+1} - u_i^{n-1}}{2\Delta t}. \tag{3.26}$$

This provides the first time step equation, which uses the initial velocity v_i^0, to get

$$u_i^1 = u_i^0 + v_i^0 + \frac{1}{2}\left(\frac{\Delta t}{\Delta x}\right)^2 \left(u_{i+1}^0 - u_i^0 + u_{i-1}^0\right). \tag{3.27}$$

Because of the boundaries, indices that extend outside of the actual length of the rod are also included. These indices refer to ghost nodes, which can be solved for in terms of other nodes within the rod, by looking at the force balance on the boundaries. For a free boundary stress goes to zero, so

$$\frac{\partial u}{\partial x} \approx \frac{u_{I+1}^n - u_{I-1}^n}{2\Delta x} \Rightarrow u_{I+1}^n = u_{I-1}^n \tag{3.28}$$

where I represents the boundary node index. A fixed boundary is very simple to deal with.

Its displacement must be zero, so $u_I^n = 0$. The spring boundary condition also requires a force balance. The requirement that

$$\hat{k}u(0,t) = \frac{\partial u}{\partial x}(0,t) \tag{3.29}$$

becomes

$$\hat{k}u_0^n = \frac{u_1^n - u_{-1}^n}{2\Delta x} \tag{3.30}$$

which can be solved for the ghost node to get

$$u_{-1}^n = u_1^n - 2\hat{k}\Delta x u_0^n \tag{3.31}$$

For the two rod bounce model two continuity boundary conditions are also required. As stated previously, at the contact interface the velocities must be equal and forces must balance during contact. This leads to a system of equations to solve for the ghost nodes at each end. For the velocity to be equal,

$$v_i^n = \frac{u_I^{n+1} - u_I^{n-1}}{2\Delta t} \tag{3.32}$$

which can be used at the two ends in contact to get the relationship that

$$u_{1_I}^{n+1} - u_{1_I}^{n-1} = u_{2_0}^{n+1} - u_{2_0}^{n-1} \tag{3.33}$$

where u_1 is the displacement in rod 1, and u_2 is the displacement in rod 2. In the model both rods use the same time step. However, the spatial step, Δx, must be different for the model to work. Setting the forces equal at the surface of contact gives that

$$\frac{\partial u_1}{\partial x}(\hat{L}_1, t) = \hat{c}_2 \frac{\partial u_2}{\partial x}(0,t) \tag{3.34}$$

which is approximated using finite difference derivatives, as

$$\frac{u^n_{1_{I+1}} - u^n_{1_{I-1}}}{2\Delta x_1} = \hat{c}_2 \frac{u^n_{2_1} - u^n_{2_{-1}}}{2\Delta x_2}. \tag{3.35}$$

Eqs. 3.33 and 3.35 can be solved simultaneously for the ghost nodes $u^n_{1_{I+1}}$ and $u^n_{2_{-1}}$ to enforce continuity across the boundary while the rods are in contact. The solutions to these equations are

$$u^n_{1_{I+1}} = \frac{2}{1 + \hat{c}_2 \frac{\Delta x_1}{\Delta x_2}} \left[u^n_{1_I} + \frac{1}{2} \left(\hat{c}_2 \frac{\Delta x_1}{\Delta x_2} - 1 \right) u^n_{1_{I-1}} + \left(\hat{c}_2 \frac{\Delta x_1}{\Delta x_2} \right)^2 (u^n_{2_1} - u^n_{2_0}) \right] \tag{3.36}$$

$$u^n_{2_{-1}} = u^n_{2_1} - \hat{c}_2 \left(\frac{\Delta x_2}{\Delta x_1} \right)^2 (u^n_{1_{I+1}} - u^n_{1_{I-1}}) \tag{3.37}$$

The explicit solution to the wave equation is only conditionally stable, depending on a nondimensional constant called the Courant number. The Courant number is typically given as

$$C = \frac{c\Delta t}{\Delta x} \tag{3.38}$$

or using the nondimensionalization used in these equations, just

$$C = \frac{\Delta t}{\Delta x}. \tag{3.39}$$

For the numerical equations to be stable and converge, the spatial and time stepping must be chosen so that the Courant number is less than 1 [45]. For the simulations shown here, the Courant number is set to 0.5. This value provided sufficient resolution and accuracy for the problem, while still allowing for a reasonable amount of computation time.

3.3.5 Calculating Bounce Duration

To calculate the solutions, the propagating waves and their reflections must be tracked. A bounce initiates when the contact interface goes into a state of tension. Once a tension

wave reaches the interface there is nothing holding the two surfaces together, and they separate. To simulate the bounce the contacting ends then become free ends, and the waves are tracked, and reflected in the individual rods. The bounce ends when the displacements of the tips of the rods are equal again. The bounce duration is given by

$$t_b = t_{b_f} - t_{b_i} \tag{3.40}$$

where t_{b_f} is the final bounce time, when the rod displacement matches again, and t_{b_i} is the initial bounce time, when the stress reaches a value of zero, just prior to going into tension. Watching how this value changes provides insight into how the main variables affect the length of the bounce.

3.4 Circuit Breaker Bouncing Results

3.4.1 $\hat{k} \to \infty$

Analytically $\hat{k} = \infty$ models the impact and subsequent bouncing of two fixed base rods. Although this case does not occur in practice, it provides useful insight as a limiting case to show how the rods bounce off of each other. Solving for this case and tracking the wave propagation gives the wave shapes at bounce initiation (t_{b_i}) in the movable rod as

$$f_{b_{10}}(x-t) = \begin{cases} \frac{1}{2}\hat{v}_i(x-t) - \frac{1}{2}\hat{v}_i & \text{if } 0 \le x-t < \hat{L}_1 \\ -\frac{1}{2}\hat{v}_i & \text{if } -\hat{L}_1 \le x-t < 0 \\ -\frac{1}{2}\hat{v}_i(x-t) - \hat{v}_i & \text{if } -2\hat{L}_1 \le x-t < -\hat{L}_1 \end{cases} \tag{3.41}$$

$$g_{b_{10}}(x+t) = \begin{cases} \frac{1}{2}\hat{v}_i & \text{if } 0 \le x+t \le \hat{L}_1 \\ -\frac{1}{2}\hat{v}_i(x+t) + \hat{v}_i & \text{if } \hat{L}_1 < x+t \le 2\hat{L}_1 \end{cases} \tag{3.42}$$

Some reflections are included in the wave definitions, for convenience, when the waves and reflections formed a single wave packet. The wave shapes at bounce initiation in the fixed

rod are

$$f_{b_{20}}(x-\hat{c}_2 t)=\begin{cases}-\frac{1}{2\hat{c}_2}\hat{v}_i(x-\hat{c}_2 t) & \text{if } 0\le x-\hat{c}_2 t\le \hat{c}_2\hat{L}_1\\ -\frac{1}{2}\hat{v}_i & \text{if } \hat{c}_2\hat{L}_1< x-\hat{c}_2 t\le \hat{c}_2\hat{L}_1+2\hat{L}_2\end{cases} \tag{3.43}$$

$$g_{b_{20}}(x+\hat{c}_2 t)=\begin{cases}\frac{1}{2\hat{c}_2}\hat{v}_i\hat{L}_1 & \text{if } 2\hat{c}_2\hat{L}_1\le x+\hat{c}_2 t\le \hat{c}_2\hat{L}_1+2\hat{L}_2\\ -\frac{1}{2\hat{c}_2}\hat{v}_i(x+\hat{c}_2 t)+\hat{L}_1\hat{v}_i+\frac{\hat{v}_i}{\hat{c}_2}\hat{L}_2 & \text{if } \hat{c}_2\hat{L}_1+2\hat{L}_2< x+\hat{c}_2 t\le 2\hat{c}_2\hat{L}_1+2\hat{L}_2\end{cases} \tag{3.44}$$

To demonstrate the results produced by the models described, consider a bouncing rod problem with $\hat{k}\to\infty$ and $\hat{u}_b=0$, with $\hat{L}_2=0.5$ and $\hat{c}_2=0.56$ using Eqs. 3.41 - 3.44. These parameters result in the characteristic diagram for displacement, shown in Fig. 3.4. The displacement for both movable and fixed rods are shown together, as labeled. The bounce initiates at a value of $t=1$, and ends at $t=2.79$. The characteristic diagram using the finite difference derivatives is shown in Fig. 3.5 confirms the analytical solutions are correct, matching very closely.

Using these equations the waves, and their derivatives, can be tracked to determine when the contact interface is about to go into tension, indicating bounce initiation, and when the tip displacements are about to match again, indicating contact. Analytically this is a tedious and time consuming process because there are many little details to follow to calculate the bounce duration correctly. Numerically it is also difficult, for different reasons. The bouncing of the electrodes is a nonlinear process, and as a result sometimes the numerical solver used has difficulty solving after contact. To improve the finite difference solution accuracy, WENO methods could be used, which are able to model oscillatory motion and discontinuities in hyperbolic partial differential equations with higher accuracy than the current methods [51].

Tracking the waves leads to analytical solutions for the bounce duration in the $\hat{k}\to\infty$

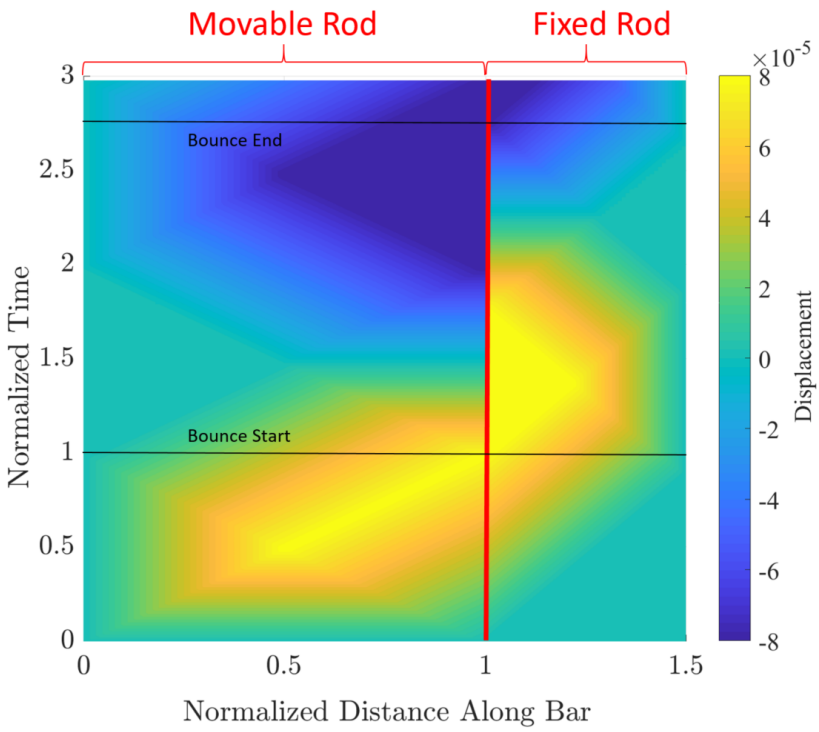

Figure 3.4: Characteristic diagram for displacement of rods for first bounce, with movable rod displacement being shown from values 0 to 1, fixed from 1 to 1.5, and parameters $\hat{k} = \infty$, $\hat{c}_2 = 0.56$, $\hat{L}_2 = 0.5$, $\hat{u}_b = 0$.

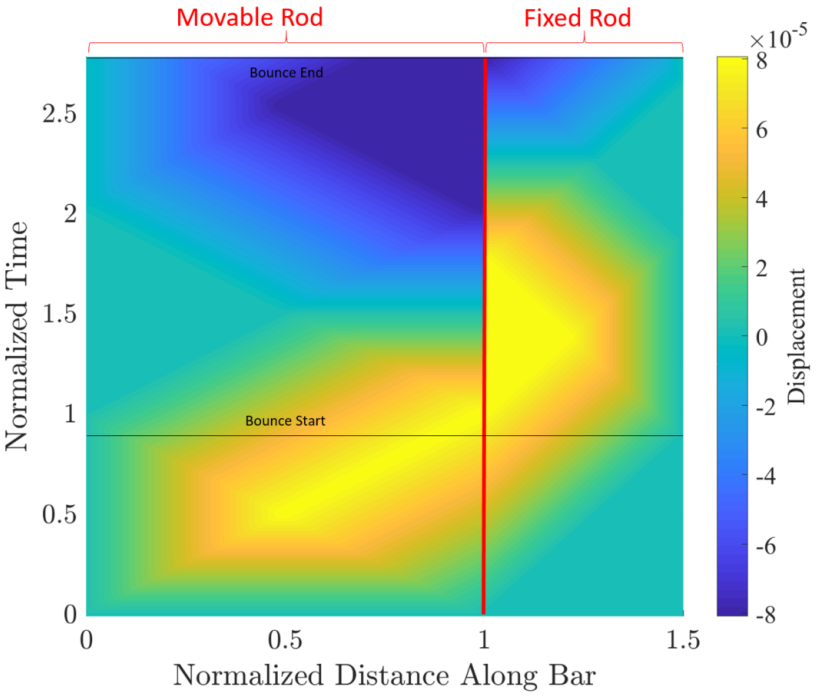

Figure 3.5: Characteristic diagram for displacement of rods for first bounce using finite difference derivatives, compare to Fig. 3.4.

case. Solutions for some values are given as

$$\hat{t}_b(\hat{c}_2, \hat{L}_2) = \begin{cases} \frac{3\hat{L}_2}{2\hat{c}_2} + \frac{3}{4} & \text{if } \frac{3}{10}\hat{c}_2 \leq \hat{L}_2 \leq \frac{1}{2}\hat{c}_2 \\ \frac{2\hat{L}_2}{\hat{c}_2} & \text{if } \frac{1}{2}\hat{c}_2 < \hat{L}_2 \leq \hat{c}_2 \\ 1 + \frac{\hat{L}_2}{\hat{c}_2} & \text{if } \hat{c}_2 < \hat{L}_2 \leq 3\hat{c}_2 \end{cases} \tag{3.45}$$

The bounce duration solutions defined in Eq. 3.45 are piecewise defined because the waves are piecewise defined. This leads to different bounce duration solutions depending on what part of the wave has reached the tips of the rods when the bounce ends and contact is reestablished. When plotted, Fig. 3.6 shows a clear trend in the bounce durations. As $\hat{c}_2$ increases, bounce duration decreases. As $\hat{L}_2$ decreases, bounce duration decreases. What this means, overall, is that bounce durations are shorter if the wave travels through the fixed rod faster. From a design perspective this suggests that if the wave speed could be increased in the fixed rod, relative to the movable, through some kind of metamaterial induced dispersion, bounces would be shortened. These conclusions, of course, are difficult to generalize to a non-infinite spring stiffness, but at least give a first glimpse of how the wave speed affects the bouncing.

Earlier, in Table 3.2, requirements were given to reduce the bounce duration to eliminate arcing. As long as bounces were less than 3.5 time units, no arcing would occur. In Fig. 3.6 the duration for all of the bounces calculated is less than this requirement. The inconsistency is due to the fact that in the actual system neither rod has a perfectly rigid base. There is some kind of spring stiffness. By tuning the spring stiffness at the base of the rod, the bounce duration could be modified to provide a reasonable range for the predicted bounce durations. This would be expected in particular for the nominal case where $\hat{c}_2 = 1$ and $\hat{L}_2 = 0.5$. Time did not allow for a thorough analysis of the spring stiffness. However, observations here suggest that the spring stiffness itself plays a very important role in bounce duration, and that stiffening the base spring on the movable electrode may

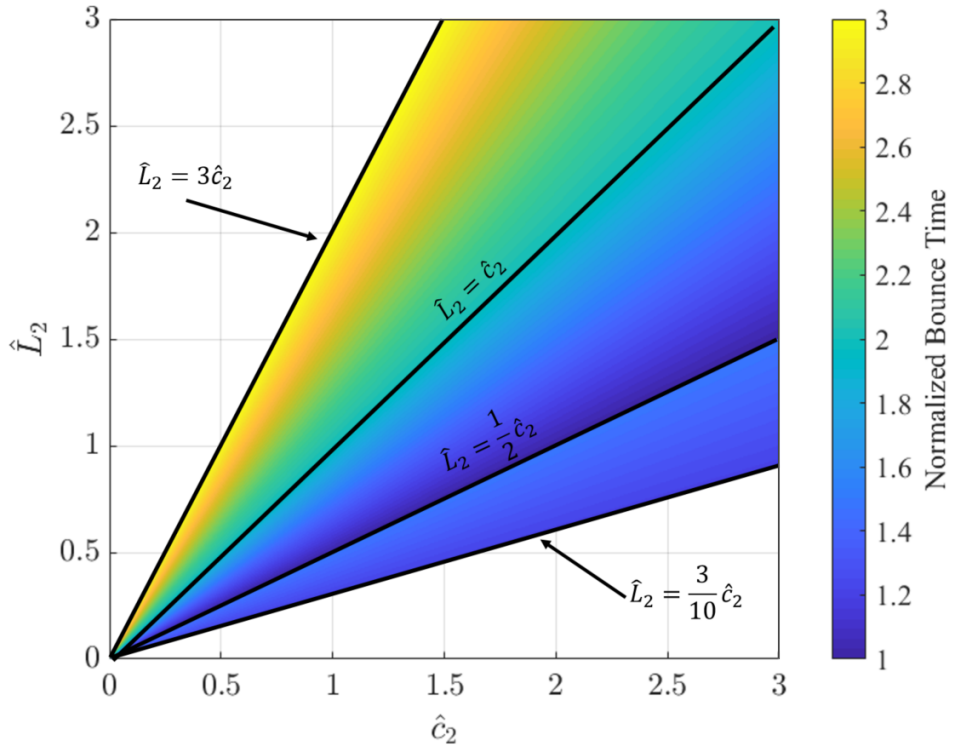

Figure 3.6: Bounce duration for first bounce of the impacting rods, with $\hat{k} = \infty$ and varying $\hat{c}_2$ and $\hat{L}_2$.

be another way to modify the bouncing to prevent arcing.

3.4.2 $\hat{k} = 2$

To provide insight into how the waves were affected by the spring, bouncing for the spring value $\hat{k} = 2$ was analyzed. For these models the spring base displacement was set to be $\hat{u}_b = \frac{1}{2}\hat{v}_i\hat{L}_1$. This value was chosen because the maximum wave displacement in the rods must be less than this. This ensures that the spring will always be compressed preventing it from pulling the movable rod away from the fixed rod. Fig. 3.7 shows the stress waves in the system, and some of the reflections, at the time of impact.

In Fig. 3.7 an example of the stress waves at impact is shown, with values of $\hat{k} = 2$, $\hat{u}_b = \frac{1}{2}\hat{v}_i\hat{L}_1$, $\hat{L}_2 = 0.5$, and $\hat{c}_2 = 0.56$. The stress waves are indicated by df and dg, which is compact notation for the derivatives of f and g, the left and right traveling waves with respect to $x - t$ and $x + t$, respectively. The waves at the time of impact in the movable

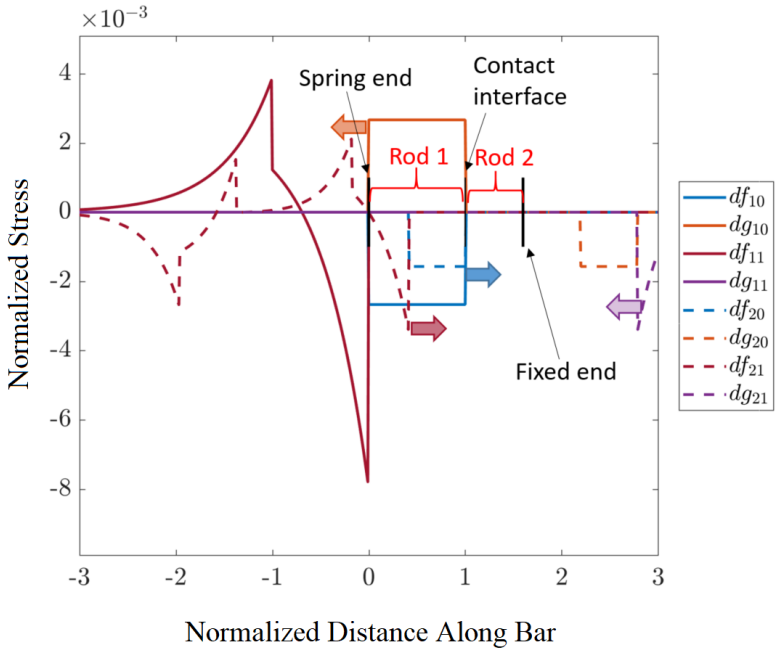

Figure 3.7: Stress waves and ghost waves, indicated as the derivatives df or dg of the traveling wave displacements f and g that will result from reflections off of the spring and fixed ends at the time of impact, in the movable (solid) and fixed (dashed) rods for $\hat{k} = 2$, $\hat{u}_b = \frac{1}{2}\hat{v}_i\hat{L}_1$, $\hat{L}_2 = 0.5$, and $\hat{c}_2 = 0.56$.

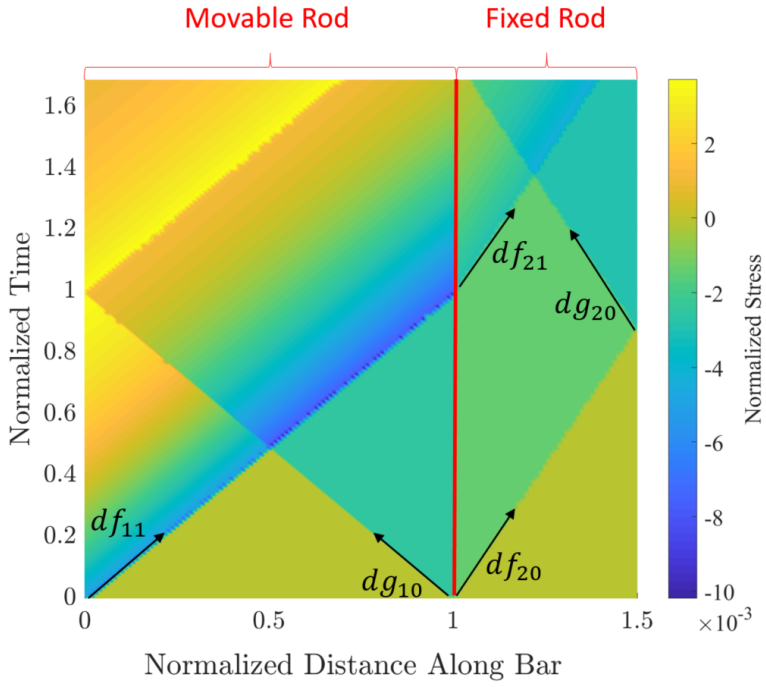

Figure 3.8: Characteristic diagram of stress waves for $\hat{k} = 2$, $\hat{u}_b = \frac{1}{2}\hat{v}_i\hat{L}_1$, $\hat{L}_2 = 0.5$, and $\hat{c}_2 = 0.56$

rod (rod 1) are square waves, shown by $df_{10}(x-t)$ and $dg_{10}(x+t)$. The rods are assumed to be in a state of zero stress at the time of impact. The wave dg_{10} is a left traveling wave. As contact initiates, it begins to reflect off of the spring boundary. The reflected wave is a right traveling wave, given by df_{11}. The fist big pulse in this wave occurs when the leading edge of dg_{10} hits the spring at impact, and the second big pulse occurs when the trailing edge of dg_{10} hits the spring. After that the response decays down to zero. df_{10} is the right traveling wave at the time of impact. At impact it starts to travel into the fixed rod. Waves traveling in the fixed rod (rod 2) are indicated by dashed lines. The wave is transmitted, but attenuated due to the requirement from Eq. 3.3. The transmitted wave is then reflected off of the fixed boundary, as dg_{20} and returns to the interface. While this is happening the other waves are being tracked to determine when the stress at the contact interface returns to zero just prior to a tension wave reaching it.

The characteristic diagram for these stress waves, from time $t = 0$ to t_{b_i}, is shown in Fig. 3.8. Some of the traveling waves are indicated by black arrows. Note that the slope of the arrows is related to the wave speed. Because the wave speed in the fixed rod was slower for this simulation, the slopes in the fixed rod are steeper. At time $t = 0$ compression waves propagate away from the contact interface, while at the same time df_{11}, which gradually goes from compression to tension, propagates towards the contact interface. Eventually, at time t = 1.68 the waves sum up to zero, and bounce initiates. Waves inside of each rod continue to propagate, but without the continuity conditions.

The bounce initiation time was found by tracking these initial waves. These times are given by the equation

$$t_{b_i} = \begin{cases} \frac{\hat{L}_1}{\hat{c}_1} + \frac{1}{\hat{k}\hat{c}_1}\ln(2+\hat{k}) & \text{if } \hat{c}_2 \leq \frac{2\hat{L}_2}{1+\frac{1}{\hat{k}}\ln(2+\hat{k})} \;\&\; \hat{k} > \ln(2+\hat{k}) \\ \frac{2\hat{L}_1}{\hat{c}_1} & \text{if } \frac{2\hat{L}_2}{1+\frac{1}{\hat{k}}\ln(2+\hat{k})} < \hat{c}_2 \leq 1 \end{cases} \tag{3.46}$$

The transcendental requirement that $\hat{k} > \ln(2+\hat{k})$ means that $\hat{k} >\sim 1.15$, all the way up to

infinity. So if the $\hat{c}_2$ requirement is satisfied, then this solution will be similar to the $\hat{k} = \infty$ case for large values of $\hat{k}$. For the case where $t_{b_i} = \frac{\hat{L}_1}{\hat{c}_1} + \frac{1}{\hat{k}\hat{c}_1}\ln(2+\hat{k})$, the wave shapes in the two rods, at bounce initiation, are

$$f_{b_{10}}(x-t) = \begin{cases} \frac{1}{2}\hat{v}_i(x-t-\hat{x}_s) + \frac{\hat{v}_i}{\hat{k}}\left(1 - \frac{1}{2+\hat{k}}e^{\hat{k}(x-t-\hat{L}_1)}\right) & \\ \qquad +\hat{u}_b\left(1 - \frac{1}{2+\hat{k}}e^{\hat{k}(x-t-\hat{L}_1)}\right) & \text{if } \hat{x}_s \le x-t \le \hat{L}_1 \\ -\frac{1}{2}\hat{v}_i\hat{L}_1 - \frac{\hat{v}_i}{\hat{k}}\frac{1}{2+\hat{k}}e^{\hat{k}(x-t-\hat{L}_1)} + \frac{\hat{v}_i}{\hat{k}}\frac{1}{2+\hat{k}}e^{\hat{k}(x-t)} & \\ \qquad +\hat{u}_b\left(1 - \frac{1}{2+\hat{k}}e^{\hat{k}(x-t-\hat{L}_1)}\right) & \text{if } -\hat{L}_1 < x-t \le \hat{x}_s \\ -\frac{\hat{v}_i}{\hat{k}}\frac{1}{2+\hat{k}}e^{\hat{k}(x-t-\hat{L}_1)} + \frac{\hat{v}_i}{\hat{k}}\frac{1}{2+\hat{k}}e^{\hat{k}(x-t)} - \hat{v}_i\hat{L}_1 e^{\hat{k}(x-t+\hat{L}_1)} & \\ \qquad +\hat{u}_b\left(1 - \frac{1}{2+\hat{k}}e^{\hat{k}(x-t-\hat{L}_1)}\right) & \text{if } x-t < -\hat{L}_1 \end{cases} \tag{3.47}$$

$$g_{b_{10}}(x-t) = \begin{cases} \frac{1}{2}\hat{v}_i\hat{L}_1 & \text{if } 0 \le x-t \le \hat{L}_1 \\ -\frac{1}{2}\hat{v}_i(x-t) + \hat{v}_i\hat{L}_i + \frac{\hat{v}_i}{\hat{k}}\frac{1}{2+\hat{k}}\left(1 - e^{-\hat{k}(x-t-\hat{L}_1)}\right) & \\ \qquad +\frac{\hat{u}_b}{2+\hat{k}}\left(1 - e^{-\hat{k}(x-t-\hat{L}_1)}\right) & \text{if } \hat{L}_1 < x-t \le 2\hat{L}_1 - \hat{x}_s \\ -\frac{\hat{v}_i}{\hat{k}}(1 - \frac{1}{2}\ln(2+\hat{k})) + \frac{\hat{v}_i}{\hat{k}}\frac{1}{2+\hat{k}}\left(1 - e^{-\hat{k}(x-t-\hat{L}_1)}\right) & \\ \qquad +\frac{\hat{v}_i}{\hat{k}}\frac{1}{2+\hat{k}}\left(1 - e^{-\hat{k}(x-t-2\hat{L}_1)}\right) & \\ \qquad +\frac{\hat{u}_b}{2+\hat{k}}\left(1 - e^{-\hat{k}(x-t-\hat{L}_1)}\right) & \text{if } 2\hat{L}_1 - \hat{x}_s < x-t \end{cases} \tag{3.48}$$

$$f_{b_{20}}(x-\hat{c}_2 t) = \begin{cases} \frac{1}{2}\frac{\hat{v}_i}{\hat{c}_2}(x-\hat{c}_2 t - \hat{c}_2\hat{x}_s) + \frac{\hat{v}_i}{\hat{k}}\left(1 - \frac{1}{2+\hat{k}}e^{\frac{\hat{k}}{\hat{c}_2}(x-\hat{c}_2 t)}\right) & \\ \qquad +\hat{u}_b\left(1 - \frac{1}{2+\hat{k}}e^{\frac{\hat{k}}{\hat{c}_2}(x-\hat{c}_2 t)}\right) & \text{if } 0 \le x-\hat{c}_2 t \le \hat{c}_2\hat{x}_s \\ -\frac{1}{2}\frac{\hat{v}_i}{\hat{c}_2}(x-\hat{c}_2 t - \hat{c}_2\hat{x}_s) & \text{if } \hat{c}_2\hat{x}_s < x-\hat{c}_2 t \le \hat{L}_2 \end{cases} \tag{3.49}$$

$$g_{b_{20}}(x-\hat{c}_2 t)=\begin{cases}\frac{1}{2}\hat{v}_i\hat{L}_1 & \text{if } 0\le x-\hat{c}_2 t\le 2\hat{L}_2-\hat{c}_2(\hat{L}_1+\hat{x}_s)\\ -\frac{1}{2}\frac{\hat{v}_i}{\hat{c}_2}(x-\hat{c}_2 t-2\hat{L}_2)-\frac{1}{2}\hat{v}_i\hat{x}_s & \text{if } 2\hat{L}_2-\hat{c}_2(\hat{L}_1+\hat{x}_s)<x-\hat{c}_2 t\le \hat{L}_2\end{cases} \tag{3.50}$$

where $\hat{x}_s = 1/\hat{k}\ln(2+\hat{k})$ is a shift resulting from the wave propagation prior to bounce.

Tracking these complex waves, and their reflections, leads to the transcendental equation for bounce duration, of

$$\hat{t}_b - c_1 e^{-k\hat{t}_b} = c_2 \qquad \text{if } m\le \hat{L}_2\le n \tag{3.51}$$

where

$$c_1 = 2\frac{1-e^{\hat{k}}+\frac{\hat{u}_b\hat{k}}{\hat{v}_i}}{\hat{k}(2+\hat{k})} \tag{3.52}$$

$$c_2 = 2\frac{\hat{L}_2}{\hat{c}_2}-\frac{2}{\hat{k}}\ln(2+\hat{k})+\frac{2}{\hat{k}}\left(1-\frac{1}{2+\hat{k})}\right)-\frac{2\hat{u}_b}{\hat{v}_i(2+\hat{k})} \tag{3.53}$$

and

$$m = \frac{1}{2}\hat{c}_2+\frac{1}{2}\frac{\hat{c}_2}{\hat{k}}\ln(2+\hat{k}) \tag{3.54}$$

$$n = \hat{c}_2-\frac{\frac{\hat{c}_2}{\hat{k}}\left(1-e^{\hat{k}}\right)+\frac{\hat{c}_2\hat{u}_b}{\hat{v}_i}}{2+\hat{k}}e^{-2\hat{k}}+\frac{\hat{c}_2}{\hat{k}}\ln(2+\hat{k})-\frac{\hat{c}_2}{\hat{k}}\left(1-\frac{1}{2+\hat{k}}\right)+\frac{\hat{c}_2\hat{u}_b}{\hat{v}_i(2+\hat{k})} \tag{3.55}$$

The solutions for the bounce duration t_b can be found from Eq. 3.51 using a numerical solver. Figure 3.9 shows Eq. 3.51 plotted as a function of $\hat{c}_2$ and $\hat{L}_2$. Due to the complexity of the equations, only one portion of the bounce duration was found. The same trends as appeared in Fig. 3.6 also appear. As $\hat{c}_2$ increases, bounce duration decreases. As $\hat{L}_2$ decreases, bounce duration decreases. An important difference also appears. The lowest

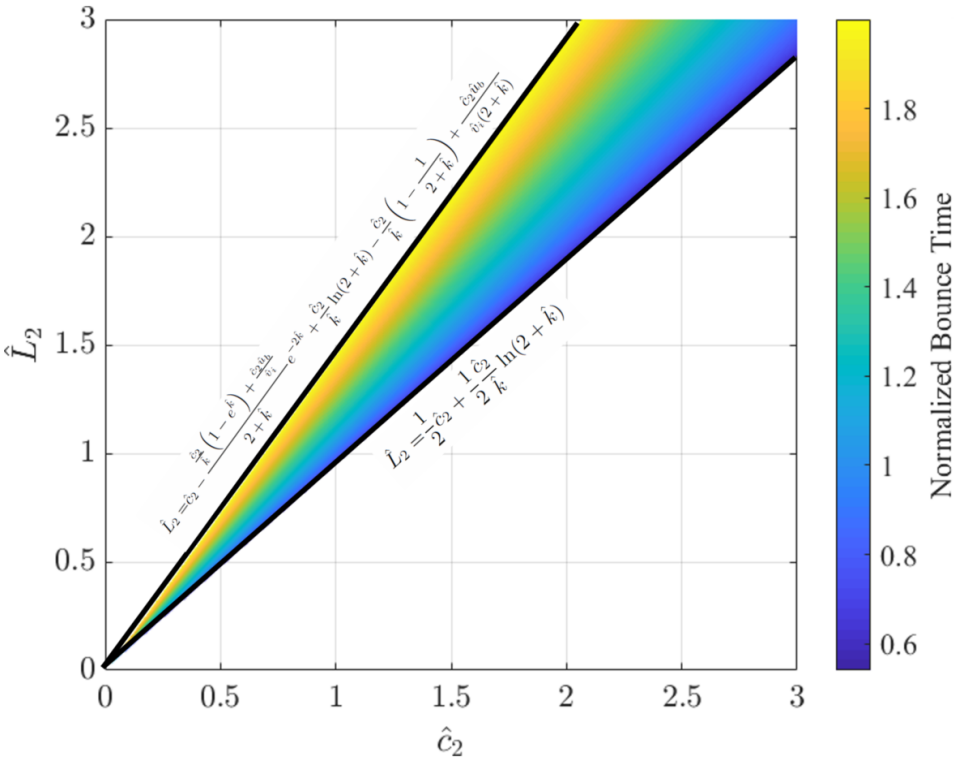

Figure 3.9: Bounce durations for $\hat{k} = 2$ and $\hat{u}_b = \frac{1}{2}\hat{v}_i$.

bounce duration is lower than the limiting value of 1 seen in Fig. 3.6 for the fixed boundary condition case. This lower bounce durattion is a result of the spring, which modifies the waves in such a way that the tips can simply skip off of each other briefly before recontacting. If this bounce goes to zero, it does not mean that all bounces are eliminated, only that the bounce will initiate from a later wave reflection.

3.4.3 Analysis of Bounce Duration Results

The results from the bounce duration have illustrated several points about the bouncing of the electrodes. Because the systems are so complex, some general observations may be more helpful than solving for specific cases. The wave functions are piecewise defined, so the bounce duration for a given combination of parameters could take a prohibitively long amount of time to solve for analytically. Only specific ranges have been solved for here. However, the solutions examined have revealed that the waves, the wave speed, and the

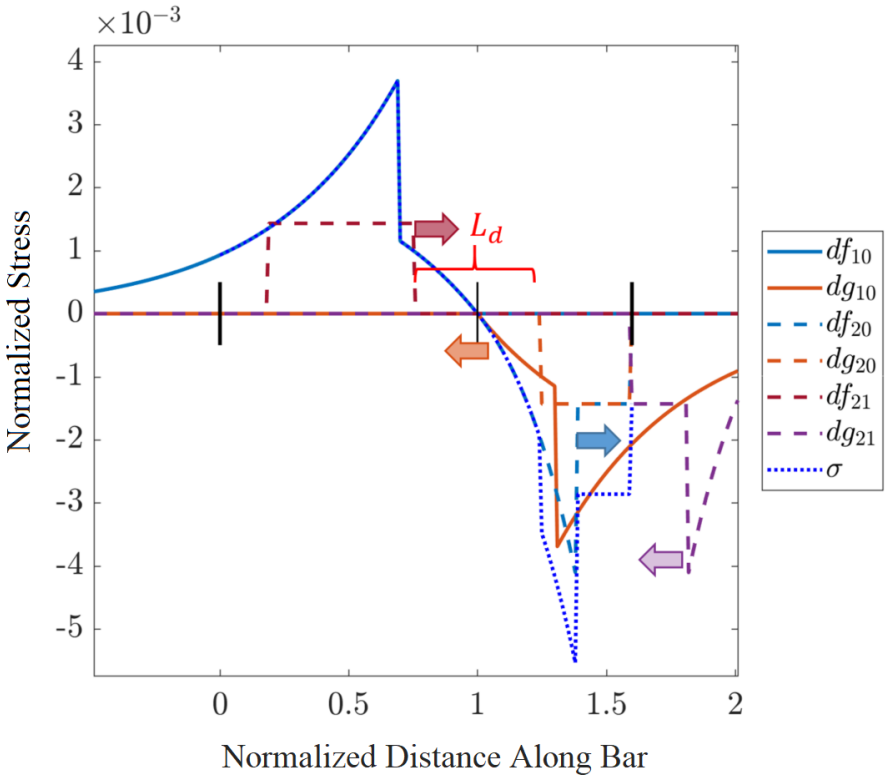

Figure 3.10: Example stress waves during bounce, indicated by df and dg, illustrating important wave characteristics that affect bounce duration.

base spring, all have an important effect on the bounce length. Physically, it should also be apparent that the stiffness of the base spring is important. In the limiting case, as the base spring stiffness goes to zero, the rods will bounce off of each other, and never recontact. By increasing the spring stiffness, multiple bounce cycles occur. As the spring gets stiffer these bounces can become very short.

3.5 Wave Characteristics for Bouncing and Dispersion

An important observation can be made from watching what characteristics of the waves have the largest effect on bounce duration. Fig. 3.10 shows an example of stress waves in the rod during a bounce, using the same compact notation for the derivatives of displacement df and dg used in Fig. 3.7 to indicate the stress waves. Two characteristics of the waves seem to have a large effect on the duration of the bounces. The first is the distance

L_d. This is the distance between dg_{20} and its approaching reflection df_{21}. This distance changes depending on the value of $\hat{c}_2$. If $\hat{c}_2$ is small, so is L_d. This distance can lead to a stall in the tip motion, where even though the waves are propagating the tips of the rods are not moving, because the waves are not interacting with the tips of the rods. The stall lasts as long as it takes the wave to reach the tip end. The result is that the tips do not move closer to each other, making the bounce last longer.

The other important characteristic of the waves is the slope. Large portions of the wave with a positive or a negative slope indicates the tips are moving in a uniform direction, either towards, or away from each other, leading to longer bounces. If the stress can be made to alternate between compression and tension along the length of the rod, the bounces will be shorter.

Both of these effects can be mitigated by introducing dispersion, as mentioned earlier. A simple dispersion relationship can be used to show this. Consider a square wave propagating in an elastic rod. This wave can be represented, in the frequency domain, by the expression [52]

$$u(x,\omega) = a_1(\omega)e^{-jkx} \tag{3.56}$$

where $a_1(\omega)$ is a frequency dependent coefficient, and k is the wave number. Given an input force $f(t) \Rightarrow F(\omega)$ the coefficient $a_1\omega$ can be found from the boundary condition, through a force balance

$$\frac{\partial u}{\partial x}(x,\omega)|_{x=0} = -\frac{F(\omega)}{EA} \tag{3.57}$$

By subbing in Eq. 3.56 the coefficient is found to be

$$a_1(\omega) = \frac{F(\omega)}{jkEA} \tag{3.58}$$

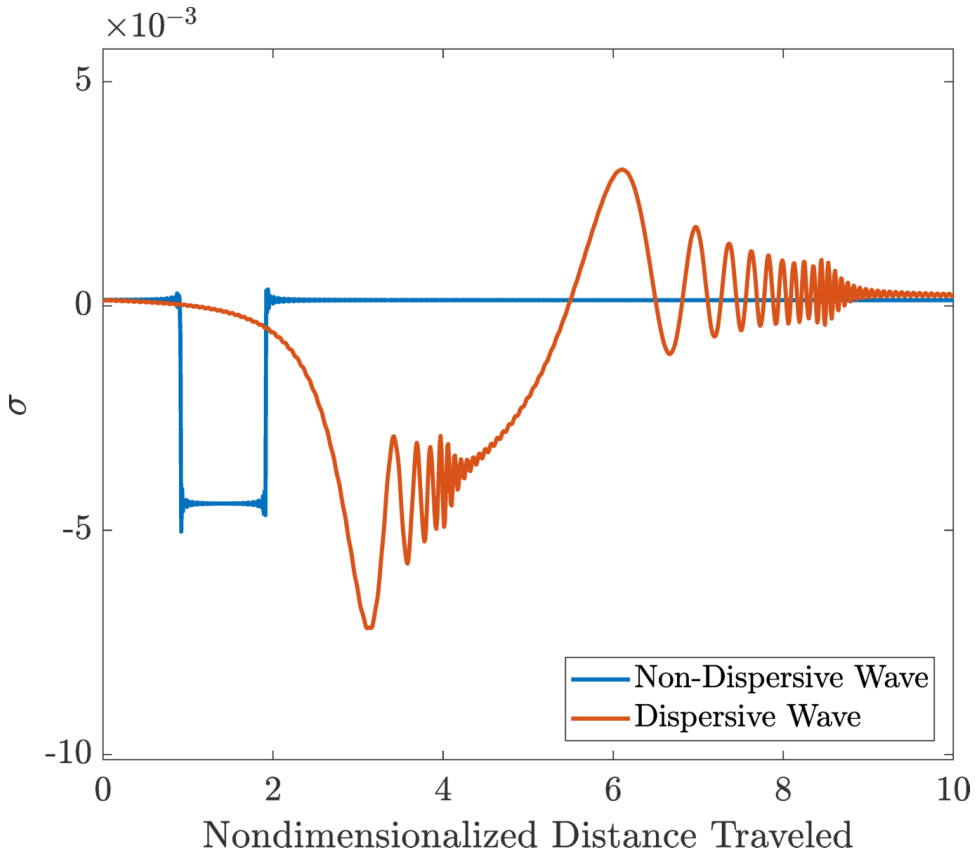

Figure 3.11: Comparison of nondispersive wave and same wave, with dispersion relationship $k = \frac{\omega^{0.9}}{c}$, traveling in a rod.

The final solution in the time domain is

$$u(x,t) = \sum_{\omega} \frac{F(\omega)}{jkEA} e^{-j(kx-\omega t)}. \tag{3.59}$$

For a typical rod $k = \omega/c$, but the effects of dispersion can be investigated by making $k \rightarrow k(\omega)$ an arbitrary function of frequency. By using this equation, and choosing the dispersion relationship $k(\omega)$, an arbitrary dispersion relationship can be investigated to see how it affects the wave shape over time. One possible dispersion relationship is

$$k = \frac{\omega^{0.9}}{c}. \tag{3.60}$$

When this dispersion relationship is applied, the wave is distorted as shown in Fig. 3.11. If this dispersion relationship could be realized in the rod, the wave could be distorted in desirable ways, as discussed above. This dispersive relationship causes the wave to oscillate about zero, as some frequencies move out ahead of others. These oscillations would result in more frequent changes in direction of the electrode tips, leading to more rapid, smaller bounces. The main portion of the wave also moves faster, which would also lead to less stall time. It is anticipated that a dispersion relationship similar to this, could be induced through elastic metamaterials, such as grounding springs or resonators. Elastic metamaterials always introduce dispersion around the edges of the bandgaps of the frequencies that they effect. This concept is investigated in greater detail in Ch. 4.

3.6 Conclusion

The circuit breaker bouncing problem was investigated in this work using analytical and numerical techniques. A model for the circuit breaker was proposed and nondimensionalized. Analytical solutions were then developed and validated with finite difference solutions. These models provided insight into how the circuit breaker bouncing was affected by the waves. The key findings can be summarized as follows:

1. The circuit breaker bounce duration is dependent on both relative wave speed and electrode length. These both directly affect the amount of time it takes a wave to travel in a rod, and can be tuned to achieve shorter bounces.

2. The circuit breaker bounce duration is also dependent on the base spring stiffness for the movable electrode. Generally stiffer base springs lead to short bounces.

3. From observation, the shape of the waves in the electrodes affect the bounce duration, and can be modified through modifying the spring stiffness.

From the results of the model presented and analyzed in this chapter show that the shape of the wave affects the bounce duration. This shape can be modified by introducing dispersion

into the propagating wave. Several mechanisms to do this are introduced in the next chapter.

CHAPTER 4

PULSE SHAPING IN 1D ELASTIC WAVEGUIDES FOR SHOCK TESTING

4.1 Overview

In this chapter a novel application of phononic materials, motivated by Hopkinson bar testing for accelerometers, is presented. The research presented here shows that through using optimized phononic material concepts, an input pulse to a longitudinal bar can be shaped to sufficiently approximate a specified, predefined output pulse. The phononic material bars were modeled analytically using the dynamic stiffness and transfer matrices. Concepts including local resonators, phononic crystals, grounding springs, and cross-sectional variation were explored, and parametric studies showed that no individual parameter of the phononic materials allowed for precise enough control to achieve the possible desired output pulse shapes. The parameters for a combined phononic crystal - local resonator are then tuned using an optimization algorithm to achieve the desired response of the system. The analytical model optimized values were investigated for sensitivity to perturbations which might be introduced during manufacturing, which could reduce the performance of the phononic material. The analytical model was then converted into physical geometry, which when analyzed using the FE method, showed that the desired wave shapes were produced.

4.2 Introduction

Mechanical shock events can be reproduced in the laboratory using Hopkinson bar tests. In general Hopkinson bar tests are used to measure the dynamic properties of a material or system by causing a pulse to travel down an incident rod, via an axial impact from a projectile, and then measuring the pulse reflection and transmission through a sample [53].

These tests are used to qualify electronic systems exposed to mechanical shocks by defining the shape of the pulse as a test specification. In these tests the electronics to be tested are usually placed at the end of the Hopkinson bar instead of between the two sides of a split bar [54]. Hopkinson bar tests are used on MEMS systems, such as accelerometers, which are subject to high accelerations on the order of 100,000 g's [55, 56].

For the Hopkinson bar test a couple of different pulse shaping techniques have previously been developed. One technique inserts a thin disk between the impacting projectile and the incident rod. When the thin disk is impacted it plastically deforms, resulting in a change to the pulse shape created by the projectile. The insert geometry can be designed to control the desired pulse properties [57, 58]. Changing the projectile shape is an alternative technique used to modify the pulse shape. Different shapes can result in pulses with faster or slower rise times as well as a change in pulse duration [59].

Hopkinson bar tests rely on the key assumption that the wave propagating in the rod is non-dispersive. This requirement is satisfied by requiring the rod to be homogeneous with a uniform cross-sectional area, and the wavelength of a pulse to be long compared to the diameter of the bar [53]. When axial impact between two rods occurs the wavelength of the input pulse is twice the length of the impacting rod [45] which means that to avoid dispersion the impacting rod must be long compared to the largest dimension of the cross-section. In this chapter dispersion is intentionally introduced through rod design, as a way to shape pulses to meet desired specifications. It is primarily concerned with determining what rod geometry and features are necessary to produce the desired pulse shape.

Elastic metamaterials introduce dispersion and bandgaps that can be used to modify the shape of a pulse. Single resonator and dual resonator metamaterials have recently been applied to a similar problem, blast mitigation, in an attempt to reduce the amplitude of an input pulse to a system. With the frequency spectrum of the resonators tuned to overlap that of the blast wave, significant wave attenuation occurred [60]. A resonant "woodpile" provided improved blast mitigation by optimizing the individual element length to minimize

the wave force amplitude [61]. Pulse shaping is very similar to the blast mitigation problem, with the caveat that instead of blocking the wave, the wave is allowed to propagate within the structure with designed dispersion characteristics.

Four basic concepts are explored here, with two of them used for actual pulse shaping. The four concepts are phononic crystals, local resonators, cross-sectional variation, and grounding springs. Phononic crystals are built of geometric or material periodicity introduced into a structure [62]. This periodicity leads to an impedance mismatch and creates frequency stop-bands at wavelengths corresponding to the unit cell length of the structure. The second building block is the local resonator. Local resonance effects produce sub-wavelength bandgaps around the natural frequency of the resonators, and generate negative effective mass or stiffness [3]. The third concept, cross-sectional variations, forces the shape of a pulse to change as it travels through a rod [63]. The fourth, grounding springs, is a periodic implementation of an elastic foundation, also known as a Winkler foundation for beams [64]. Elastic foundations in strings, beams, and rods introduce dispersion which does not allow for the propagation of waves at low frequencies [45], i.e. it creates a high-pass filter. Phononic crystals and local resonators were more promising and explored in greater depth for their pulse shaping capabilities.

4.3 Theoretical Background

4.3.1 Input and Output

The input pulse due to an impacter striking the incident rod in a Hopkinson bar test is modeled as a haversine [54]. The input force is then given as

$$f(t) = \frac{f_p}{2}\left(1 - \cos\left(\frac{2\pi}{\tau}t\right)\right) = f_p \sin^2\left(\frac{\pi}{\tau}t\right) \tag{4.1}$$

where f_p is the pulse amplitude and τ is the shock duration. The shock duration is dependent upon the length of the projectile impacting the incident bar and the wave speed. For a

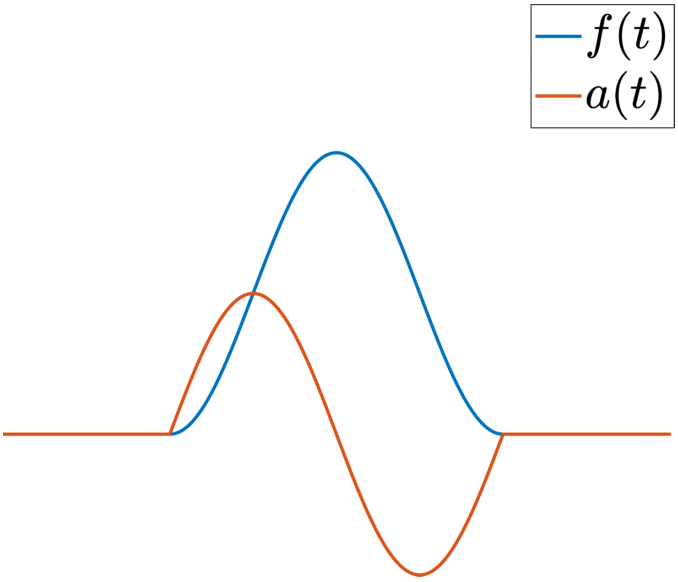

Figure 4.1: Initial force and acceleration wave shapes.

projectile of length L_p with wave speed c_0,

$$\tau = \frac{2L_p}{c_0}. \tag{4.2}$$

This result can be found by applying D'Alembert's solution to the longitudinal impact of two rods [45]. The input force amplitude is also dependent on the impact velocity. However, because this research is only concerned with the overall shape of the wave and the relative amplitude, f_p will be assumed to have a unit value. The results will be applicable to any amplitude wave that satisfies the Hopkinson bar assumptions about wavelength listed earlier. The input acceleration corresponding to the input force pulse is expressed as

$$a(t) = a_p \sin\left(\frac{2\pi}{\tau}t\right). \tag{4.3}$$

where a_p is the acceleration pulse amplitude. Herein the acceleration wave shape is the wave shape to be tuned. One important feature is the fundamental frequency, ω_0 which is

$$\omega_0 = \frac{2\pi}{\tau}. \tag{4.4}$$

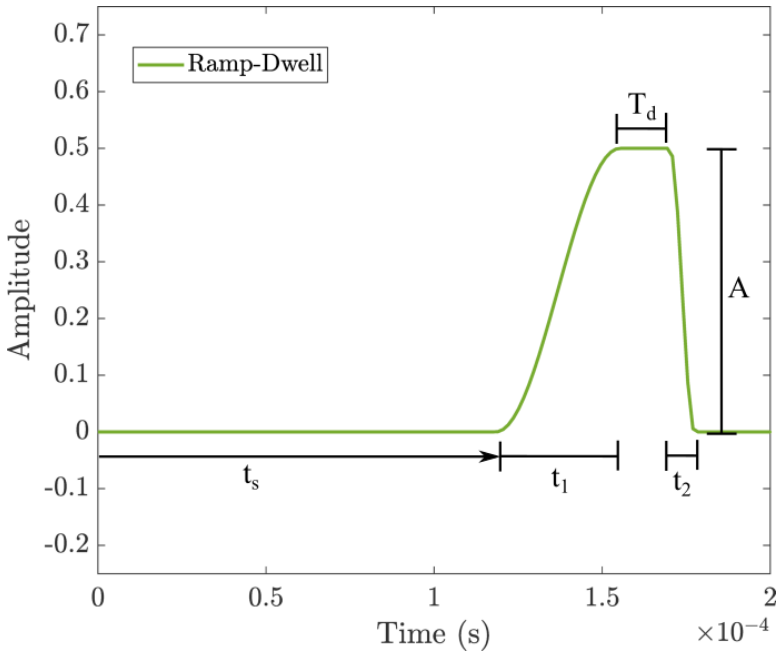

Figure 4.2: Example output curve created from Eq. 4.5.

The input force and acceleration pulse shapes are plotted in Fig. 4.1.

There are two input pulse features of particular interest for Hopkinson bar tests. For tests measuring strain rate dependent material properties a constant strain rate is important, which requires a constant rise in the pulse [57]. For other Hopkinson bar tests, used to study the fracture behavior of materials, the pulse duration is also relevant [58]. The output wave formulation was chosen in order to provide control of the desired strain rate and pulse duration. These properties in an output pulse shape are modeled with the expression

$$a_d(t) = A \begin{cases} 1 - \cos\left(2\pi f_1 t - \phi_1\right) & t_s \leq t \leq t_1 + t_s \\ 1 & t_1 + t_s \leq t \leq t_1 + t_s + T_d \\ 1 - \cos\left(2\pi f_2 t - \phi_2\right) & t_1 + t_s + T_d \leq t \leq t_1 + t_2 + t_s + T_d \\ 0 & \text{otherwise} \end{cases} \tag{4.5}$$

where $f_1 = 1/t_1$, $f_2 = 1/t_2$, $\phi_1 = 2\pi f_1 t_s$, and $\phi_2 = 2\pi f_2(t_s + T_d + t_1 - t_2)$. The subscript d is used to indicate that this is the desired output pulse shape. t_1 and t_2 are the time duration of the rising and falling portion of the waves, T_d is the time duration of the dwell, and A is the amplitude. t_s is the amount of time it takes the wave to travel down the rod. These variables are defined graphically on an example curve in Fig. 4.2.

Equation 4.5 was chosen because it provides a simple way to define the output curve in terms of only a few variables. Equation 4.5 only includes the portion of the pulse before the first zero crossing, and does not represent the entire wave form created by the initial impact. In Hopkinson bar tests the initial pulse is usually followed by additional waves due to various effects, such as reflections off of the ends of the bars. However, only the wave before the first zero crossing is important (even before the wave begins to fall from its first peak) [54]. Because of this, any waves after the first zero crossing were neglected and will not be shown herein.

4.3.2 Transfer and Dynamic Stiffness Matrices

The transfer matrix is used to determine the rod's dispersion relationship, which reveals the effect of different rod parameters on wave dispersion in the frequency domain. Although the transfer matrix can be used to predict wave propagation in the time domain, it is not used here due to ill-conditioning which occurs with increasing numbers of unit cells [65]. Instead the global dynamic stiffness matrix, which avoids this problem, is used to simulate wave propagation through the rod, and to predict what the output wave shape will be in the time domain. Predicting the output wave shape provides a way to study how different metamaterial parameters affect the wave shape. Both of these matrices are developed from the dynamic stiffness matrix for a unit cell. These techniques were also selected because they can be used to predict both dispersion and wave propagation in a variety of periodic configurations.

The dynamic stiffness matrix relates the generalized displacements at the ends of the

Figure 4.3: Example rod unit cell.

rod to their corresponding generalized forces. The transfer matrix method relates the generalized forces and displacements at one end of the rod to the generalized forces and displacements at the other.

For an example unit cell, as shown in Fig. 4.3, the forces and displacements are related by the dynamic stiffness matrix $[D]$, in the frequency domain, as

$$\begin{bmatrix} F_1 \\ F_2 \end{bmatrix} = \begin{bmatrix} D_{11} & D_{12} \\ D_{21} & D_{22} \end{bmatrix} \begin{bmatrix} u_1 \\ u_2 \end{bmatrix}. \tag{4.6}$$

Expressions for D_{ij} vary depending on the features of the unit cell, and will be defined for specific cases later. For arbitrary adjacent sections n and $n+1$ of a rod, as shown in Fig. 4.4, continuity conditions are required to capture the wave propagation from one unit cell to the next. To enforce continuity, at a shared boundary between unit cells the displacements are identical, so $u_{1_{n+1}} = u_{2_n}$. The forces must also be in equilibrium requiring that $F_{1_{n+1}} = -F_{2_n}$. These relationships are necessary to derive the transfer matrix from the dynamic stiffness matrix, because the transfer matrix describes the transference of these quantities from one unit cell to the next. To obtain the transfer matrix, one can rearrange Eq. 4.6 so that the force and displacement for each end are on the same side of the equation, and then apply the continuity conditions to obtain

$$\begin{bmatrix} u_1 \\ F_1 \end{bmatrix}_{n+1} = \begin{bmatrix} -D_{12}^{-1}D_{11} & D_{12}^{-1} \\ D_{22}D_{12}^{-1}D_{11} - D_{21} & D_{22}D_{12}^{-1} \end{bmatrix} \begin{bmatrix} u_1 \\ F_1 \end{bmatrix}_n \tag{4.7}$$

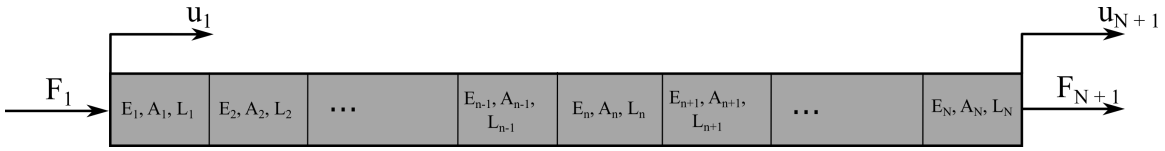

Figure 4.4: A finite rod composed of an arbitrary number of sections.

The transfer matrix then is

$$[T] = \begin{bmatrix} -D_{12}^{-1}D_{11} & D_{12}^{-1} \\ D_{22}D_{12}^{-1}D_{11} - D_{21} & D_{22}D_{12}^{-1} \end{bmatrix} \tag{4.8}$$

For a bar composed of N different sections, as shown in Fig. 4.4, the transfer matrix models how a force in one section would be transferred to the next section by concurrently multiplying the transfer matrices of adjacent cells together. The resulting equation would be

$$\begin{bmatrix} u_1 \\ F_1 \end{bmatrix}_{N+1} = [T]_N[T]_{N-1}\cdots[T]_2[T]_1 \begin{bmatrix} u_1 \\ F_1 \end{bmatrix}_1 = \prod_{i=1}^{N}[T]_i \begin{bmatrix} u_1 \\ F_1 \end{bmatrix}_1 \tag{4.9}$$

The global transfer matrix then becomes a product of the transfer matrices so that

$$[T] = \prod_{i=1}^{N}[T]_i. \tag{4.10}$$

Using this approach, the output wave at one end of the rod can be found from a prescribed input wave at the other end. This same transfer matrix could be used to model a rod of N identical sections, or a periodic system composed of a unit cell consisting of N different sections.

This technique can be used to determine dispersion characteristics in a periodic system by applying the Floquet-Bloch theorem, which says that the state vector at identical places

on adjacent unit cells is the same, but with a phase shift. Mathematically, this is stated as

$$\begin{bmatrix} u_1 \\ \\ F_1 \end{bmatrix}_{n+1} = e^{i\mu} \begin{bmatrix} u_1 \\ \\ F_1 \end{bmatrix}_n \tag{4.11}$$

where $e^{i\mu}$ describes the phase shift at nondimensionalized wave number $\mu = \kappa L$ where L is the length of the unit cell. Using Eq. 4.8

$$\begin{bmatrix} u_1 \\ \\ F_1 \end{bmatrix}_{n+1} = [T] \begin{bmatrix} u_1 \\ \\ F_1 \end{bmatrix}_n = e^{i\mu} \begin{bmatrix} u_1 \\ \\ F_1 \end{bmatrix}_n \tag{4.12}$$

which can be rewritten as

$$\left([T] - e^{i\mu(\omega)}[I]\right) \begin{bmatrix} u_1 \\ \\ F_1 \end{bmatrix}_n = [0] \tag{4.13}$$

The dispersion relationship can be found by solving this eigenvalue problem. To solve, for a given frequency compute the eigenvalues λ and eigenvectors. Then use the relationship $\lambda = e^{i\mu(\omega)}$ to calculate the complex wave number for that given frequency. The real portion of the wave number corresponds to the wave propagation while the imaginary portion corresponds to wave attenuation or amplification, and indicates where band gaps are. The eigenvectors correspond to the wave modes of the system at that frequency.

One of the interesting characteristics of this eigenvalue problem is that the eigenvalues come in complex conjugate pairs. These eigenvalues correspond to wave propagation to the left and to the right. For most systems the wave is attenuated as it propagates, so the correct eigenvalue to use will be the eigenvalue that results in wave attenuation in the direction of

wave propagation. For a wave propagating to the right this will be the eigenvalue that results in a positive imaginary value for μ.

For the prediction of the propagating wave shape the global dynamic stiffness matrix is used. Although this can be done with the transfer matrix, as the number of unit cells increases, meaning the number N in Eq. 4.10 grows larger, the transfer matrix becomes ill-conditioned [65]. Because the global dynamic stiffness matrix does not require the multiplication of multiple matrices, it performs better as far as conditioning is concerned.

The global dynamic stiffness matrix provides the forces and displacements at the beginning and end of each section along a finite rod such as that shown in Fig. 4.4. In order to create this matrix, let Eq. 4.6 represent the ith element of the rod. The global dynamic stiffness matrix is then created by adding overlapping components, similar to the finite element method, as follows,

$$\begin{bmatrix} F^1 \\ F^2 \\ F^3 \\ \vdots \\ F^N \\ F^{N+1} \end{bmatrix} = \begin{bmatrix} D_{11}^1 & D_{12}^1 & & & & \\ D_{21}^1 & D_{22}^1 + D_{11}^2 & D_{12}^2 & & & \\ & D_{21}^2 & D_{22}^2 + D_{11}^3 & & & \\ & & & \ddots & & \\ & & & & D_{22}^{N-1} + D_{11}^N & D_{12}^N \\ & & & & D_{21}^N & D_{22}^N \end{bmatrix} \begin{bmatrix} u^1 \\ u^2 \\ u^3 \\ \vdots \\ u^N \\ u^{N+1} \end{bmatrix} \tag{4.14}$$

where the superscript refers to the element number, with forces and displacement representing the forces and displacements of the left end of the element. All terms left unspecified are zero. The internal forces sum to zero, so $F^2 = F^3 = ... = F^N = 0$. The initial force F^1 is prescribed by the chosen input wave form, i.e. the frequency domain representation of Eq. 4.1, and the output force corresponds to a free end so $F^{N+1} = 0$ also.

Equation 4.14 captures all pulse reflections within the phononic material. This includes zero crossings that occur after the initial pulse. Only the initial pulse, before the first zero crossing, is used in testing the accelerometers or measuring other dynamic material properties. Portions of the wave beyond the first zero crossing are not of interest for this work, therefore they are not shown in the results.

The dynamic stiffness matrix is defined in the frequency domain. In order to use the dynamic stiffness matrix the input pulse shape must be transformed into the frequency domain. Once all of the forces and terms in the dynamic stiffness matrix have been specified, simply invert the dynamic stiffness matrix to find the frequency domain displacements for each of the degrees of freedom. All other quantities of interest, such as acceleration or stress, can then be calculated from the displacement. Finally, to get the pulse shape, transform back from the frequency domain to the time domain.

4.3.3 Longitudinal Rod Governing Equation

The dynamic stiffness matrix and transfer matrix were derived without determination of the properties of the rod they would be modeling. Now that the framework for modeling has been developed, the phononic unit cells themselves can be modeled. The bars in the Hopkinson bar experiment are modeled using the longitudinal wave equation

$$\frac{\partial^2 u}{\partial x^2} = \frac{1}{c_0^2}\frac{\partial^2 u}{\partial t^2} \tag{4.15}$$

where $c_0 = \sqrt{E/\rho}$, and E and ρ are the Young's modulus and density, respectively. The coordinate x and displacement, u are shown in Fig. 4.5. This formulation assumes a constant cross-section, linear elastic material, and uniform stress distribution over the cross section. Waves modeled by Eq. 4.15 are nondispersive. This formulation assumes that the lateral inertia, taken into account through the Poisson ratio, is negligible. For the main frequency components of interest for the input waves simulated here this assumption holds

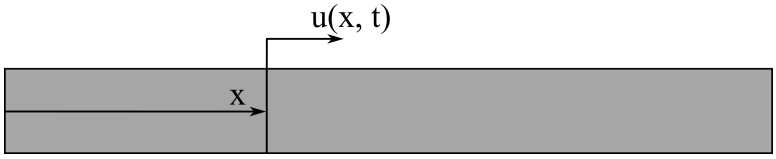

Figure 4.5: Coordinates and displacement for a longitudinal rod.

true. Assuming time harmonicity, Eq. 4.15 reduces to

$$\frac{\partial^2 u}{\partial x^2} + \frac{\omega^2}{c_0^2} u = 0 \tag{4.16}$$

which has the solution

$$u(x) = A_1 e^{i\kappa x} + A_2 e^{-i\kappa x}. \tag{4.17}$$

4.3.4 Dynamic Stiffness Matrix

The dynamic stiffness matrix for a rod unit cell is found by evaluating Eq. 4.17 at the boundaries. This leads to the equations

$$u_1 = u(0) = A_1 + A_2 \tag{4.18}$$

$$u_2 = u(L) = A_1 e^{i\kappa L} + A_2 e^{-i\kappa L} \tag{4.19}$$

$$F_1 = -EA\frac{\partial u}{\partial x}(0) = -EAi\kappa(A_1 - A_2) \tag{4.20}$$

$$F_2 = EA\frac{\partial u}{\partial x}(L) = EAi\kappa\left(A_1 e^{i\kappa L} - A_2 e^{-i\kappa L}\right) \tag{4.21}$$

which can be solved to eliminate A_1 and A_2 to get the matrix equation

$$\begin{bmatrix} F_1 \\ \\ F_2 \end{bmatrix} = \frac{EA\kappa}{\sin(\kappa L)} \begin{bmatrix} \cos(\kappa L) & -1 \\ \\ -1 & \cos(\kappa L) \end{bmatrix} \begin{bmatrix} u_1 \\ \\ u_2 \end{bmatrix}. \tag{4.22}$$

The dynamic stiffness matrix is the matrix in Eq. 4.22 that relates the displacement and force vectors. Eq. 4.22 shows the contents of the dynamic stiffness matrix presented in Eq.

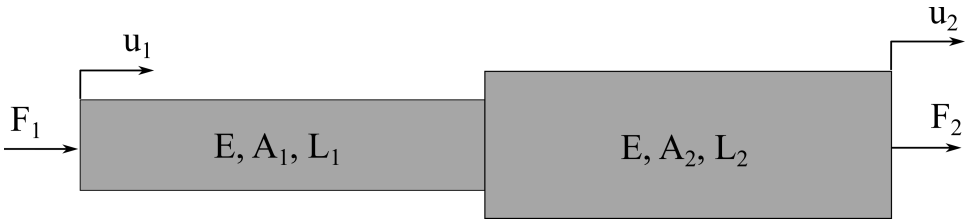

Figure 4.6: Example of a phononic crystal unit cell.

4.6 for a straight rod. The transfer matrix is then found from Eq. 4.22 using Eq. 4.8.

A phononic crystal unit cell is shown in Fig. 4.6. The transfer matrix for a phononic crystal is found using the transfer matrix for two separate rods and then applying the transfer matrix multiplication property in Eq. 4.10 so that

$$[T]_{pc} = [T]_2 [T]_1 . \tag{4.23}$$

The global dynamic stiffness matrix can be created by alternating matrices $[D]_1$ and $[D]_2$ for the respective rod sections that they represent as shown in Eq. 4.14.

A unit cell for a rod with local resonators is shown in Fig. 4.7. The dynamic stiffness matrix for a rod with a resonator is derived in the same way, but the right boundary force balance (Eq. 4.21) becomes

$$\begin{aligned} F_2 &= EA\frac{\partial u}{\partial x}(L) + k_r(u_2 - u_r) \\ &= EAi\kappa \left(A_1 e^{i\kappa L} - A_2 e^{-i\kappa L}\right) + k_r(u_2 - u_r) \end{aligned} \tag{4.24}$$

with the mass spring resonator modeled by the equation

$$m_r \ddot{u}_r + k_r(u_r - u_2) = 0. \tag{4.25}$$

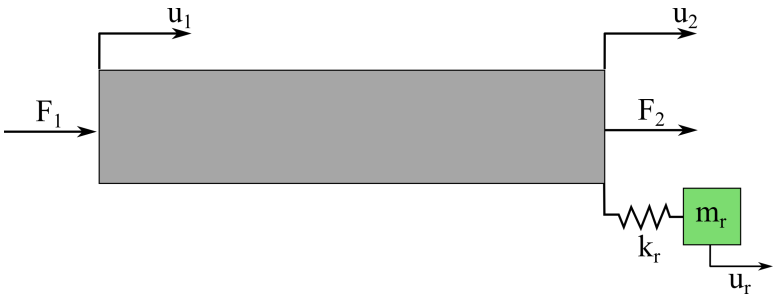

Figure 4.7: Example of a unit cell for a rod with periodically applied local resonators.

Using the assumption of time harmonicity, Eq. 4.25 is rearranged to find that

$$u_r = \frac{1}{1 - \left(\frac{\omega}{\omega_r}\right)^2} \tag{4.26}$$

where $\omega_r = \sqrt{k_r/m_r}$. Equation 4.26 is used to eliminate u_r in Eq. 4.24. Then using Eqs. 4.18 – 4.20 with Eq. 4.24 the matrix equation for a local resonator is found to be

$$\begin{bmatrix} F_1 \\ \\ F_2 \end{bmatrix} = \begin{bmatrix} EA\kappa\frac{\cos(\kappa L)}{\sin(\kappa L)} & -\frac{EA\kappa}{\sin(\kappa L)} \\ \\ -\frac{EA\kappa}{\sin(\kappa L)} & EA\kappa\frac{\cos(\kappa L)}{\sin(\kappa L)} - k_r\frac{(\omega/\omega_r)^2}{1-(\omega/\omega_r)^2} \end{bmatrix} \begin{bmatrix} u_1 \\ \\ u_2 \end{bmatrix}. \tag{4.27}$$

The matrix in Eq. 4.27 is the dynamic stiffness matrix presented in Eq. 4.6 for a rod with a local resonator attached. This dynamic stiffness matrix is identical to that of the rod, with the addition of the k_r term in the bottom right element.

A unit cell for a rod with a grounding spring is shown in Fig. 4.8. This can be thought of as a limiting case for the local resonator with infinite mass. Equations 4.18 - 4.20 are the same, but the force balance at the right end becomes

$$\begin{aligned} F_2 &= EA\frac{\partial u}{\partial x}(L) + k_g u_2 \\ &= EAi\kappa\left(A_1 e^{i\kappa L} - A_2 e^{-i\kappa L}\right) + k_g u_2. \end{aligned} \tag{4.28}$$

Figure 4.8: Rod unit cell with a grounding spring.

Solving Eqs. 4.18 – 4.20 with Eq. 4.28 leads to the matrix equation

$$\begin{bmatrix} F_1 \\ \\ F_2 \end{bmatrix} = \begin{bmatrix} EA\kappa\frac{\cos(\kappa L)}{\sin(\kappa L)} & -\frac{EA\kappa}{\sin(\kappa L)} \\ \\ -\frac{EA\kappa}{\sin(\kappa L)} & EA\kappa\frac{\cos(\kappa L)}{\sin(\kappa L)} + k_g \end{bmatrix} \begin{bmatrix} u_1 \\ \\ u_2 \end{bmatrix}. \tag{4.29}$$

The matrix in Eq. 4.29 is the dynamic stiffness matrix for a rod with a grounding spring attached. The only difference between the matrix in Eq. 4.22 for the original rod and this one is the addition of the k_g term in the bottom right element.

A unit cell for a rod with an exponentially varying cross-section is shown in Fig. 4.9. The cross-sectional variation results in a different governing equation. For this specific case, the governing equation is

$$\frac{1}{A(x)}\frac{\partial}{\partial x}\left(A(x)\frac{\partial u}{\partial x}\right) = \frac{1}{c_0^2}\frac{\partial^2 u}{\partial t^2} \tag{4.30}$$

The final governing equation will depend on the choice of cross-sectional variation. Not all cross-sectional variations result in analytically solvable governing equations. For the purposes of this work, the cross-section will be restricted to the analytically solvable exponential variation of the form

$$A(x) = \pi r^2(x) = \pi\left(r_0 e^{-\beta x}\right)^2, \tag{4.31}$$

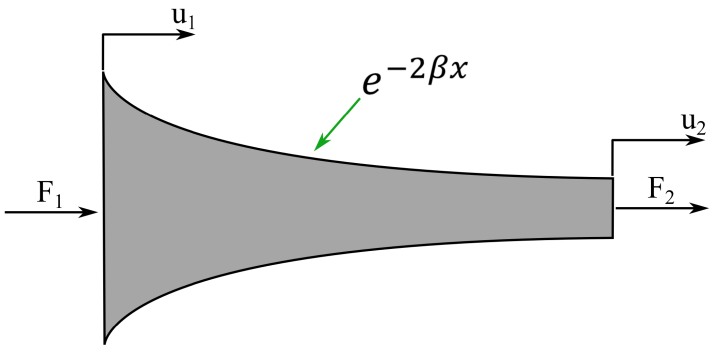

Figure 4.9: Rod with an exponentially decaying cross-sectional area.

where r is the rod radius, r_0 is the radius value at $x = 0$, and β controls the exponential decay or growth of the rod.

This profile falls into the class of cross-sectional variations known as 'horns,' which can behave as amplifiers or attenuators [45]. A positive value of β results in exponential decay as x grows. This leads to a smaller cross-section at the terminal unit cell or rod end and a larger amplitude wave. A negative value results in exponential growth in cross-sectional area, a larger cross-section at the terminal end of the rod, and as a result a smaller amplitude wave. If the cross-sectional area at the ends is specified then this can be used in Eq. 4.31 to solve for the necessary value of β. To do this, let $\alpha = A(L)/A(0)$ which when evaluated using Eq. 4.31 and solving for β gives that

$$\beta = -\frac{1}{2L} \ln \alpha. \tag{4.32}$$

When Eq. 4.31 is used for the cross-sectional variation and assuming time harmonic vibration, Eq. 5.2 becomes

$$\frac{\partial^2 u}{\partial x^2} - 2\beta \frac{\partial u}{\partial x} + \frac{\omega^2}{c_0^2} = 0 \tag{4.33}$$

The solution is then in the form

$$u(x) = A_1 e^{\left(\beta + i\sqrt{\kappa^2 - \beta^2}\right)x} + A_2 e^{\left(\beta - i\sqrt{\kappa^2 - \beta^2}\right)x} \tag{4.34}$$

When Eq. 4.34 is evaluated at the boundaries the resulting four equations are

$$u_1 = u(0) = A_1 + A_2 \tag{4.35}$$

$$u_2 = u(L) = A_1 e^{\left(\beta + i\sqrt{\kappa^2 - \beta^2}\right)L} + A_2 e^{\left(\beta - i\sqrt{\kappa^2 - \beta^2}\right)L} \tag{4.36}$$

$$F_1 = -EA(0)\frac{\partial u}{\partial x}(0) = -EA(0)\left(A_1\left(\beta + i\sqrt{\kappa^2 - \beta^2}\right) - A_2\left(\beta - i\sqrt{\kappa^2 - \beta^2}\right)\right) \tag{4.37}$$

$$\begin{aligned} F_2 = EA(0)\frac{\partial u}{\partial x}(L) = EA(L)\Bigg(&A_1\left(\beta + i\sqrt{\kappa^2 - \beta^2}\right)e^{\left(\beta + i\sqrt{\kappa^2 - \beta^2}\right)L} \\ &-A_2\left(\beta - i\sqrt{\kappa^2 - \beta^2}\right)e^{\left(\beta - i\sqrt{\kappa^2 - \beta^2}\right)L}\Bigg) \end{aligned} \tag{4.38}$$

which lead to the matrix equation

$$\begin{bmatrix} F_1 \\ \\ F_2 \end{bmatrix} = \begin{bmatrix} D_{e_{11}} & D_{e_{12}} \\ \\ D_{e_{21}} & D_{e_{22}} \end{bmatrix} \begin{bmatrix} u_1 \\ \\ u_2 \end{bmatrix}. \tag{4.39}$$

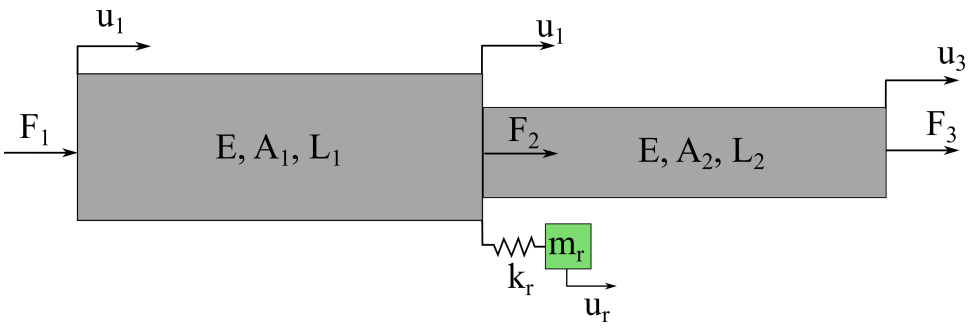

Figure 4.10: Unit cell combining both a phononic crystal and local resonance into a single elastic metamaterial.

where

$$C_e = \frac{E}{e^{\beta L}\sin(\sqrt{\kappa^2-\beta^2}L)} \tag{4.40}$$

$$D_{e_{11}} = -\beta e^{\beta L} C_e A(0)\sin\left(\sqrt{\kappa^2-\beta^2}L\right) + \sqrt{\kappa^2-\beta^2}e^{\beta L}C_e A(0)\cos\left(\sqrt{\kappa^2-\beta^2}L\right) \tag{4.41}$$

$$D_{e_{12}} = -C_e A(0)\sqrt{\kappa^2-\beta^2} \tag{4.42}$$

$$D_{e_{21}} = -C_e A(0) e^{2\beta L}\sqrt{\kappa^2-\beta^2} \tag{4.43}$$

$$D_{e_{22}} = \beta e^{\beta L} C_e A(0)\sin\left(\sqrt{\kappa^2-\beta^2}L\right) + \sqrt{\kappa^2-\beta^2}e^{\beta L}C_e A(0)\cos\left(\sqrt{\kappa^2-\beta^2}L\right) \tag{4.44}$$

The dynamic stiffness matrix for an exponential rod is given in Eq. 4.39 with components given by Eqs. 4.40 – 4.44.

Finally, a combination of the phononic crystal and resonator concepts was also explored in a single unit cell, as shown in Fig. 4.10. The dynamic stiffness matrix for the first part is given by Eq. 4.27 and for the second part by Eq. 4.22. The transfer matrix for this unit cell is found using Eq. 4.23.

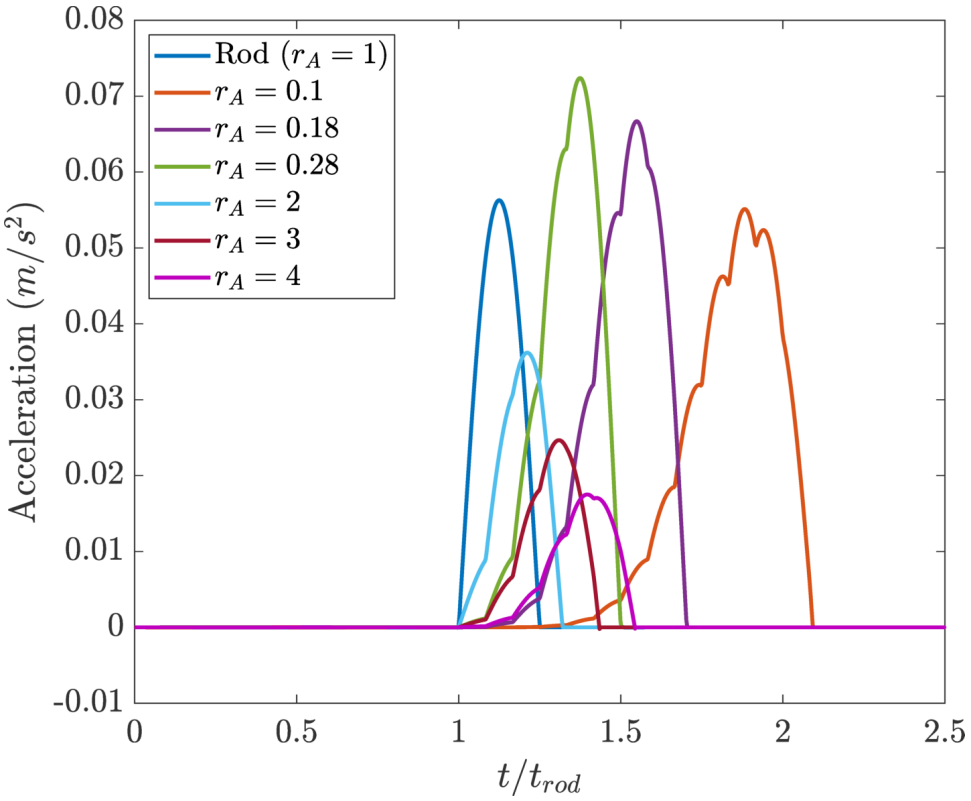

Figure 4.11: Effect of change in the phononic crystal cross-sectional area on the output pulse shape.

4.4 Parametric Studies

Parametric studies of the phononic crystal, local resonator, ground spring, and exponentially varying metamaterials were conducted using Eq. 4.14 to determine the various parameters' effect on the output wave shape.

4.4.1 Phononic Crystal

For a phononic crystal three variables were investigated including:

1. Cross sectional area $r_A = \frac{A_2}{A_1}$
2. Unit cell length $r_{L_{uc}} = \frac{L_1+L_2}{L_{i1}+L_{i2}}$ where L_{ij} is the initial length of the jth section.
3. Relative section lengths $L_r = \frac{L_1}{L_1+L_2}$

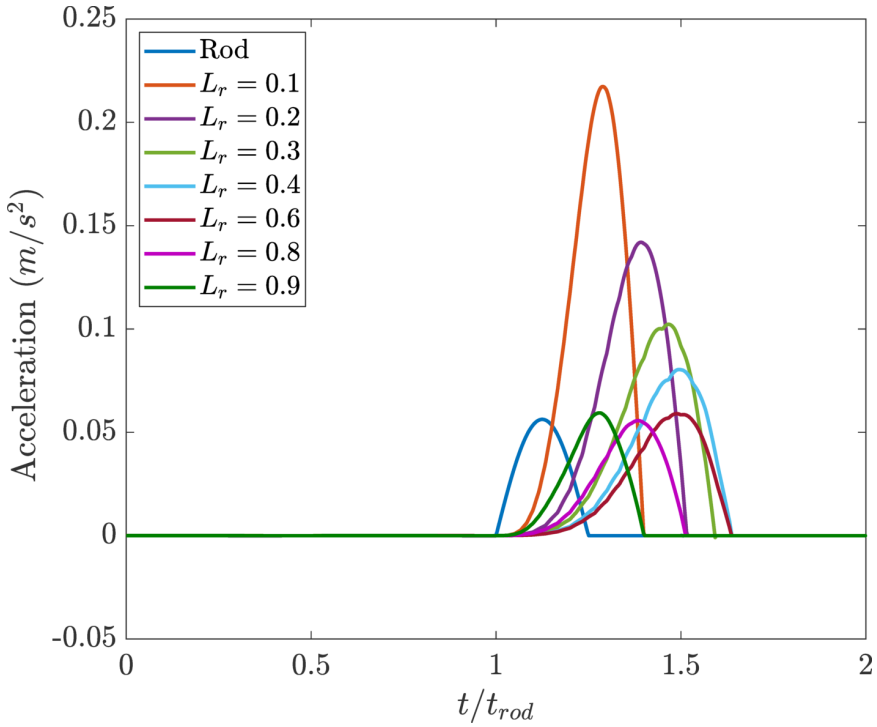

Figure 4.12: Effect of change of relative section lengths in the phononic crystal on the output pulse shape.

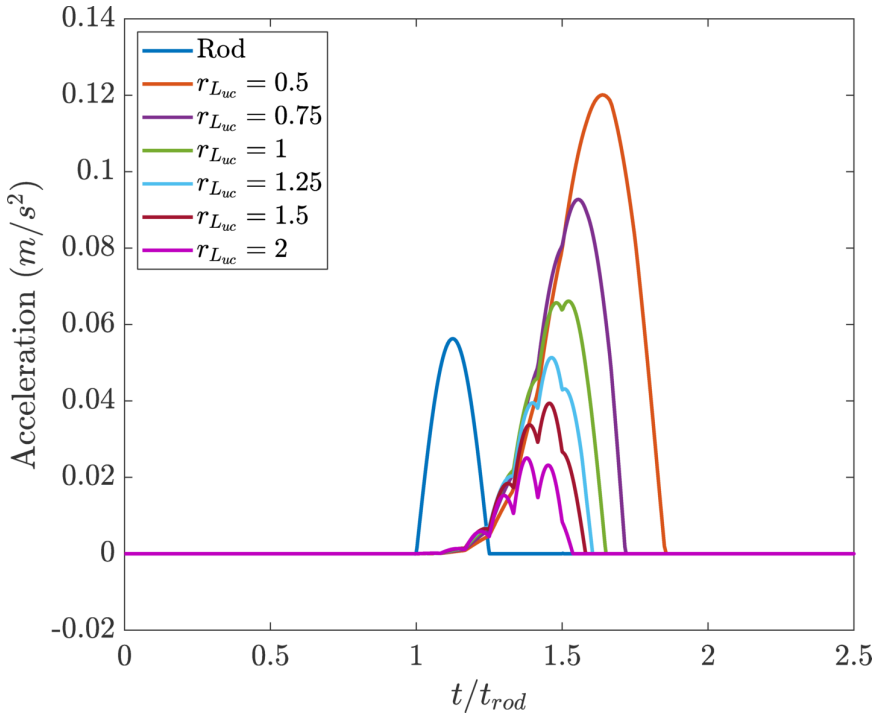

Figure 4.13: Effect of phononic crystal unit cell length on the output pulse shape.

Wave shapes for the parametric studies on cross-sectional area, phase length, and unit cell length are shown in Figs. 4.11 – 4.13. The number of unit cells used for the parametric studies was fixed at 12.

In Fig. 4.11 as r_A decreases from 0.28 to 0.1 the pulse shape decreases in amplitude and has a longer rise time. Ripples, or lobing, starts to develop as r_A becomes smaller. As r_A grows from a value of 1 the amplitude significantly decreases, and the rise time also increases. Figure 4.12 shows an interesting change in the shape of the waves, where very little ripples occur, but the rise time initially increases, and then decreases as L_r approaches a value of unity. In Fig. 4.13 as the unit cell length increases the amplitude of the wave decreases, and ripples in the wave become more pronounced.

4.4.2 Local Resonator

For the local resonator elastic metamaterial two variables were investigated, including:

1. Resonator mass $r_m = \frac{m_r}{m_{rod}}$ where m_{rod} is the mass of the unit cell rod.

2. Natural frequency $r_\omega = \frac{\omega_r}{\omega_0}$ where ω_0 is the fundamental frequency of the input pulse. r_ω measures how close the resonator natural frequency is to the fundamental input frequency.

These results are shown Figs. 4.14 and 4.15 respectively. The resonator introduces a sinusoidal curve into the output pulse. Because of this, sometimes the initial pulse drops below zero very rapidly, leading to a shorter wave duration. For small values of m_r the resonator does not have a dramatic effect on the shape of the wave. As m_r increases the a sinusoid begins to appear in the curve. Once the mass of the resonator moves past approximately $1/2$ the mass of the rod the amplitude of this additional sinusoid has increased to the point where it causes the first zero crossing to appear much sooner. The parametric study of the natural frequency shows that the affect of the sinusoid decreases as the resonance moves away from the fundamental frequency. This suggests that the resonator only affects the

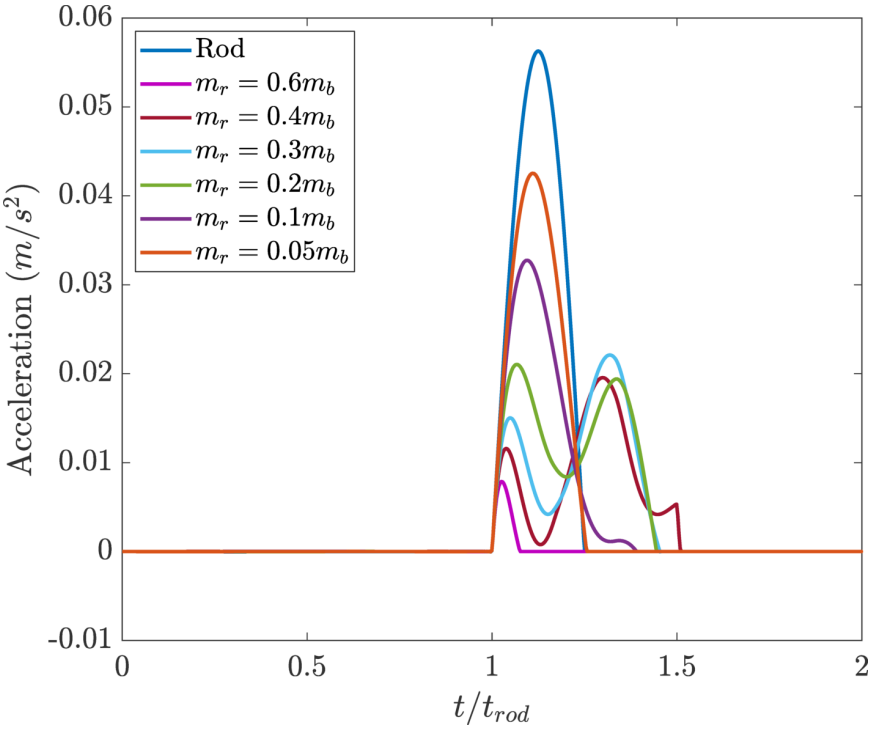

Figure 4.14: Effect of change in the resonator mass on the output pulse shape.

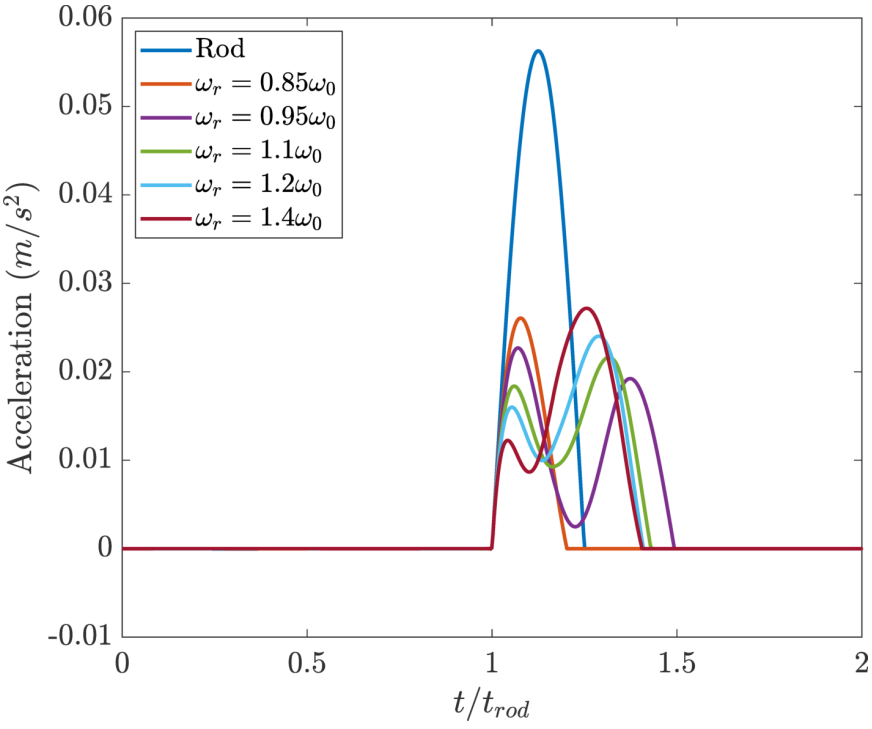

Figure 4.15: Effect of change in the resonator frequency on the output pulse shape.

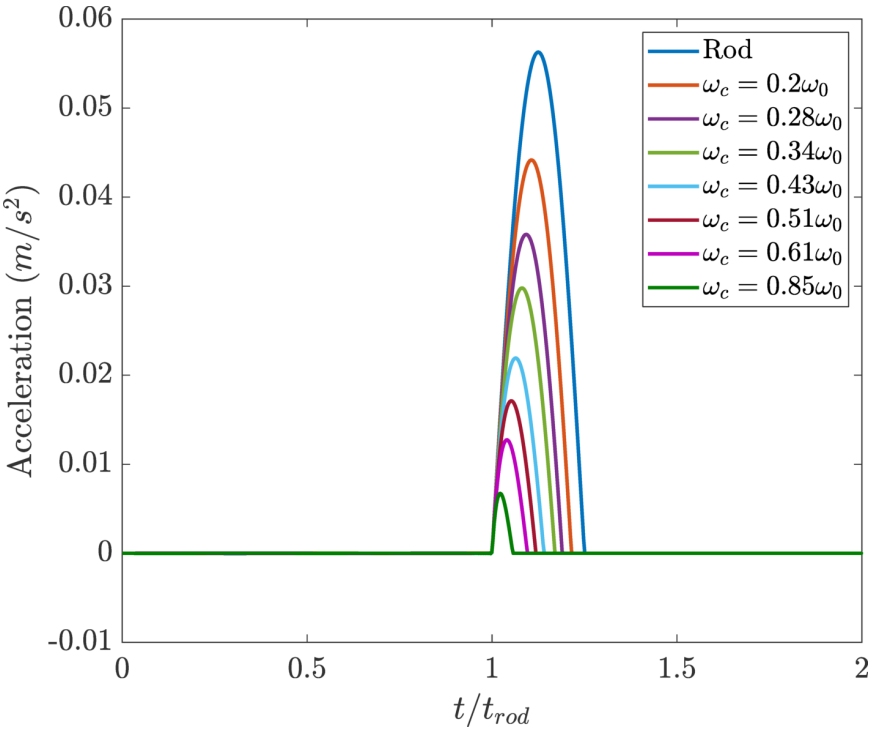

Figure 4.16: Effect of ground spring cut-off frequency on the output pulse shape.

shape of the wave when its resonance is sufficiently close to the input wave fundamental frequency.

4.4.3 Grounding Springs

For the grounding spring phononic material the grounding spring forms a high pass filter. The effect of moving the filter cut-off frequency ω_c on the shape of the input pulse was investigated by increasing the cutoff frequency from zero (no grounding springs) to $0.85\omega_0$. These results are shown in Fig. 4.16. As the cut-off frequency grows closer to the fundamental frequency ω_0 the wave amplitude is attenuated. This trend continues as the cut-off frequency increases past the fundamental frequency. These results suggest that the grounding spring concept could be a useful tool for blocking or attenuating wave propagation, but not for tuning the shape of a propagating pulse, therefore grounding springs were not explored further.

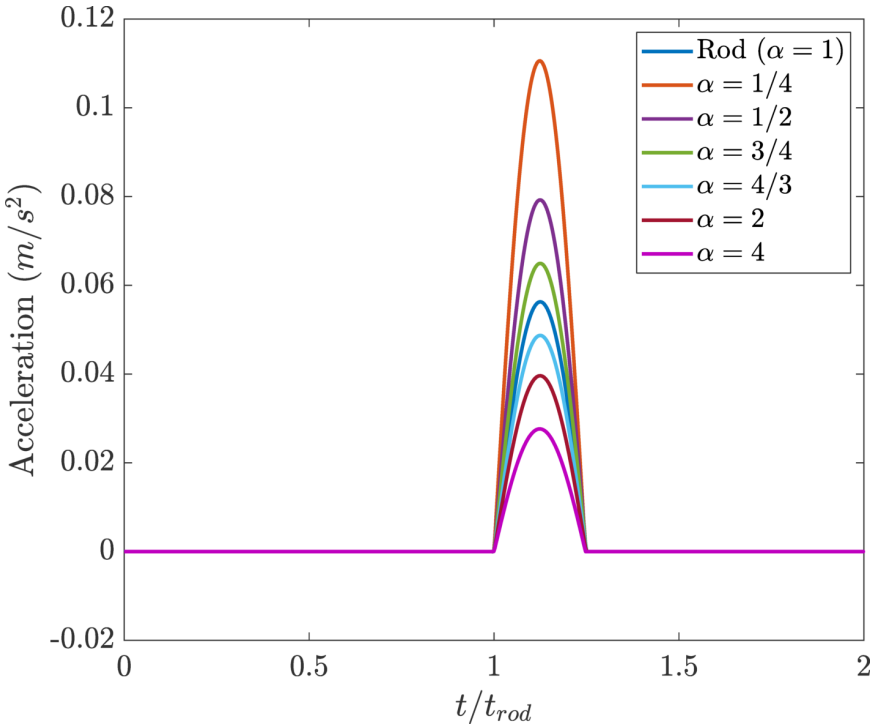

Figure 4.17: Effect of different exponentially decaying cross-sectional areas on wave shape, with $\alpha = A(L)/A(0)$ being the ratio between initial and final cross-sectional areas.

4.4.4 Exponentially Varying Cross Section

For the exponentially varying cross section only a single unit cell the entire length of the rod was used, to demonstrate the amplification and attenuation effects of this cross-sectional variation. These results are shown in Fig. 4.17. As the cross-sectional ratio α becomes larger the wave amplitude becomes proportionately smaller. As α becomes smaller the wave becomes proportionately larger. The amplitude decreases because the wave energy is spread over a larger area, and increases when the wave energy is concentrated in a smaller area. This suggests that this particular concept could be used to scale the desired amplitude of the output wave shape.

4.5 Optimization

The combination of the local resonator and phononic crystal, as shown in Fig. 4.10 was optimized to create desired pulse shapes. A preliminary optimization for several different wave types was conducted in Matlab using the analytical model. A sensitivity analysis was then performed to determine how perturbations in the optimized parameters would affect the output pulse shape. Physical metamaterial geometry was then optimized in Abaqus. The number of unit cells was fixed at 9 because this has been shown to be sufficient to get the full effect of a periodic structure [30]. Two main categories of wave shapes, dwells and ramps, were investigated to determine whether or not pulses could be shaped to achieve shapes that highlight two features of interest for pulses in Hopkinson bar tests: the wave duration, and the rising wave, as noted in Sec. 4.3.1. Finally, as noted earlier, only the portion of the pulse before the first zero crossing is of interest.

4.5.1 Fitness Function

For optimization, the error between the actual output curve and the desired output curve is

$$e(t) = a_d(t) - a_o(t). \tag{4.45}$$

The error measurement of a pulse is then calculated by taking the integral of the squared error

$$E = \int_0^T e^2(t)dt \tag{4.46}$$

which is shown graphically in Fig. 4.18. This is also known as the L^2 norm of the error. The L^2 norm was chosen because it is a standard error measurement used for optimization and provides a sufficient measure of the difference between the desired and expected output waves for the optimization routine.

This error measurement is sufficient for the optimization routine, but does not provide

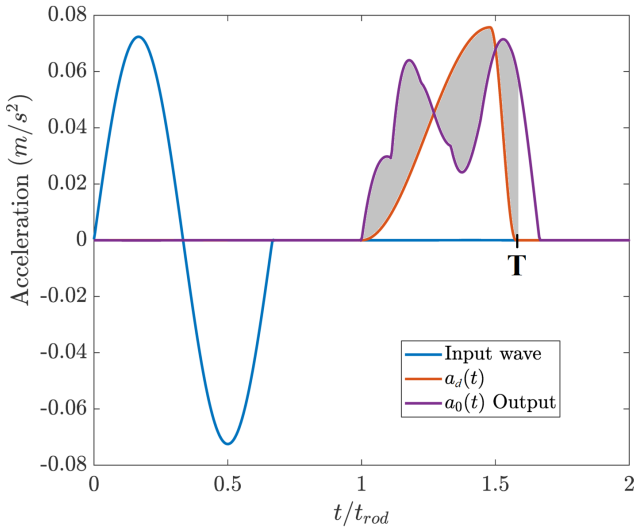

Figure 4.18: Graphical representation of the error integration in Eq. 4.46 with the error to be integrated up to the end of the desired output curve, shown in gray.

a good measure of how close the optimized wave matches the desired wave, because the optimization tries to make the output value of Eq. 4.46 as close to zero as possible, in absolute terms. For reporting purposes, the error between the desired output wave and the actual output wave will be reported as the ratio of the L_2 norms of the actual and desired outputs, given as

$$E_{L_2} = \frac{\|a_o\|}{\|a_d\|}. \tag{4.47}$$

This expression provides a relative comparison between the two waves. A unit value represents a perfect match, and non-unit values describes the relative goodness of fit.

4.5.2 Analytical Model Optimization Results

The optimization variables used for the analytical model were the cross-sectional area ratio r_A, the unit cell total length ratio $r_{L_{uc}}$, the unit cell phase length ratio L_r, the resonator to unit cell mass ratio r_m, and the ratio of resonance to fundamental input frequency r_ω, as presented earlier in the parametric study. In Matlab the optimization was performed using the *fminsearch* function which uses the Nelder-Mead simplex algorithm.

Results of the optimization routine for three different ramp type waves are shown in

Table 4.1: Optimized parameter values for ramp type waves.

t_1, t_2	$r_m = \frac{m_r}{m_{rod}}$	$r_\omega = \frac{\omega_r}{\omega_0}$	$r_A = \frac{A_2}{A_1}$	$L_r = \frac{L_1}{L_1+L_2}$	$r_{L_{uc}} = \frac{L_1+L_2}{L_{i1}+L_{i2}}$	$E_{L_2} = \frac{\|a_o\|}{\|a_d\|}$
$\frac{5}{6}\tau$, $\frac{1}{6}\tau$	0.259	1.244	0.442	0.401	1.156	1.016
$\frac{1}{2}\tau$, $\frac{1}{2}\tau$	0.127	1.179	0.246	0.866	1.046	1.010
$\frac{1}{6}\tau$, $\frac{5}{6}\tau$	0.137	1.083	0.675	0.458	1.762	0.931

Fig. 4.19. The results show some ripples in the rising wave, but overall demonstrate good consistency with the desired output waves. Table 4.1 shows the values of the optimized variables for each wave shape and the error measurement. The optimized output for the $5/6\tau$, $1/6\tau$ and $1/2\tau$, $1/2\tau$ ramp type waves was very close to the desired wave shapes with a difference in the L_2 norms of 0.02 or less. The $1/6\tau$, $5/6\tau$ optimized wave was also close but had a difference in the L_2 norm of 0.07 indicating that the optimized metamaterial structure was not able to approximate this leftward sloping wave quite as well.

In addition to the three different ramps shown in Fig. 4.19 another four rightward facing ramps were investigated. The rightward facing ramps were investigated further because achieving lower slopes with slower rise times is often desired for Hopkinson bar tests investigating rate dependent loading properties. Results from the FE optimization, presented in the next section (Sec. 4.5.4) also suggested that this wave shape would be easier to achieve for phononic materials. Results for the metamaterial optimization for rightward facing ramps are shown in Fig. 4.20 with optimized parameters in Table 4.2.

The results show an unexpected trend – that the metamaterial performs better at pulse shaping as the rise times become longer and the fall times become shorter. The symmetric wave, which had an error of 0.01 when the total duration of the wave was τ, had an error of 0.15 when the total wave duration was 2τ. There are several factors that probably contribute to this. The original wave input is of duration τ, so the metamaterial needs to stretch the wave. This can be accomplished by slowing down some of the frequency content of the wave. However, the hybrid metamaterial/phononic crystal investigated herein is not able to do that, especially for longer waves, in a symmetric manner.

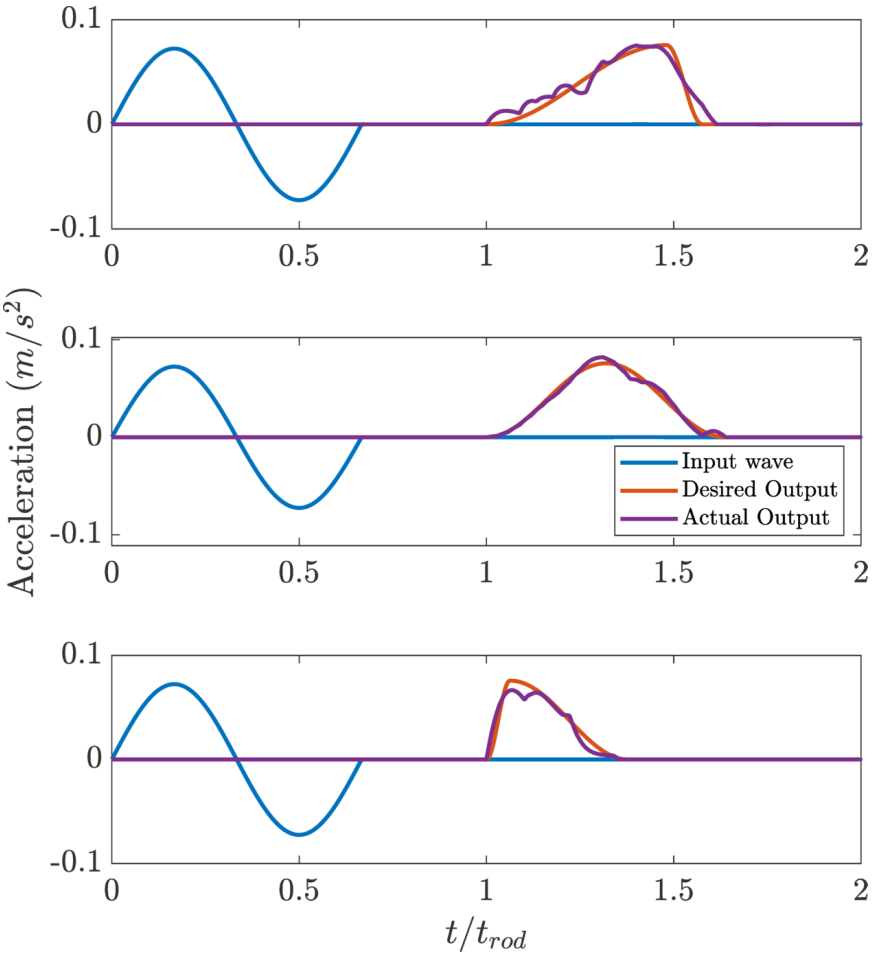

Figure 4.19: Optimized wave shapes for ramp type desired outputs, with the top, middle, and bottom waves having $t_1 = 5/6\tau, t_2 = 1/6\tau$; $t_1 = 1/2\tau, t_2 = 1/2\tau$; and $t_1 = 1/6\tau, t_2 = 5/6\tau$ respectively, all with $T_d = 0$ (no dwell) as defined in Fig. 4.2.

Table 4.2: Optimized parameter values for longer ramp type waves.

t_1, t_2	$r_m = \frac{m_r}{m_{rod}}$	$r_\omega = \frac{\omega_r}{\omega_0}$	$r_A = \frac{A_2}{A_1}$	$L_r = \frac{L_1}{L_1+L_2}$	$r_{L_{uc}} = \frac{L_1+L_2}{L_{i1}+L_{i2}}$	$E_{L_2} = \frac{\|a_o\|}{\|a_d\|}$
τ, τ	0.200	0.895	0.227	0.180	1.856	0.854
$\frac{5}{4}\tau$, $\frac{3}{4}\tau$	0.164	0.983	0.213	0.268	1.783	0.875
$\frac{3}{2}\tau$, $\frac{1}{2}\tau$	0.250	1.382	0.184	0.345	1.233	0.921
$\frac{7}{4}\tau$, $\frac{1}{4}\tau$	0.271	1.233	0.185	0.183	1.485	0.982

Results of the optimization routine for three different square type waves are shown in Fig. 4.21. In each successive wave the dwell becomes a little bit longer, and the rise and fall times are reduced. In a similar fashion to the ramps, these waves show some ripples, but overall are consistent with the desired output wave shapes. The values of the optimized variables, with the wave error measurement, are shown in Table 4.3. There is a clear trend in the L_r ratio. As the length of the dwell increases the L_r ratio becomes smaller. r_ω also decreases. For each of these waves the output wave shape very closely matches the desired wave shape, with the $\frac{1}{3}\tau$, $\frac{1}{3}\tau$, $\frac{1}{3}\tau$ and $\frac{1}{4}\tau$, $\frac{1}{2}\tau$, $\frac{1}{4}\tau$ waves having an error measurement of less than 0.01, and the $\frac{1}{6}\tau$, $\frac{2}{3}\tau$, $\frac{1}{6}\tau$ wave having an error measurement of 0.031. When optimized, the proposed metamaterial very effectively achieves this class of wave shapes.

The way that the optimization routine modifies the wave shape becomes clearer in the dispersion relationships for the waves. Figures 4.22 – 4.24 show the dispersion relationships for the small, medium, and large dwells, respectively. The transfer functions between the rod inputs and optimized output waves were also calculated. The dispersion relationships are lined up in the frequency domain with their corresponding transfer function amplitudes.

The dispersion relationships show that as the dwell becomes larger, the band gap introduced by the phononic crystal becomes narrower, and the band gap introduced by the local resonator moves closer to the fundamental frequency $\omega = \omega_0$. The transfer function shows that bandgaps predicted by the dispersion relationship do in fact occur in the frequency domain of the propagated wave, as shown by the low amplitude portions of the transfer

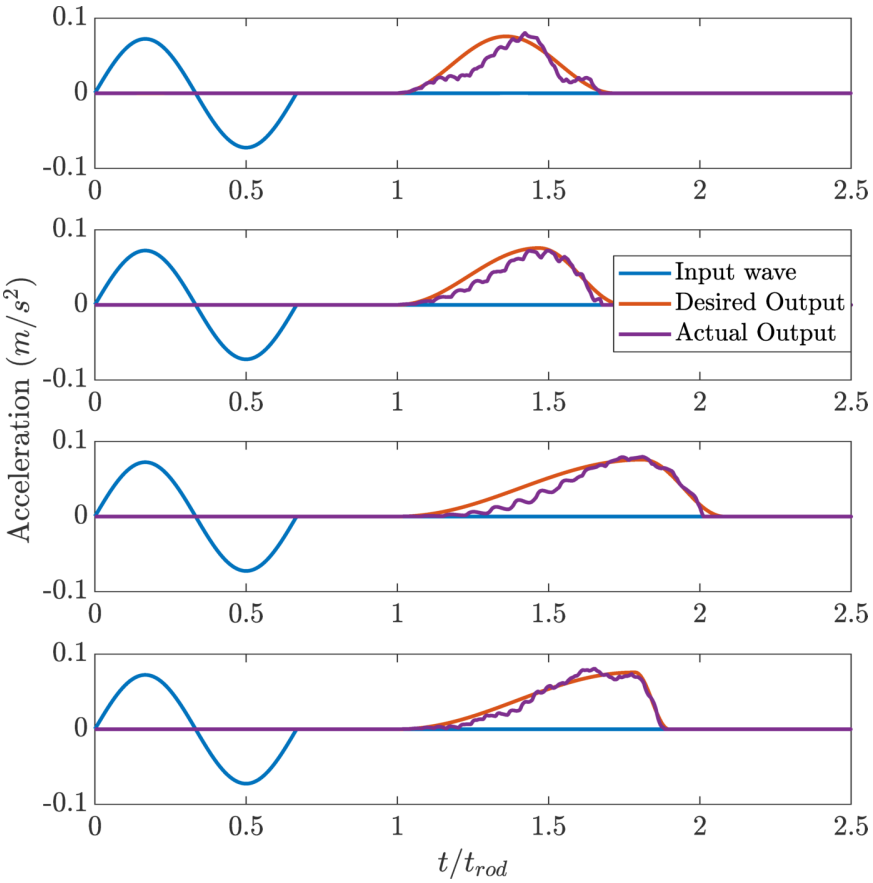

Figure 4.20: Optimized wave shapes for longer rightward facing ramp type desired outputs, with the first wave $t_1 = \tau, t_2 = \tau$, the second $t_1 = 5/4\tau, t_2 = 3/4\tau$, the third $t_1 = 3/2\tau, t_2 = 1/2\tau$, and the fourth $t_1 = 7/4\tau, t_2 = 1/4\tau$, all with $T_d = 0$ (no dwell) as defined in Fig. 4.2.

Table 4.3: Optimized parameter values for square type waves.

t_1, T_d, t_2	$r_m = \frac{m_r}{m_{rod}}$	$r_\omega = \frac{\omega_r}{\omega_0}$	$r_A = \frac{A_2}{A_1}$	$L_r = \frac{L_1}{L_1+L_2}$	$r_{L_{uc}} = \frac{L_1+L_2}{L_{i1}+L_{i2}}$	$E_{L_2} = \frac{\|a_o\|}{\|a_d\|}$
$\frac{1}{3}\tau, \frac{1}{3}\tau, \frac{1}{3}\tau$	0.124	1.219	0.473	0.357	1.332	0.994
$\frac{1}{4}\tau, \frac{1}{2}\tau, \frac{1}{4}\tau$	0.121	1.183	0.461	0.243	1.366	1.001
$\frac{1}{6}\tau, \frac{2}{3}\tau, \frac{1}{6}\tau$	0.123	1.142	0.459	0.173	1.470	0.969

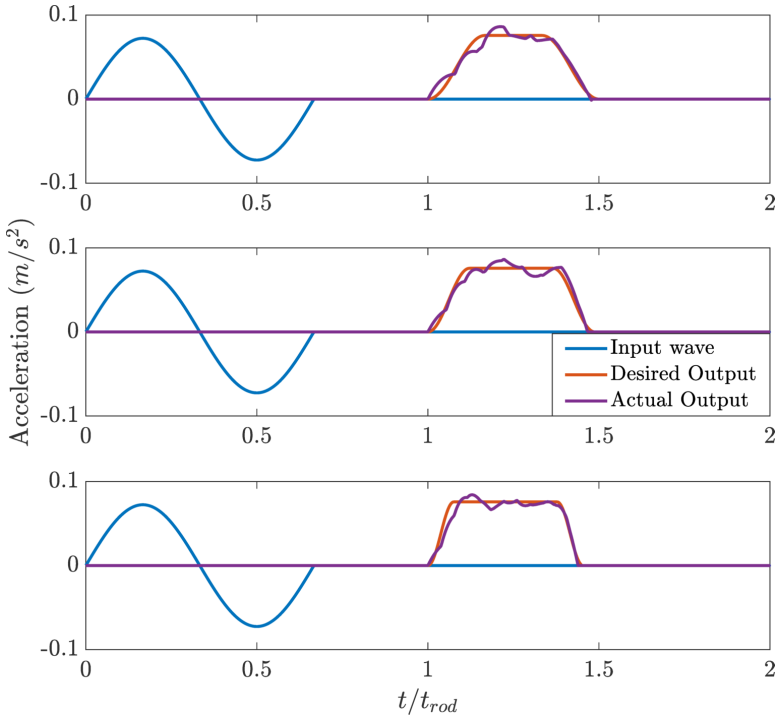

Figure 4.21: Optimized wave shapes for dwell type desired outputs with the top, middle, and bottom waves having $t_1 = 1/3\tau, T_d = 1/3\tau, t_2 = 1/3\tau$; $t_1 = 1/4\tau, T_d = 1/2\tau, t_2 = 1/4\tau$; and $t_1 = 1/6\tau, T_d = 2/3\tau, t_2 = 1/6\tau$ respectively, as defined in Fig. 4.2.

functions (in blue) lining up exactly with the predicted dispersion bandgaps.

4.5.3 Analytical Model Sensitivity Analysis

The pulse shaping technique was investigated for its sensitivity to variations in both material and geometric properties. Manufacturing processes introduce imperfections into structures which can cause them to perform differently than intended. Two properties, the Young's modulus, and the cross-sectional area, were perturbed to determine how changes in these parameters would affect the pulse shaping performance of the phononic material and its robustness when manufactured. In all simulations the Young's modulus was assumed to be uniform throughout the structure. However, the sensitivity of the pulse shaping technique to variation in the Young's modulus was chosen because this material property is known to vary based on a variety of factors that are difficult to control in manufacturing, and is a common variation. The cross-sectional area was chosen because it is the main

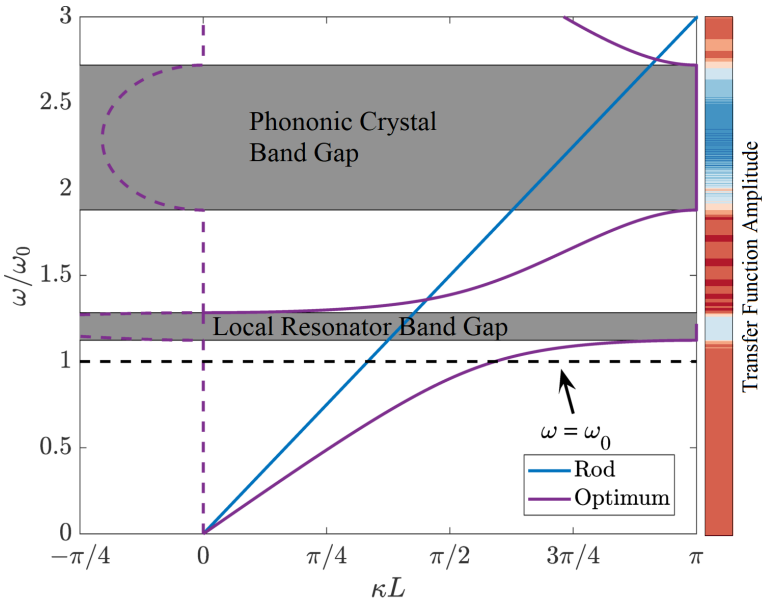

Figure 4.22: Dispersion diagram of the optimized unit cell for the $t_1 = 1/3\tau, T_d = 1/3\tau, t_2 = 1/3\tau$ dwell wave, bandgaps highlighted in gray and imaginary portion shown as a dashed line. The transfer function amplitude is shown on a log scale in the colorbar with highest values in dark red of approximately $\log_{10}(1.8)$ and lowest values in dark blue as approximately $\log_{10}(0.005)$.

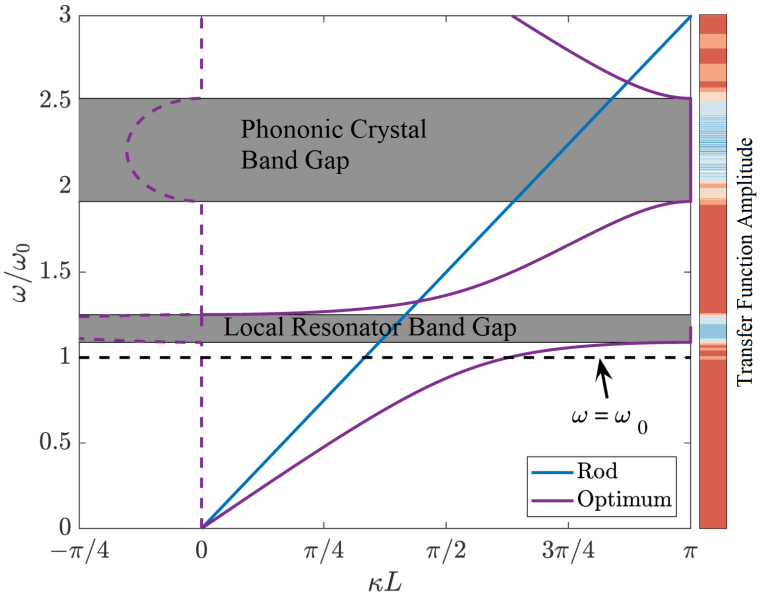

Figure 4.23: Dispersion diagram of the optimized unit cell for the $t_1 = 1/4\tau, T_d = 1/2\tau, t_2 = 1/4\tau$ dwell wave, bandgaps highlighted in gray and imaginary portion shown as a dashed line. The transfer function amplitude is shown on a log scale in the colorbar with the highest values in red as approximately $\log_{10}(1.5)$ and the lowest values in blue as approximately $\log_{10}(0.02)$.

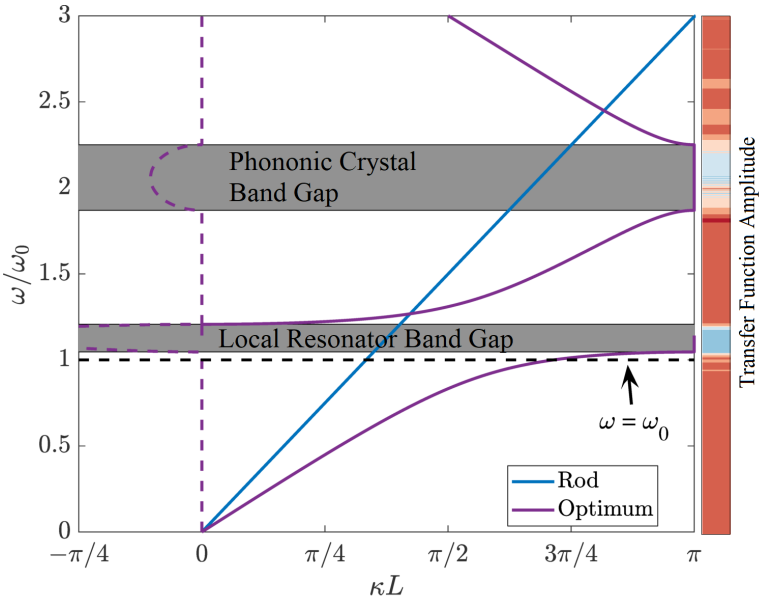

Figure 4.24: Dispersion diagram of the optimized unit cell for the $t_1 = 1/6\tau, T_d = 2/3\tau, t_2 = 1/6\tau$ dwell wave, bandgaps highlighted in gray and imaginary portion shown as a dashed line. The transfer function amplitude is shown on a log scale in the colorbar with red as approximately $\log_{10}(1.6)$ and the lowest values in blue as approximately $\log_{10}(0.03)$.

geometric feature used in introducing the phononic crystal.

In all previous simulations the phononic material unit cell shown in Fig. 4.10 was modeled combining the dynamic stiffness matrices for a rod with a resonator, given in Eq. 4.27, and an unmodified uniform rod, given in Eq. 4.22. The sensitivity to the Young's modulus was investigated by assuming that the first section, with the resonator, has a Young's modulus of E_1 and the second section has a Young's modulus of E_2. For the first section E_1 was held constant at the nominal values used for the previous simulations. For the second section a nominal 5% variation was introduced according to the relationship

$$E_2 = E_1(1 + 0.05x_r) \tag{4.48}$$

where

$$x_r = \sigma r. \tag{4.49}$$

The variable r is a random number drawn from a normal distribution with a mean of zero

and a standard deviation of 1. Using $\sigma = 3$ makes x_r a random number drawn from a distribution with standard deviation of 3. For r, 100 values were chosen, the Young's modulus E_2 was perturbed, and then the pulse shape for the $5/6\tau, 1/6\tau$ pulse using the optimized parameters given in Table 4.1 was calculated. A similar procedure for the cross-sectional area, but using the relationship

$$A_2 = r_A A_1(1 + 0.05x_r) \tag{4.50}$$

was followed. This results in a 5% variation with three standard deviations around the optimized cross-sectional area A_2.

The pulse shapes for the perturbed Young's modulus are shown in Fig. 4.25. Various models are shown in gray, with the two most extreme variations in pulse shape defining the inner and outer edges of this envelope of curves. This envelope of curves' boundaries correspond to $E_{min} = 0.49E_1$, shown in green, and $E_{max} = 1.39E_1$, shown in pink. These boundaries suggest that the output curves scale according to the size of the variation in Young's modulus. Even though a variation in Young's modulus by a factor as extreme as 0.5 or 1.39 would be extremely uncommon, a variation this large does not dramatically change the pulse shaping performance. For the majority of variations shown, the change in the output pulse shape would be inconsequential to the performance of the phononic material.

The pulse shapes for the perturbed cross-sectional area are shown in Fig. 4.26. Once again various models are shown in gray, with the two most extreme variations in area defining the inner and outer edges of the envelope of curves. For the cross-sectional area the boundaries of this envelope correspond to $A_{min} = 0.62A_2$ and $A_{max} = 1.47A_2$ given in green and pink, respectively. These results follow the same trends as the variation in Young's modulus, with smaller values of cross-sectional area resulting in lower rise time, and larger values resulting in higher rise times. These results suggest that the amount of

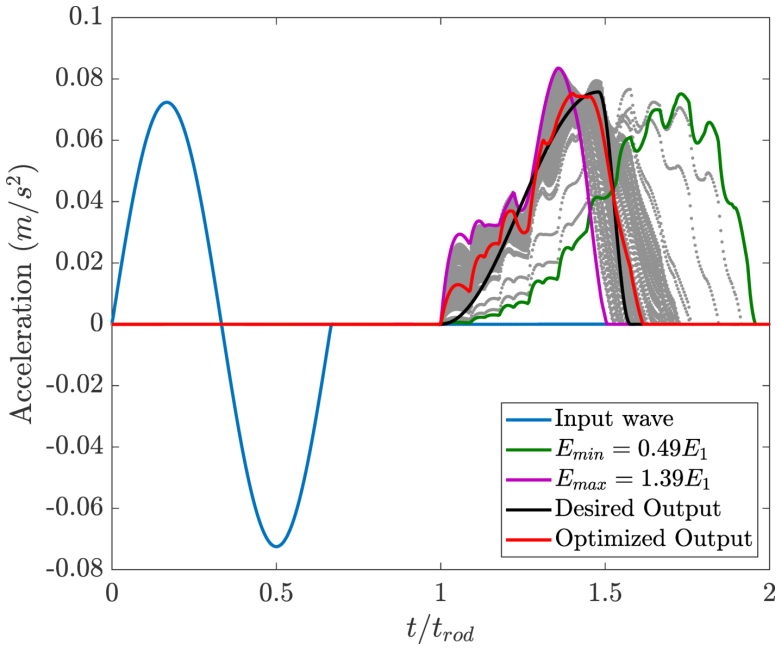

Figure 4.25: Sensitivity analysis for the pulse shaping technique, showing the effect of random variation in Young's Modulus on the pulse shape.

variation from the optimal curve would scale depending on the variation in cross-sectional area, and that for small variations there would be a negligible variation from the optimized curve.

The results of the sensitivity analysis show that the pulse shaping technique is relatively insensitive to variations in the Young's modulus or cross-sectional area. These results suggest that when implemented physically the phononic material would behave as expected, with minor but unimportant variations to the overall performance resulting from manufacturing defects.

4.5.4 FE Optimization

Physical Geometry

In order to perform optimization using FEA the combined unit cell shown in Fig. 4.10 was translated into a physically realizable geometry. The basic geometry used for the FE unit cell is shown in Fig. 4.27. The two different phases of the rod were modeled as coaxial

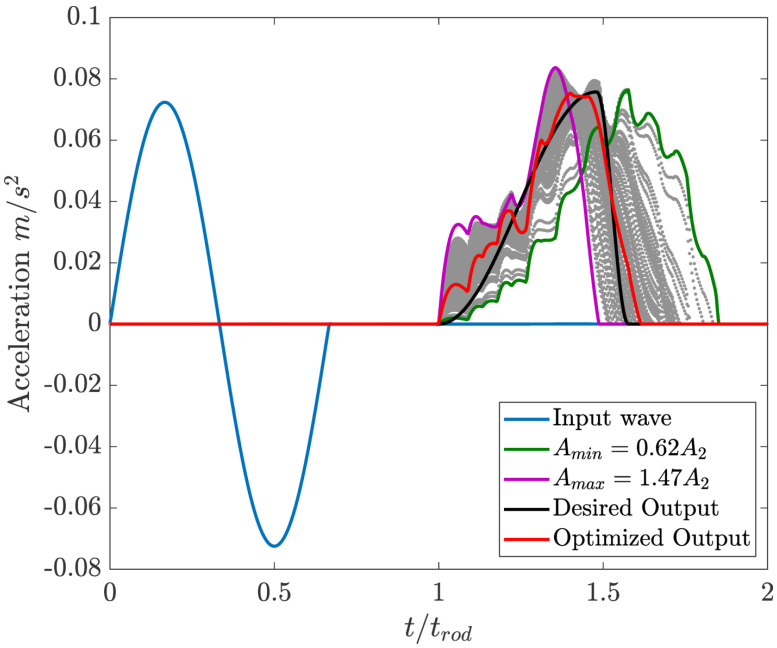

Figure 4.26: Sensitivity analysis for the pulse shaping technique, showing the effect of random variation in area on the pulse shape.

cylinders with different cross-sectional radii r_1 and r_2 to control the relative cross-sectional areas A_1 and A_2, and different lengths L_1 and L_2 to control the relative phase lengths. The mass of the resonator translated into a concentric ring around the second phase of the phononic crystal connecting to the terminating end of the first phase of the phononic crystal via supports which also act as springs. The resonator mass and spring geometry were designed to result in a vibration mode with motion along the axis of the rod (the direction of wave propagation). As a nominal starting value the natural frequency of this mode was tuned to $0.92\omega_0$. Although this geometry is not stiff enough to prevent other mode shapes near ω_0 from arising, all other modes near the frequency range of interest require out of plane or shearing motion to be excited. Because the rod will be excited by an axial impact, these motions will be minimal, therefore the other modes will have a negligible effect on the wave shape and their influence can be ignored.

The FE rod geometry is shown in Fig. 4.28. Assuming a minimum of 6 unit cells per wavelength, the minimum wavelength the mesh could capture was calculated. The mesh size accurately captures wave propagation for frequencies up to $1.91\omega_0$, capturing

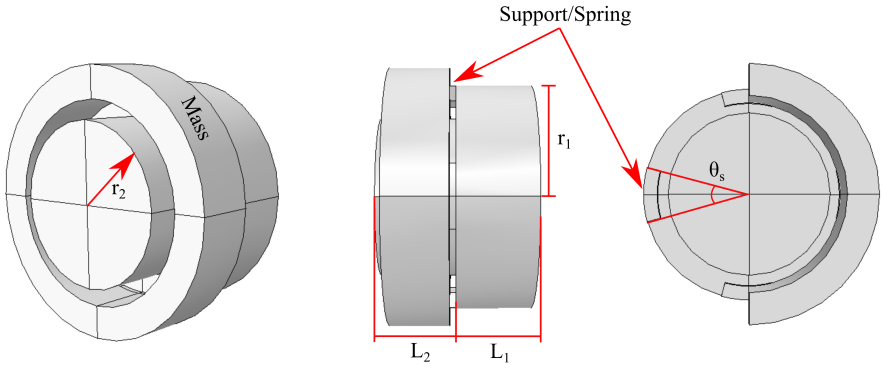

Figure 4.27: Various views of the unit cell geometry created from simplified combined unit cell shown in Fig. 4.10, with the far right view showing a cut-away view of a spring.

the main frequency content of the impact, while also allowing for reasonable runtime of the optimization routine. Mesh convergence studies showed that there was no significant difference between the output wave shape with this mesh density and higher mesh densities.

In the FE optimization, for the phononic crystal the same variables were used for optimization, namely the cross-sectional area, the relative lengths of the phases, and the total length of the unit cell. For the resonator, in the simplified model the mass and natural frequency were optimized. However, for the FE model these characteristics are functions of the size of the mass and the length and cross-section of the spring. As a result, geometric quantities which result in a change to the mass or spring stiffness were optimized as substitutes. The mass was controlled by optimizing $r_{m_{outer}}$, its outer radius. The spring stiffness was controlled by optimizing its width, controlled by the angle θ_s that the spring sweeps through. The mass was easy to calculate, therefore the optimized mass ratio $r_m = m_r/m_b$ comparing the resonator mass to the bar mass will still be reported as before. There are four supports, composed of cylindrical sectors with a fixed thickness and length. If each support sweeps through an angle of 45^o they combine into a single solid support. For modeling purposes the maximum angle is constrained to 44^o to maintain clearance between the springs. The ratio $r_\theta = \theta_s/44$ will be reported to reflect this, instead of the natural frequency. Although the angle the supports sweep through affects the natural frequency of

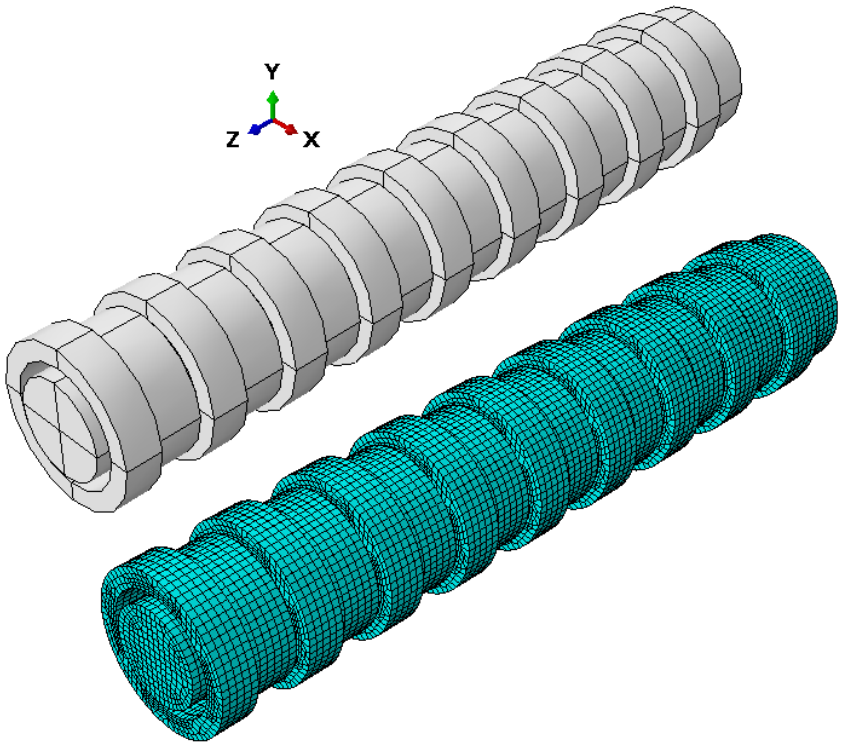

Figure 4.28: Nominal FE rod geometry composed of 9 unit cells as shown in Fig. 4.27 with wave propagation in the z-direction.

the resonator, it does not scale in exactly the same way as the mass on a spring does. Some stiffness from the rod also contributes. As a result it is easier to report the optimized angle swept through by the support than the natural frequency. As a general rule, the larger the support angle, the higher the natural frequency.

The extension of the geometry resulted in geometric constraints to provide clearance between the resonator and the other parts of the unit cell. These constraints, and their justification are as follows:

1. $r_{m_{outer}} \geq r_1$ sets a minimum value of $m_r \approx 0.1$ and prevents the mass width from being smaller than the spring width, which would cause problems with meshing the parametric model.

2. $44 \geq \theta_k \geq 1$ prevents interference between the different springs, but also prevents the springs from having zero spring stiffness, which will cause errors in the FE code.

Table 4.4: Optimized parameter values for ramp type waves using an FE model.

t_1, t_2	$r_m = \frac{m_r}{m_{rod}}$	$r_\theta = \frac{\theta_s}{44}$	$r_A = \frac{A_2}{A_1}$	$L_r = \frac{L_1}{L_1+L_2}$	$r_{L_{uc}} = \frac{L_1+L_2}{L_{i1}+L_{i2}}$	$E_{L_2} = \frac{\|a_o\|}{\|a_d\|}$
$\frac{5}{6}\tau$, $\frac{1}{6}\tau$	0.048	0.599	0.515	0.525	0.971	0.901
$\frac{1}{2}\tau$, $\frac{1}{2}\tau$	0.049	0.371	0.622	0.679	1.437	0.987
$\frac{1}{6}\tau$, $\frac{5}{6}\tau$	0.023	0.437	0.700	0.069	2.150	1.026

3. $0.7 \geq r_A \geq 0.05$ The lower bound allows for a very small but non-zero cross-sectional area. The upper bound prevents interference between the second phase of the phononic crystal and the resonator.

4. $L_2 \geq 1.05L_m$ where L_m is the combined length of the mass and support spring. The second phase length of the phononic crystal must be longer than L_m or else the resonator will interfere with the subsequent unit cell.

The FE model was implemented using the Abaqus Python API. It was optimized using the Nelder-Mead simplex algorithm available in the Python scipy module.

FEA Optimization Results

Results for the FEA optimized ramp type waves are shown in Fig. 4.29. The optimized values are shown in Table 4.4 and the optimized geometries in Fig. 4.30. The optimized metamaterial was able to successfully achieve both a symmetric and rightward ramp, but struggled to achieve a leftward ramp. Although the E_{L2} error measurement was closer for the leftward $1/6\tau, 5/6\tau$ than the rightward $5/6\tau, 1/6\tau$ waves, qualitatively it can be seen from Fig. 4.29 that the leftward desired ramp was not achieved, while the rightward ramp matched the desired wave shape almost exactly except for the peak of the wave. These results are similar to what the simple analytical model predicted in Sec. 4.5.2.

In Table 4.4 there are two clear trends. As the wave shape shifts from right to left, the total unit cell length ratio $r_{L_{uc}}$ increases, and the cross-sectional area ratio r_A increases. This indicates that decreasing the total length and the cross sectional area A_2 contribute to

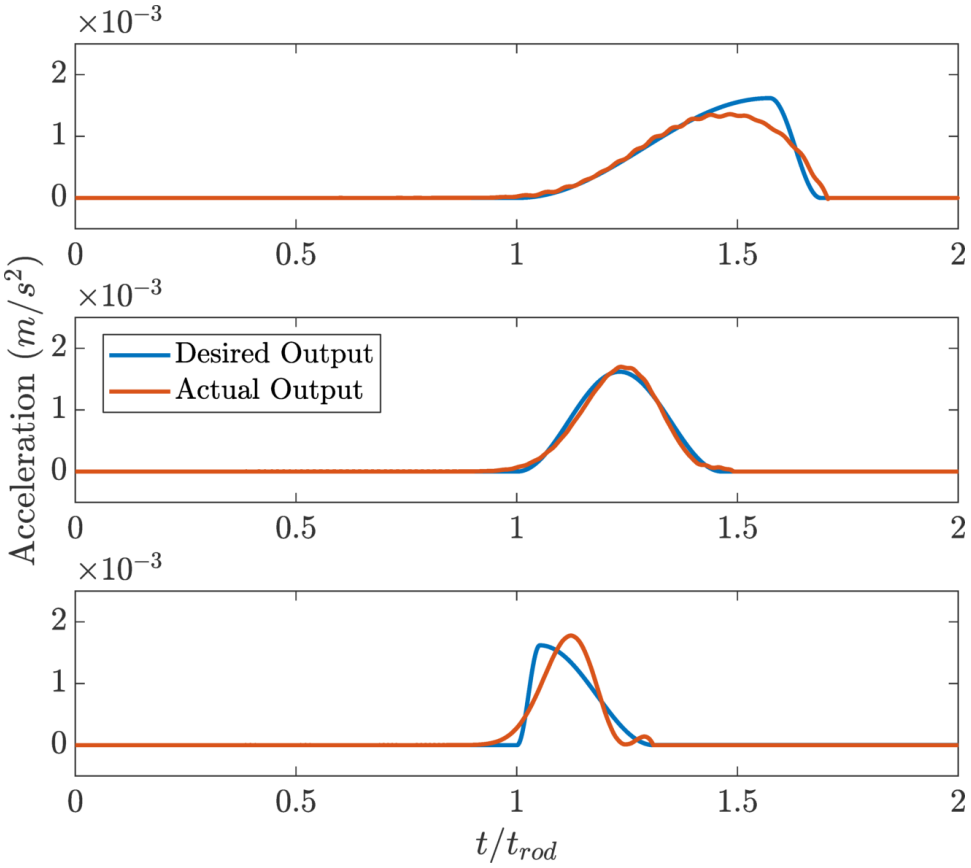

Figure 4.29: Optimized wave shapes produced by FE models for rightward facing ramp type desired outputs for waves (from top to bottom) $t_1 = 5/6\tau, t_2 = 1/6\tau$; $t_1 = 1/2\tau, t_2 = 1/2\tau$; and $t_1 = 1/6\tau, t_2 = 5/6\tau$.

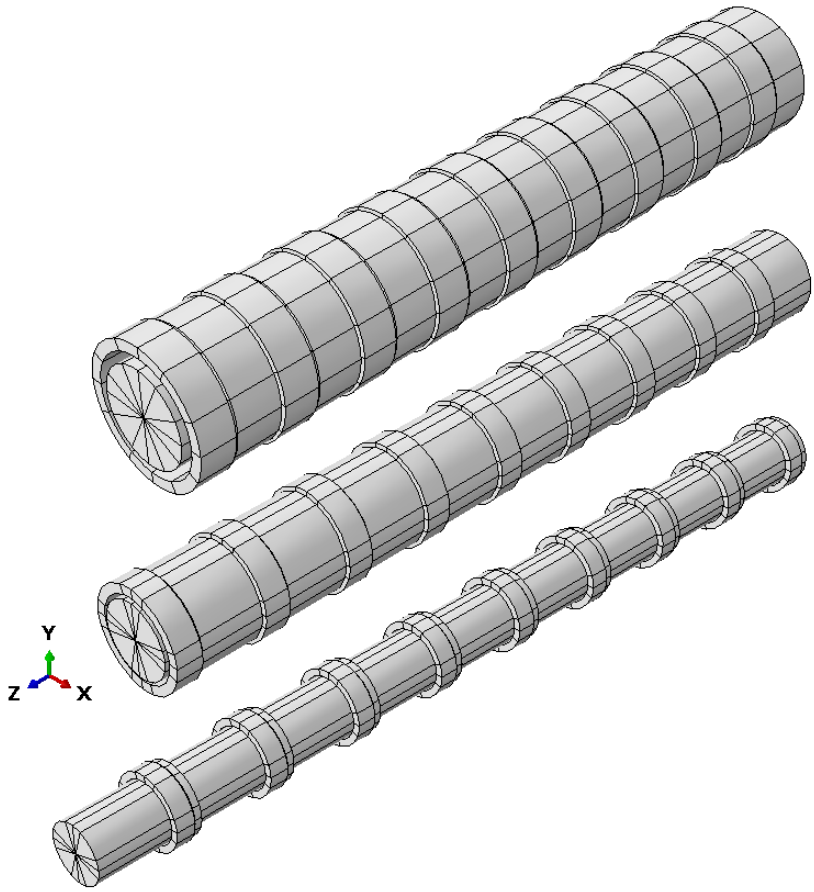

Figure 4.30: Optimized geometries for, from top to bottom, the $t_1 = 5/6\tau, t_2 = 1/6\tau$; $t_1 = 1/2\tau, t_2 = 1/2\tau$; and $t_1 = 1/6\tau, t_2 = 5/6\tau$ ramp type waves.

shifting the wave to the right.

In addition to the three different ramps presented in Fig. 4.29, four longer rightward facing ramps were investigated. The results for these ramps are shown in Fig. 4.31 with the optimized parameters given in Table 4.5 and optimized geometries shown in Fig. 4.32. The optimized waves follow the same trends as predicted by the optimization of the simplified analytical model. The optimized $t_1 = \tau, t_2 = \tau$ and $t_1 = 5/4\tau, t_2 = 3/4\tau$ waves did not match the desired wave shape as closely as the two wave shapes that were slanted further right. The only clear trend in the optimized parameters was that r_θ became progressively smaller, meaning softer springs and therefore a lower natural frequency for the resonator. This, also coupled with a low mass of the resonator, suggests that the resonator does not

Table 4.5: Optimized parameter values for longer ramp type waves using an FE model.

t_1, t_2	$r_m = \frac{m_r}{m_{rod}}$	$r_\theta = \frac{\theta_s}{44}$	$r_A = \frac{A_2}{A_1}$	$L_r = \frac{L_1}{L_1+L_2}$	$r_{L_{uc}} = \frac{L_1+L_2}{L_{i1}+L_{i2}}$	$E_{L_2} = \frac{\|a_o\|}{\|a_d\|}$
τ, τ	0.200	0.467	0.345	0.548	1.344	0.882
$\frac{5}{4}\tau$, $\frac{3}{4}\tau$	0.250	0.442	0.320	0.435	1.254	0.881
$\frac{3}{2}\tau$, $\frac{1}{2}\tau$	0.019	0.133	0.255	0.467	1.484	0.987
$\frac{7}{4}\tau$, $\frac{1}{4}\tau$	0.029	0.126	0.213	0.330	1.484	1.066

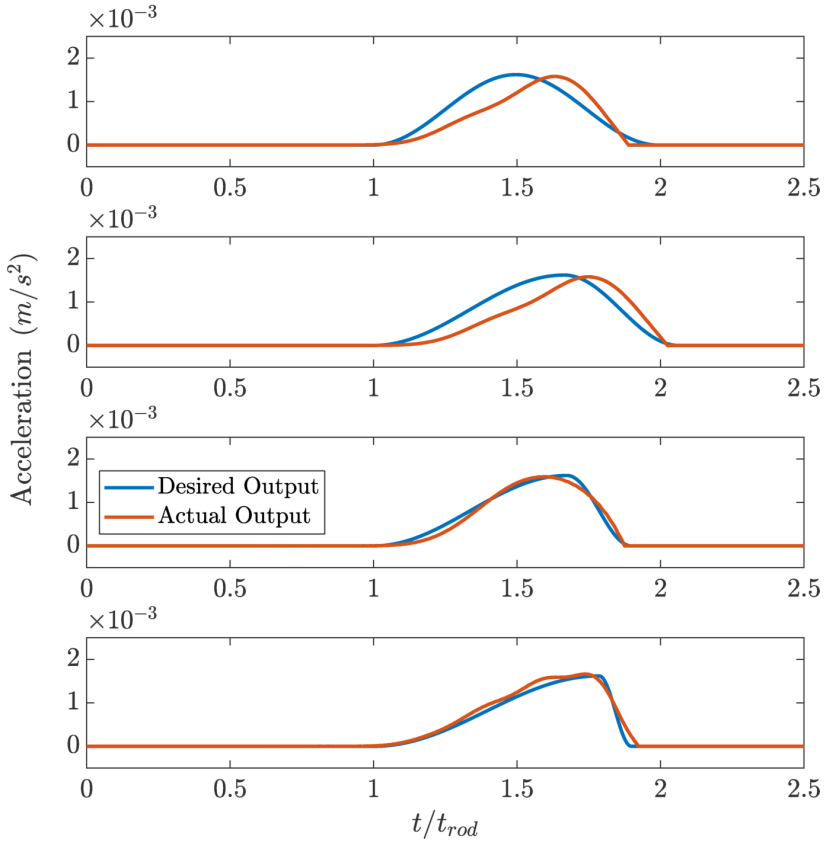

Figure 4.31: Optimized wave shapes for, from top to bottom, the $t_1 = \tau, t_2 = \tau$; $t_1 = 5/4\tau, t_2 = 3/4\tau$; $t_1 = 3/2\tau, t_2 = 1/2\tau$; and $t_1 = 7/4\tau, t_2 = 1/4\tau$ ramp type waves.

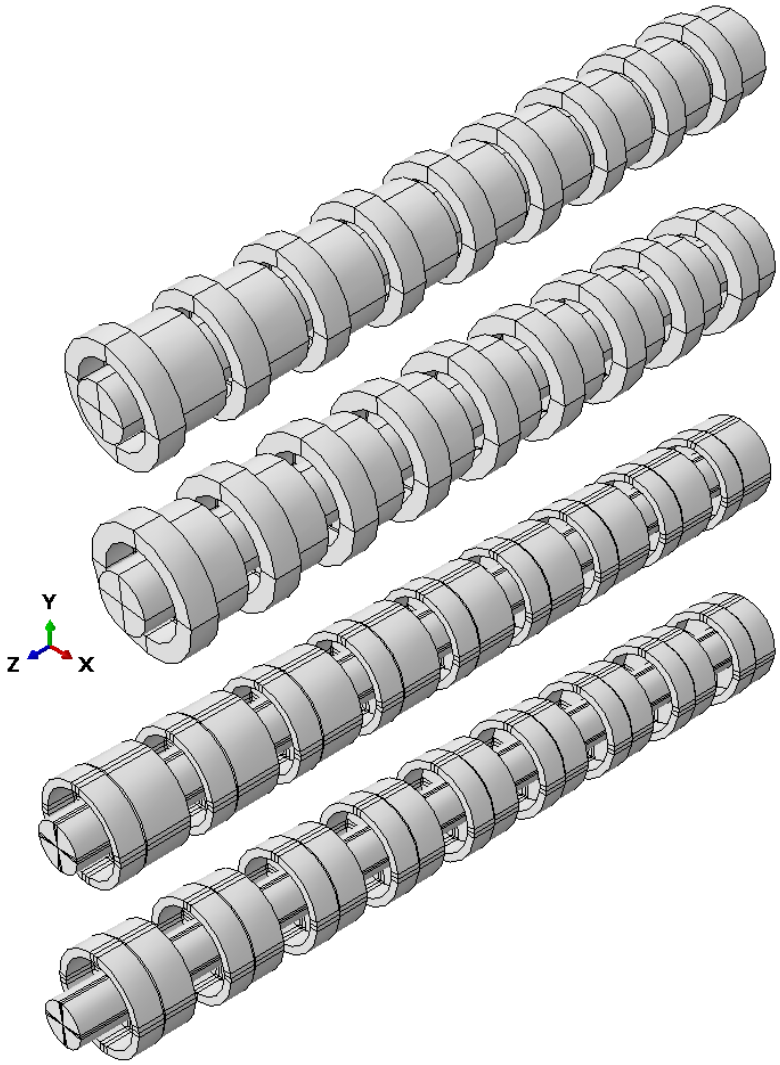

Figure 4.32: Optimized geometries for, from top to bottom, the $t_1 = \tau, t_2 = \tau$; $t_1 = 5/4\tau, t_2 = 3/4\tau$; $t_1 = 3/2\tau, t_2 = 1/2\tau$; and $t_1 = 7/4\tau, t_2 = 1/4\tau$ ramp type waves.

Table 4.6: Optimized parameter values for dwell type waves using a FE model.

t_1, T_d, t_2	$r_m = \frac{m_r}{m_{rod}}$	$r_\theta = \frac{\theta_s}{44}$	$r_A = \frac{A_2}{A_1}$	$L_r = \frac{L_1}{L_1+L_2}$	$r_{L_{uc}} = \frac{L_1+L_2}{L_{i1}+L_{i2}}$	$E_{L_2} = \frac{\|a_o\|}{\|a_d\|}$
$\frac{1}{3}\tau, \frac{1}{3}\tau, \frac{1}{3}\tau$	0.075	0.459	0.657	0.707	1.585	1.111
$\frac{1}{4}\tau, \frac{1}{2}\tau, \frac{1}{4}\tau$	0.115	0.520	0.680	0.549	1.131	1.125
$\frac{1}{6}\tau, \frac{2}{3}\tau, \frac{1}{6}\tau$	0.240	0.578	0.700	0.297	0.756	0.927

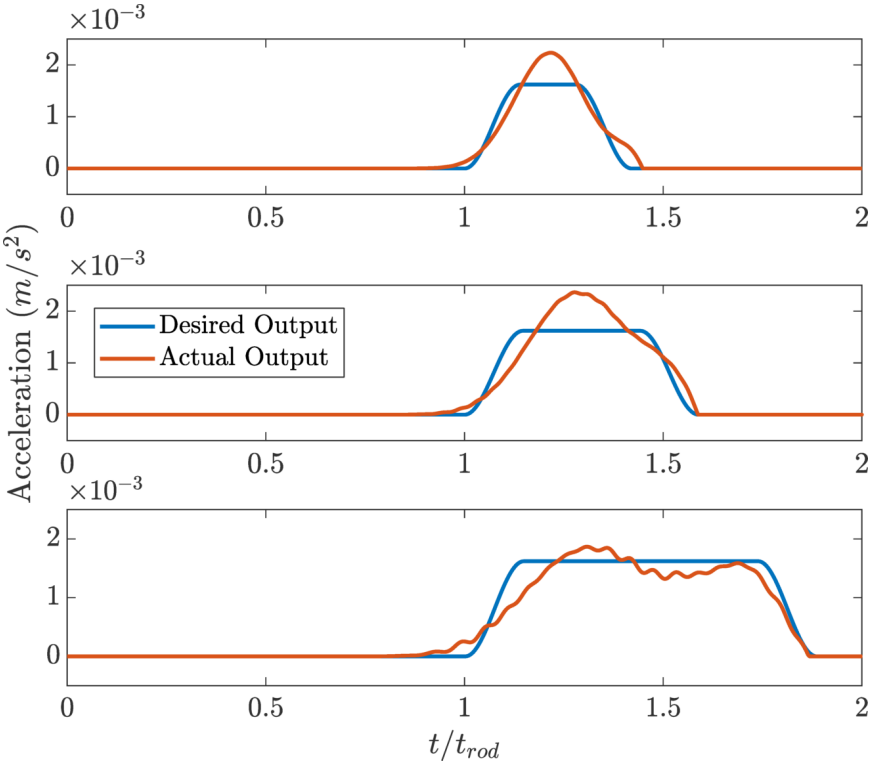

Figure 4.33: Optimized wave shapes for, from top to bottom $t_1 = 1/3\tau, T_d = 1/3\tau, t_2 = 1/3\tau$; $t_1 = 1/4\tau, T_d = 1/2\tau, t_2 = 1/4\tau$; $t_1 = 1/6\tau, T_d = 2/3\tau, t_2 = 1/6\tau$ dwell type waves.

play a large role in obtaining this particular wave shape. It is instead controlled by the tuning of the phononic crystal parameters.

Results for the FEA optimized dwell type waves are shown in Fig. 4.33. The optimized parameters are shown in Table 4.6 and the optimized geometries are shown in Fig. 4.34. The E_{L2} error measurements show that the metamaterial was able to successfully shape dwell type waves. However, the analytical model optimization predicted flatter regions in the dwell section, something which the FEA optimization routine struggled to achieve, with

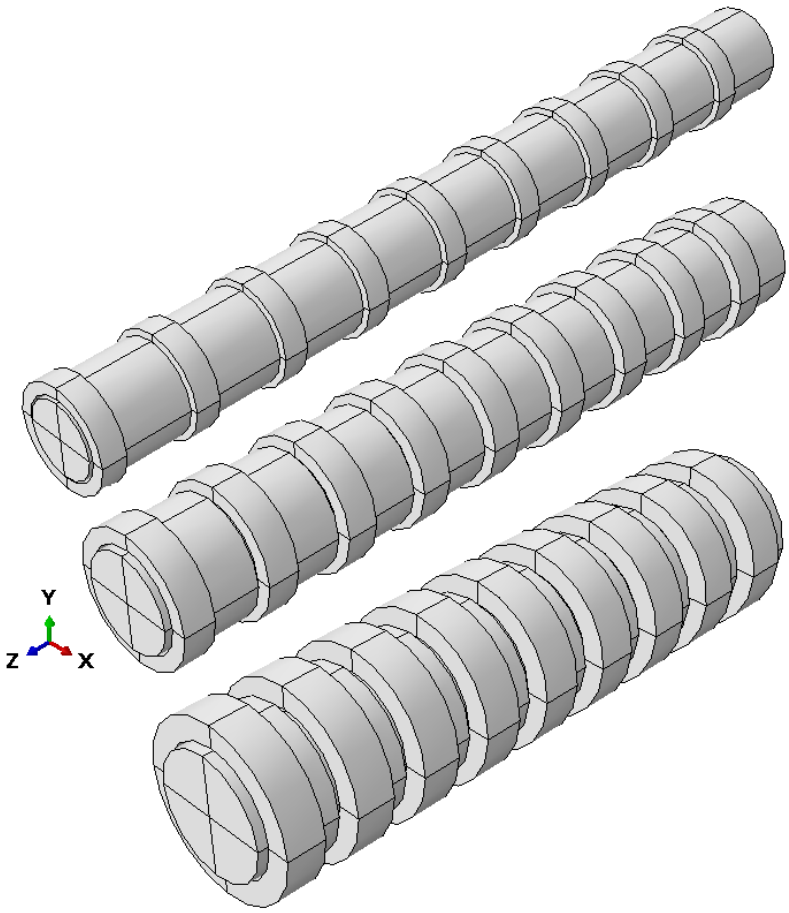

Figure 4.34: Optimized geometries for, from top to bottom $t_1 = 1/3\tau, T_d = 1/3\tau, t_2 = 1/3\tau$; $t_1 = 1/4\tau, T_d = 1/2\tau, t_2 = 1/4\tau$; $t_1 = 1/6\tau, T_d = 2/3\tau, t_2 = 1/6\tau$ dwell type waves.

the best approximation of this in the longest dwell case. The optimized values show that as the dwell became longer and the rise times shorter, the mass of the resonator increased. Also, the length of each unit cell decreased and the phase ratio became smaller, shifting from a longer first phase to a longer second phase.

4.6 Conclusion

In this chapter a technique to shape pulses in 1D elastic waveguides was developed. The input wave was specified as a haversine, and a general equation that could specify both ramps and dwells as outputs was created, allowing for the creation of the desired output

pulse shape. The elastic bar was modeled analytically using the dynamic stiffness and transfer matrices. Parametric studies showed that no individual parameter of the phononic materials allowed for precise enough control to achieve the possible desired output wave shapes. Instead, the use of an optimization routine showed that by tuning the various parameters, ramp and square type waves could be produced using an analytical model to match the desired wave shapes. A sensitivity analysis of the optimized analytical model showed that the pulse shape is relatively insensitive to perturbations in both material and optimized geometric properties.

Finally, the analytical model was translated into an FE model. The change in cross-sectional area of the rods implemented the phononic crystal, the resonator mass translated into a collar, and the springs translated into supports connecting the collar to the rod. The FE model was parametrized and subjected to geometric constraints which the analytical model was not subject to. When the parametrized FE models were optimized for the same desired pulse shapes as the analytical models, physically realizable geometry was found that creates reasonable approximations of the desired pulses.

The results of this chapter demonstrate that phononic materials can be used to shape pulses traveling in 1D waveguides. This is a novel use of phononic materials which has not been demonstrated before. This chapter also shows that complex phononic materials are not needed to do this. Instead this was demonstrated using a set of simple phononic crystal and elastic metamaterial concepts. By combining and optimizing the effects of the two simple phononic materials, physically realizable geometry was produced which resulted in pulse shaping.

CHAPTER 5
CONCLUSIONS AND CONTRIBUTIONS

5.1 Summary

To date, elastic metamaterials have found limited success in practical applications. The overarching goal of this dissertation is to explore potential practical problems where elastic metamaterial concepts could be successfully applied. To this end, three wave propagation or vibration problems have been investigated. These problems include vibration mitigation for a massive vibrating industrial machine, i.e. an electric generator; the bouncing of electrodes in a circuit breaker during a closing event and how to reduce the accompanying arc time; and pulse shaping in Hopkinson bar tests.

For the vibration mitigation of the electric generator two different concepts were explored. These included spring mass resonators mounted to the generator, tuned to resonate at its excitation frequency. Applying these resonators to the generator resulted in a reduced force experienced at the base of the supports, where the generator attached to ground. The other concept consisted of periodically applied grounding springs which create a mechanical high pass filter. The stiffness of these springs were tuned to place the generator excitation frequency within the stop band. This concept resulted in a reduction of the force experienced along the main support of the structure, although the total force through all of the grounding springs remained the same. Results of this study highlight some of the difficulties in applying elastic metamaterial concepts to vibration mitigation of heavy machinery.

For the circuit breaker electrode bouncing problem each electrode was modeled as a continuous system with waves propagating through it. When the electrodes were in contact they were modeled as a single system, and when they were out of contact as two separate

systems. Contact was initiated when the electrode contact tips' displacement matched, and was broken when a tension wave reached the contact interface. The result is that although each electrode was modeled as a linear system, the combined system was highly nonlinear. Both analytical and numerical approaches were used to find solutions to the system model. The results showed that the electrode bounce duration was dependent on several parameters, including the wave speed in the electrodes, the length of the electrodes, and the stiffness of the electrode base spring. The results suggested that if the wave duration from impact could be modified by changing the slope of the stress wave as it propagates through the system then the bounce time could be reduced. One suggested way to do this was by modifying the wave shape via elastic metamaterials.

The Hopkinson bar test and electrode bouncing problem are similar in that both systems have individual waves propagating through the system, and both could benefit from control of the shape of those waves. As a result, the pulse shaping suggested by the bouncing electrode problem was explored more fully in the Hopkinson bar problem. For the Hopkinson bar the input pulse shape was known and the desired output pulse shape was chosen. The research investigated what phononic crystal and metamaterial characteristics were necessary to achieve the desired pulse shape. Four metamaterial concepts were investigated, including phononic crystals, local resonators, grounding springs, and cross-sectional variation. The investigation found that a combined unit cell composed of a phononic crystal and local resonator had the greatest potential for wave shaping. An optimization routine applied to the analytical model demonstrated that the proposed unit cell could perform pulse shaping and was relatively insensitive to defects, and an optimization routine applied to an FE model found the necessary geometry to achieve this. Two different classes of waves, dwell shaped waves and ramp shaped waves were successfully achieved using the FE optimization routine.

5.2 Challenges and Constraints in the Practical Application of Elastic Metamaterials

As was stated in Sec. 5.1 the goal of this research was to explore the potential practical application of elastic metamaterials. This effort has run into several constraints which add additional complexity to the application of elastic metamaterials. There is a fundamental tradeoff between the important quantities of the bandgap frequency and length of phononic crystals; stiffness and mass of local resonators; and mass and geometric extension of local resonators. These constraints are reviewed and summarized here.

The tradeoff between frequency and length is well known. Phononic crystals introduce bandgaps into structures via the use of material or geometric periodicity. This periodicity results in bandgaps for frequencies with wavelengths close to the characteristic length of the periodicity. For example, Fig. 4.22 shows a bandgap that starts at $\omega/\omega_0 \approx 1.9$. In this case the wave length is approximately 2.4 times the length of a unit cell. In designing phononic crystals, as the desired frequency for the bandgap becomes lower the wave length becomes longer, requiring a longer unit cell size. As a result, the length scales needed to create bandgaps at low frequencies become prohibitive for many possible uses.

Local resonators offer the ability to avoid the geometric size problem. The local resonators create what has been termed subwavelength bandgaps, i.e. bandgaps that appear at frequencies lower than would appear due to the periodicity of the structure. These bandgaps appear at the resonant frequency of the resonator. There is also a fundamental limitation with mass and stiffness that creates difficulty in applying local resonators for vibration isolation of large structures. This can be seen by the resonant frequency for a mass-spring resonator, of

$$\omega_r = \sqrt{\frac{k}{m}} \tag{5.1}$$

where k is the stiffness and m is the mass. To keep a constant resonant frequency, if the stiffness goes up, the mass also must increase. This became a limiting factor for the

generator in Ch. 2. It prevented the supports from being modified into a monatomic lattice, as described in [31], because they also needed to be stiff to enough support the static weight of the generator. The high static stiffness required a prohibitively high mass to create an elastic metamaterial with a bandgap that included the excitation frequency of interest.

Finally, when developing the physical implementation of local resonators, there is a limitation in mass and geometric extension when trying to apply internal resonators as described in [31]. Again in the case of the generator, because the mass the supports were holding was very large, even though the resonators could be effective at a small fraction of the total mass, the amount of space needed for the masses was still too large for them to fit within the space the support provided. Thus even though a potentially effective vibration mitigation technique, its application was limited by the conflicting requirements of the mass and its geometric extension.

These limitations provide a suggestion for the kinds of problems in which elastic metamaterials would be able to be effectively applied for vibration mitigation techniques. For large scales or high frequencies phononic crystals might be sufficient. On smaller scales or lower frequencies the local resonator would be a more appropriate choice. But the local resonator also will be limited by the amount of kinetic energy inherent in the system, necessary stiffness, and space for mass. These tradeoffs suggest that applied problems that require lower stiffness or with the excitation frequency appearing at higher frequencies would be better targets for the successful use of elastic metamaterials. A good example of this kind of problem is the use of phononic crystals and elastic metamaterials for pulse shaping in Ch. 4. The input pulse resulted in a frequency spectrum which was sufficiently high enough for phononic crystals to be used and where less massive resonators could be effective.

5.3 Research Contributions

The research contributions of this work are as follows:

1. The application of elastic metamaterials to heavy industrial equipment was explored, and a couple of possible concepts were demonstrated.

2. A new analytical model for the bouncing of circuit breaker electrodes after closing was proposed. Prior work on this subject has modeled the electrodes numerically or else treated the electrodes as lumped element systems. These models were not used to examine wave propagation in the electrodes. The new model naturally lends itself to an understanding of the role wave propagation plays in electrode bouncing and provides analytical solutions that show how various aspects of the electrode affects the wave propagation and the electrode bounce.

3. A technique to shape pulses in 1D rods using phononic materials was developed and refined. Phononic materials have not previously been used to perform pulse shaping in elastic waveguides.

4. The geometry and implementation for the pulse shaping technique was demonstrated in a physically realizable structure.

5.4 Recommendations for Future Work

5.4.1 Hopkinson Pressure Bar

There are two immediate developments which would be valuable for the pulse shaping techniques described in Ch. 4. The first is to experimentally validate the pulse shaping technique to show that the optimized elastic metamaterials developed behave as predicted. The second is to develop the same technique to be used for shaping stress, strain, or velocity quantities. Although this dissertation has focused on acceleration, many split Hopkinson bar tests focus on stress and strain [66, 67]. Thus these would be valuable additions to the pulse shaping technique.

Additionally, split Hopkinson pressure bar tests have been developed for both tension waves [68] and torsional waves [69]. The work in Ch. 4 assumed a compression test. How-

ever, a tensile wave would be expected to travel in the same manner through the system. Thus, with minimum development pulse shaping could be adapted for tensile waves. In torsional split Hopkinson bar tests square type waves [70] are important. Torsional wave propagation and longitudinal wave propagation in bars are modeled using the same governing equations [71]. Thus a similar analysis to that in Ch. 4 could be used to develop pulse shaping in torsional bars, with optimization to develop torsional metamaterials and geometry for actual use.

5.4.2 Electrode Bouncing

In Ch. 3 a new analytical model was proposed for the bouncing of circuit breaker electrodes that was able to predict bounce time and duration based on the waves traveling through the system. For the electrode bouncing problem recommended future work focuses on three specific areas. The first is to use the analytical model to further explore the effect of base spring stiffness on bounce duration. This would be accomplished by assuming that the wave speeds of the electrodes are the same, and that the electrode lengths nominally satisfy the relationship $L_1 = 2L_2$, and then modifying the spring stiffness to see how it affects the propagating waves and the resulting bounce duration. The second recommendation is to develop a finite difference model that implements a WENO scheme, to make the numerical solutions more effectively model the discontinuities present in the bouncing bar phenomenon. It is expected that this would make the numerical solution more robust, and less subject to noise. The third recommendation comes from the pulse shaping developed for the Hopkinson bar test demonstrated in Ch. 4. Using the analytical models for electrode bouncing, the pulse shaping and optimization techniques could be applied to develop a metamaterial that shapes the wave caused by electrode impact to reduce the time of bounce for the electrode. This has not been explored in this dissertation and would be another interesting application of pulse shaping.

5.4.3 Dispersion Optimization

In Ch. 4 pulse shaping was accomplished by defining an objective function in the time domain that measured the error between an actual and desired output wave shape. If the input and output pulse shape are known, then an inverse problem can be formulated to determine the necessary dispersion relationship for the material the wave would pass through, to cause it to transform into the desired output wave. A metamaterial could be optimized using an objective function that calculated the error between the desired dispersion relationship and the actual dispersion relationship. By doing this the dispersion relationship could be approximated with an elastic metamaterial.

5.4.4 Pulse Shaping Using Variable Cross-Section

In Sec. 4.4 the effect of an exponentially varying cross-section on pulse shape was investigated. This is a very specific case of a class of rods with wide variability. As Sec. 4.4 showed, a varying rod cross-section changes the shape of a pulse traveling through it. Varying the rod cross-section could be used to obtained desired output wave shapes. The governing equation for a rod with unspecified cross-section is

$$\frac{1}{A(x)}\frac{\partial}{\partial x}\left(A(x)\frac{\partial u}{\partial x}\right) = \frac{1}{c_0^2}\frac{\partial^2 u}{\partial t^2}. \tag{5.2}$$

In this equation, more general solutions have been found assuming that the cross section is given by both a polynomial [72] or sinusoidal expansion[73]. Even if analytical solutions are not available for a specified cross-section, so long as the equation remains numerically solvable this would be a sufficient model for pulse shaping. The coefficients in the cross-sectional area polynomial or Fourier series could be treated as variables to be optimized to cause an output pulse shape to match a desired output pulse shape. This could provide an additional optimization technique for the shaping of pulses.

REFERENCES

[1] D. Mead, "A general theory of harmonic wave propagation in linear periodic systems with multiple coupling," *Journal of Sound and Vibration*, vol. 27, pp. 235 –260, 2 1973.

[2] M. Heckl, "Investigations on the vibrations of grillages and other simple beam structures," *J. Acoust. Soc. Am.*, vol. 36, 7 1964.

[3] Z. Liu, X. Zhang, Y. Mao, Y. Zhu, Z. Yang, C. T. Chan, and P. Sheng, "Locally resonant sonic materials," *Science*, vol. 289, 2000.

[4] H. Sun, X. Du, and P. F. Pai, "Theory of metamaterial beams for broadband vibration absorption," *Journal of Intelligent Material Systems and Structures*, vol. 21, pp. 1085 –1101, 11 2010.

[5] D. Yu, Y. Liu, H. Zhao, G. Wang, and J. Qiu, "Flexural vibration band gaps in Euler-Bernoulli beams with locally resonant structures with two degrees of freedom," *Phys. Rev. B*, vol. 73, pp. 064 301–1 –064301–5, 2006.

[6] G. Wang, X. Wen, J. Wen, and Y. Liu, "Quasi one-dimensional periodic structure with locally resonant band gap," *Journal of Applied Mechanics*, vol. 73, 2006.

[7] X. Wang and M. Wang, "An analysis of flexural wave band gaps of locally resonant beams with continuum beam resonators," *Meccanica*, vol. 51, 2016.

[8] Y. Xiao, J. Wen, D. Yu, and X. Wen, "Flexural wave propagation in beams with periodically attached vibration absorbers: Band-gap behavior and band formation mechanisms," *J. Sound Vib.*, vol. 332, pp. 867 –893, 2013.

[9] B. Sharma and C. Sun, "Local resonance and Bragg bandgaps in sandwich beams containing periodically inserted resonators," *J. Sound Vib.*, vol. 364, 2016.

[10] D. Beli, J. Arruda, and M. Ruzzene, "Wave propagation in elastic metamaterial beams and plates with interconnected resonators," *International Journal of Solids and Structures*, vol. 139 - 140, 2018.

[11] T. Igusa and K. Xu, "Vibration control using multiple tuned mass dampers," *J. Sound Vib.*, vol. 175, pp. 491 –503, 1994.

[12] J. Ma, Z. Hou, and B. M. Assouar, "Opening a large full phononic band gap in thin elastic plate with resonant units," *Journal of Applied Physics*, vol. 115, 2014.

[13] M. Smith, "Synthesis of mechanical networks: The inerter," *IEEE Trans. Automat. Contr.*, vol. 47, pp. 1648 –1662, 2002.

[14] C. Yilmaz, G. Hulbert, and N. Kikuchi, "Phononic band gaps induced by inertial amplification in periodic media," *Phys. Rev. B*, vol. 76, pp. 054 309–1 –054309–9, 2007.

[15] N. Frandsen, O. Bilal, J. Jensen, and M. Hussein, "Inertial amplification of continuous structures: Large band gaps from small masses," *J. Appl. Phys.*, vol. 119, pp. 124 902–1 –011003–17, 2012.

[16] S. Taniker and C. Yilmaz, "Generating ultra wide vibration stop bands by a novel inertial amplification mechanism topology with flexure hinges," *International Journal of Solids and Structures*, vol. 106 - 107, pp. 129 –138, 2017.

[17] Y. Ding, Z. Liu, C. Qiu, and J. Shi, "Metamaterials with simultaneously negative bulk modulus and mass density," *Physical Review Letters*, vol. 99, no. 9, 2007.

[18] S. A. Pope, "Double negative elastic metamaterial design through electrical-mechanical circuit analogies," *IEEE Transactions on Ultrasonics, Ferroelectrics, and Frequency Control*, vol. 60, pp. 1467 –1474, 7 2013.

[19] P. S. Ma, H. J. Lee, and Y. Y. Kim, "Dispersion suppression of guided elastic waves by anisotoropic metamaterial," *J. Acoust. Soc. Am.*, vol. 13, EL77 –EL82, 2015.

[20] J. Wang and C. Mak, "Adaptive-passive vibration isolation between nonrigid machines and nonrigid foundations using a dual beam periodic structure with shape memory alloy transverse connection," *Journal of Sound and Vibration*, vol. 333, 2014.

[21] J. Vila, R. Pal, and M. Ruzzene, "Observation of topological valley modes in an elastic hexagonal lattice," *Phys. Rev. B*, vol. 96, 13 2017.

[22] M. Ruzzene, F. Scarpa, and F. Soranna, "Wave beaming effects in two-dimensional cellular structures," *Smart Mater. Struct.*, vol. 12, 2003.

[23] A. Phani, J. Woodhouse, and N. Fleck, "Wave propagation in two-dimensional periodic lattices," *J. Acout. Soc. Am.*, vol. 119, 2006.

[24] E. Baravelli and M. Ruzzene, "Internally resonating lattices for bandgap generation and low-frequency vibration control," *J. Sound Vib.*, vol. 332, pp. 6562 –6579, 2013.

[25] O. Yuksel and C. Yilmaz, "Shape optimization of phononic band gap structures incorporating inertial amplification mechanisms," *Journal of Sound and Vibration*, vol. 355, pp. 232 –245, 2015.

[26] L. Brillouin, *Wave Propagation in Periodic Structures, Electric Filters and Crystal Lattices*. Dover, 1946.

[27] Y. Lin and T. McDaniel, "Dynamics of beam-type periodic structures," *Journal of Engineering for Industry*, vol. 91, pp. 1133 –1141, 4 1969.

[28] M. Aberg and P. Gudmundson, "The usage of standard finite element codes for computation of dispersion relations in materials with periodic microstructure," *J. Acoust. Soc. Am.*, vol. 102, 1997.

[29] G. Gupta, "Natural flexural waves and the normal modes of periodically-supported beams and plates," *Journal of Sound and Vibration*, vol. 13, pp. 89 –101, 1 1970.

[30] C. Sugino, S. Leadenham, M. Ruzzene, and A. Erturk, "On the mechanism of bandgap formation in locally resonant finite elastic metamaterials," *Journal of Applied Physics*, vol. 120, 2016.

[31] M. Hussein, M. Leamy, and M. Ruzzene, "Dynamics of phononic materials and structures: Historical origins, recent progress, and future outlook," *Applied Mechanics Reviews*, vol. 66, 2014.

[32] J. Huang, Z. Shi, W. Huang, X. Chen, and Z. Zhang, "A periodic foundation with rotational oscillators for extremely low-frequency seismic isolation: Analysis and experimental verification," *Smart Materials and Structures*, vol. 26, 2017.

[33] A. Spadoni and C. Daraio, "Vibration isolation via linear and nonlinear periodic devices," *Proceedings of the ASME 2009 International Design Engineering Technical Conferences and Computers and Information in Engineering Conference (IDETC/CIE)*, pp. 277 –284, 2009.

[34] C. Crede, *Vibration and Shock Isolation*. New York: Wiley, 1951.

[35] V. Ivovich and M. Savovich, "Isolation of floor machines by lever-type vibration corrector," *Proceedings of the Institution of Civil Engineers - Structures and Buildings*, vol. 146, pp. 391 –402, 2001.

[36] M. Munjal, "A rational synthesis of vibration isolators," *J. Sound Vib.*, vol. 39, pp. 247 –263, 1975.

[37] K. Reichl and D. Inman, "Lumped mass model of a 1D metastructure for vibration suppression with no additional mass," *J. Sound Vib.*, vol. 403, pp. 75 –89, 2017.

[38] C. Yilmaz and N. Kikuchi, "Analysis and design of passive low-pass filter type vibration isolators considering stiffness and mass limitations," *J. Sound Vib.*, vol. 293, pp. 171 –195, 2006.

[39] L. Liu and M. Hussein, "Wave motion in periodic flexural beams and characterization of the transition between bragg scattering and local resonance," *J. Appl. Mech.*, vol. 79, pp. 011 003–1 –124902 –14, 2016.

[40] S. Ochi, K. Kagawa, G. A. Calhoon, and K. Beamer, "Vacuum circuit breaker technology: Vacuum interrupters - how they work," *NETA WORLD*, pp. 1 –7, 2010.

[41] H. Yang, L. Yu, W. Hou, S. R. Matu, and Y. Zhang, "Initial impact measurement during opening of vacuum circuit breakers," in *2015 3rd International Conference on Electric Power Equipment*, 2015, pp. 95–97.

[42] P. G. Slade, "Advances in material development for high power, vacuum interrupter contacts," *IEEE Transactions on Components, Packaging, and Manufacturing Technology: Part A*, vol. 17, no. 1, pp. 96–106, 1994.

[43] ——, "The vacuum interrupter contact," *IEEE Transactions on Components, Hybrids, and Manufacturing Technology*, vol. 7, no. 1, pp. 25–32, 1984.

[44] ——, "Contact materials for vacuum interrupters," *IEEE Transactions on Parts, hybrids, and packaging*, vol. 10, no. 1, pp. 43–47, 1974.

[45] K. Graff, *Wave Motion in Elastic Solids*. Dover Publications, 1975.

[46] P. Barkan, "A study of the contact bounce phenomenon," *IEEE Transactions on Power Apparatus and Systems*, 1967.

[47] J. Wang, Z. Liu, S. Xiu, Z. Wang, S. Yuan, L. Jin, H. Zhou, and R. Yang, "Development of high-voltage vacuum circuit breakers in china," *IEEE Transactions on Plasma Science*, vol. 35, pp. 856–865, 2007.

[48] L. Yu, Z. Liu, J. Wang, Y. Geng, L. Sun, R. Yu, and X. Xue, "Contacts impact phenomena in a 126 kv vacuum circuit breaker," in *25th International Symposium on Discharges and Electrical Insulation in Vacuum (ISDEIV)*, 2012, pp. 473–476.

[49] L. Yu, Y. Geng, Q. Li, J. Wang, and Z. Liu, "An approach for minimum percussion welding in closing operation of a 126-kv vacuum circuit breaker," *IEEE Transactions on Components, Packaging and Manufacturing Technology*, vol. 4, pp. 840–847, 2014.

[50] S. P. Chapra and R. P. Canale, *Numerical Methods for Engineers, 7th ed*. McGraw-Hill Education, 2015.

[51] G. S. Jiang and C. W. Shu, "Efficient implementation of weighted eno schemes," *Journal of Computational Physics*, vol. 126, 1 1996.

[52] J. Doyle, *Wave Propagation in Structures*. Springer, 1998.

[53] H. Kolsky, "An investigation of the mechanical properties of materials at very high rates of loading," *Proc. Phys. Soc. B.*, vol. 62, 1949.

[54] T. Togami, W. Baker, and M. Forrestal, "A split hopkinson bar technique to evaluate the performance of accelerometers," *Journal of Applied Mechanics*, vol. 63, 1996.

[55] J. Meng and A. Dasgupta, "Influence of secondary impact on printed wiring assemblies - part i: High frequency 'breathing mode' deformations in the printed wiring board," *J. Electron. Packag.*, vol. 138, 1 2016.

[56] ——, "Influence of secondary impact on printed wiring assemblies - part ii: Competing failure modes in surface mount components," *J. Electron. Packag.*, vol. 138, 1 2016.

[57] D. J. Frew, M. J. Forrestal, and W. Chen, "Pulse shaping techniques for testing brittle materials with a split Hopkinson pressure bar," *Experimental Mechanics*, vol. 42, 1 2002.

[58] K. Xia, M. H. B. Nasseri, B. Mohanty, F. Lu, R. Chen, and S. N. Luo, "Effects of microstructures on dynamic compression of barre granite," *International Journal of Rock Mechanics and Mining Sciences*, vol. 45, 2008.

[59] K. Yuan, W. Guo, Y. Su, J. Lei, and H. Guo, "Study on several key problems in shock calibration of high-g accelerometers using Hopkinson bar," *Sensors and Actuators A: Physical*, vol. 258, 2017.

[60] K. Tan, H. Huang, and C. Sun, "Blast-wave impact mitigation using negative effective mass density concept of elastic metamaterials," *International Journal of Impact Engineering*, vol. 64, 2014.

[61] E. Kim, J. Yang, H. Hwang, and C. Shul, "Impact and blast mitigation using locally resonant woodpile metamaterials," *International Journal of Impact Engineering*, vol. 101, pp. 24 –31, 2017.

[62] M. M. Sigalas and E. N. Economou, "Elastic and acoustic wave band structure," *Journal of Sound and Vibration*, vol. 158, pp. 377 –382, 2 1992.

[63] H. Matsuda, T. Sakiyama, C. Morita, and M. Kawakami, "Longitudinal impulsive response analysis of variable cross-section bars," *Journal of Sound and Vibration*, vol. 181, pp. 541 –551, 3 1995.

[64] M. Hetenyi, *Beams on Elastic Foundation: Theory With Applications in the Fields of Civil and Mechanical Engineering*. Springer, 1998.

[65] R. Uhrig, "The transfer matrix method seen as one method of structural analysis among others," *Journal of Sound and Vibration*, vol. 4, pp. 136 –148, 2 1966.

[66] F. Jiang and K. Vecchio, "Hopkinson bar loaded fracture experimental technique: A critical review of dynamic fracture toughness tests," *Applied Mechanics Reviews*, vol. 62, 2009.

[67] K. Xia and W. Yao, "Dynamic rock tests using split Hopkinson (Kolsky) bar system - a review," *Journal of Rock Mechanics and Geotechnical Engineering*, vol. 7, 1 2015.

[68] J. Harding, E. Wood, and J. Campbell, "Tensile testing of materials at impact rates of strain," *Journal of Applied Mechanics*, vol. 38, no. 1, pp. 83–91, Mar. 1971.

[69] J. Lewis and J. Campbell, "The development and use of a torsional Hopkinson-bar apparatus," *Experimental Mechanics*, vol. 12, pp. 520 –524, 1972.

[70] J. Duffy, J. D. Campbell, and R. H. Hawley, "On the use of a torsional split Hopkinson bar to study rate effects in 1100-0 aluminum," *Journal of Applied Mechanics*, vol. 38, no. 1, pp. 83–91, Mar. 1971.

[71] A. Leissa and M. Qatu, *Vibrations of Continuous Systems*. McGraw-Hill Professional, 2011.

[72] M. Eisenberger, "Exact longitudinal vibration frequencies of a variable cross-section rod," *Applied Acoustics*, vol. 34, pp. 123 –130, 2 1991.

[73] B. Kumar and R. Sujith, "Exact solutions for the longitudinal vibration of non-uniform rods," *Journal of Sound and Vibration*, vol. 207, pp. 721 –729, 5 1997.

VITA

William Johnson was born in Provo, Utah, while his parents were undergraduate students at Brigham Young University (BYU), and spent his entire childhood there. While living there, many of his neighbors and close family friends were accomplished professors, which helped encourage him to pursue a PhD. In high school his favorite subject was mathematics. Prior to starting his bachelors degree, he took a two year sabbatical to serve as a volunteer missionary for his church, The Church of Jesus Christ of Latter-Day Saints. He had the opportunity to serve in Hawaii and on Christmas Island, where he became fluent in the Micronesian language of Kiribati (Gilbertese). While in Hawaii he developed a strong desire to understand how the world came to be the way it was. This interest has extended to philosophy, psychology, politics, and history. His study of mechanical engineering is an extension of this. He did his bachelors and masters degrees at BYU in mechanical engineering, also obtaining minors in mathematics and philosophy. His enjoyment of his masters program led him to pursue a PhD, which this dissertation is the culmination of. While working on his PhD he met his wife at a New Year's Eve party. They now have one son and hope to have several more children.